MASS TRANSFER IN BINARY STARS USING SPH

MASS TRANSFER IN BINARY STARS USING SMOOTHED PARTICLE HYDRODYNAMICS

By

CHARLES-PHILIPPE LAJOIE, B.Sc., M.Sc.

A Thesis

Submitted to the School of Graduate Studies

in Partial Fulfillment of the Requirements

for the Degree of

Doctor of Philosophy

McMaster University

DOCTOR OF PHILOSOPHY (2010) McMaster University
(Physics and Astronomy) Hamilton, Ontario

TITLE: Mass Transfer in Binary Stars using Smoothed Particle Hydrodynamics

AUTHOR: Charles-Philippe Lajoie, B.Sc., M.Sc. (Université de Montréal)

SUPERVISOR: Professor Alison Sills

NUMBER OF PAGES: xvi, 184

Abstract

Despite numerous efforts to better understand binary star evolution, some aspects of it remain poorly constrained. In particular, the evolution of eccentric binaries has remained elusive mainly because the Roche lobe formalism derived for circular binaries does not apply, and other approximations must be used. Here, we report the results of our Smoothed Particle Hydrodynamics simulations of eccentric binaries using a novel way of modeling only the outermost layers of the stars with appropriate boundary conditions. We find that our boundary treatment conserves energy well and that it is well suited for the modeling of interacting binary stars. Using this new technique, along with properly relaxed model stars, we find clear trends in the mass transfer episodes. In particular, we show that these episodes can be described by Gaussians with a FWMH of $\sim 0.12\ P_{orb}$ and that the peak rates occur after periastron, around an orbital phase of ~ 0.55, independent of the eccentricity and masses of the stars. The accreted material, on the other hand, is observed to form a rather sparse envelope around either or both stars. Although the fate of this envelope is not modeled in our simulations, we show that a constant fraction ($\sim 5\%$) of the material transferred is ejected from the systems. We discuss this result in terms of the poorly constrained non-conservative mass transfer scenario and argue that it can help calibrate it. Finally, we discuss the limitations of our technique and conditions under which it performs best. The results presented in this thesis represent an improvement upon previous hydrodynamical work and could be used in analytical and binary population synthesis studies to better constrain the evolution of eccentric binaries and the formation of exotic stellar populations.

À la mémoire de mon père, Pierre

Acknowledgements

The work presented in this thesis is the fruit of over four years of research, programming, and collaborations. Such an endeavour is rarely accomplished alone, and here I make no exception. I wish to acknowledge many people who made this project possible in one way or another.

Before all else, I especially wish to thank my advisor, Alison Sills, whose ideas, suggestions, and relentless encouragements contributed to make this thesis what it is. I also wish to thank the members of my thesis committee, Doug Welch and James Wadsley, whose advices only made my work and thesis better. My journey at McMaster would not have been the same without the precious help and care of all the staff of the Physics & Astronomy department. No doubt that they are the ones that make our passage here so smooth and enjoyable. I also want to thank Hua Wu, for his patience and passion for computers, without whom countless hours of work could have been lost. The simulations presented in this thesis were made possible by the facilities of SHARCNET and I thank the people there for their support and dedicated resources programs. Many thanks also go to my fellow aspiring physicists from the department, with whom I have shared offices, played hockey, soccer, squash, etc, and spent late nights at the Phoenix. I must also thank my coaches and teammates from the McMaster Lacrosse team who introduced me to this great sport and helped me become the player (and captain) that I now am. Playing on the field allowed me to clear my mind from all the long days spent in my office. I had an awesome time playing lacrosse and I will remember it forever. Last, but not least, I particularly want to thank my parents, siblings, and girlfriend for their encouragements, patience, and most importantly, love. The last two years have been difficult; I have missed you and I have wished I could be with you all more often. All your visits have been much appreciated and your support unmatched, and I can never thank you enough for everything you have done for me. As hard as I have worked to complete this thesis, it would never have been possible without you.

Table of Contents

List of Figures

List of Tables

"To explain all nature is too difficult a task for any one man or even for any one age. 'Tis much better to do a little with certainty & leave the rest for others that come after, than to explain all things by conjecture without making sure of any thing."

SIR ISAAC NEWTON (1643-1727)

Chapter 1

Introduction

Gravitation rules. It is what forms dark matter halos and giant molecular clouds. It is also what compresses these clouds of gas to such an extent that stars form out of them. And these newly-formed stars are often bound to each other by means of this force, allowing for the formation of star clusters, galaxies, and clusters of galaxies. From the falling meteorites and the revolution of planets around stars to the dynamics of clusters of galaxies, the inevitability of the gravitational force creates some of the most spectacular phenomena in the Universe. In particular, when two stars orbit around each other, forming what we call a binary stellar system, the relentless inward pull of the gravitational force can sometimes bring stars so close to each other that material starts flowing from one star to the other. It is easily imaginable that such episodes of mass transfer can alter significantly the course of evolution of a star. The first realization of the importance of binary interactions may have been by Crawford (1955), who suggested an interesting solution to the so-called "Algol paradox". Algol is a binary star composed of a Sun-like star and a slightly more evolved star. Paradoxically, the more evolved star is also the least mas-

sive of the two stars, at odds with the standard stellar evolution theory, and Crawford (1955) realized that the close proximity of the two components must have led to significant mass transfer from the initially more massive star to the least massive one until the roles were reversed. This discovery opened the door for an even wider range of classes of stars and much work has since been done in order to draw a full picture of the galactic stellar populations. Nowadays, such close, interacting binary stars are believed to be the most efficient way of forming exotic stellar populations such as cataclysmic variables (CVs) and X-ray binaries, helium white dwarfs, and blue stragglers. CVs and X-ray binaries are composed of compact objects, such as black holes, neutron stars, and white dwarfs, all swallowing infalling matter from a larger and tenuous companion. The very existence of these compact objects in such tight binaries is hard to explain using only the standard single-star evolution theory and it is now acknowledged that close binary interactions must have taken place during the formation of such systems (e.g. Paczyński 1976). Similarly, white dwarfs are the most common stellar remnants in the Galaxy and are composed of what was once the core of a Sun-like star. The more massive (and oldest) of these progenitors form white dwarfs composed mainly of carbon and oxygen, but less massive, longer-lived progenitors are expected to form only a helium core. However, for a single star to fade away as a helium white dwarf requires a period of time longer than the age of the Galaxy, so we should simply not be able to observe such stars. It is now believed that helium white dwarfs must have been formed in binary systems in which material from the progenitors was stripped by a close companion until the helium core was exposed. The origin of blue stragglers, on the other hand, has remained elusive. When compared to other stars, the brightness of blue stragglers suggest that they have

been rejuvenated at some point, extending their lifetime by some millions of years. Although this question still remains unanswered, a binary origin for blue stragglers has been suggested, adding to the stellar exotic populations of the galaxy. Even for stars that are not transferring mass, a close companion can have all sorts of observable effects. RS Canum Venaticorum stars, for example, are variable binaries with enhanced chromospheric and magnetic activity that is thought to originate from the tidal effects from a close companion (e.g. Rodono 1992). These are all examples of how binary interactions can modify the evolution of stars and, as of today, there does not seem to be any other way to account for these systems other than by binary interactions.

The study of such exotic stellar populations requires the understanding of close binary evolution. In turn, the study of binary evolution involves different physical mechanisms occurring over different timescales, which quickly render the problem at hand complicated. For example, the numerous nuclear reactions that allow stars to shine occur (and change) over millions, even billions, of years, whereas the change of the orbital separation due to gravitational radiation, magnetic braking and stellar winds (all referred to as angular momentum loss mechanisms) occurs on much shorter, dynamical timescales. Also, the structure of stars is affected by the loss of mass and angular momentum and the ensuing response differs depending on the mass of the star. This response, in turn, can give rise to mass loss on timescales ranging from a few days to a few million years. The theoretical tools generally used to study binary systems can not resolve all of these timescales; they usually incorporate only some of these mechanisms and rely on approximations to realistically model such binary systems. Stellar evolution codes can successfully evolve single stars over many billion years while taking into account the different nuclear

reactions networks. Only recently have they been used to evolve binary stars, although most of them are still in one dimension and only a handful use two dimensions (Han, Tout, & Eggleton, 2000; Deupree & Karakas, 2005). Moreover, they rely on prescriptions for the mass transfer and accretion rates. These same prescriptions and approximations have also been used to model different populations of binary stars with population synthesis codes, which can evolve many millions of stars at once over the age of the Galaxy, i.e $10^9 - 10^{10}$ years (Portegies Zwart & Verbunt, 1996; Hurley et al., 2002; Ivanova et al., 2005). None of these techniques can actually model the mass transfer itself as it often occurs on dynamical timescales of the order of a day or less. Hydrodynamics, on the other hand, is well suited for such purposes, although it can be hard to incorporate physical ingredients such as convection, magnetic fields, and nuclear reactions. Moreover, hydrodynamics is usually not designed to evolve stars over long periods of time, making the long-term hydrodynamical evolution of binary stars rather challenging to achieve.

In general, people have focused on idealized cases where the orbit is circular, the rotation of the stars is synchronized with the orbital velocity (such that the stars always show the same hemispheres to each other, in a similar fashion as we always see the same side of the moon), and mass transfer is conservative (i.e. the mass lost by one star remains bound to the system and/or is all accreted by the other star). Seminal work by Morton (1960), Paczyński (1965, 1971) and Paczyński & Sienkiewicz (1972), among others, on mass transfer and its consequences on the stars and the orbital parameters have opened the way to a more quantitative study of binary evolution. Iben (1991) and Iben & Livio (1993) have more recently laid out the overall evolutionary paths of many different binary populations and qualitatively ex-

plained the formation scenarios of many exotic objects but, from a theoretical point of view, a detailed description of some aspects of close interactions under different circumstances is still lacking. Of particular interest are (1) the rate at which mass is transferred from one star to the other, (2) the amount of mass accreted by the secondary stars, and (3) the degree of mass expelled from these systems, if any. To date, these quantities have usually been either approximated from theoretical estimates or arbitrarily assumed fixed. But because these quantities bear important relevance for the long-term evolution of binary stars, as they are some of the mechanisms that drive the change of orbital separation, which ultimately decides on the fate of the system, it is important to get better estimates for the more realistic, non-idealized cases. In particular, recent studies (Sepinsky et al. 2007a, 2007b, 2009) have suggested that eccentric binaries may evolve differently compared to the circular binaries. Given that a non-negligible fraction ($\sim 20\%$) of interacting binaries have eccentric orbits (Petrova & Orlov, 1999; Raguzova & Popov, 2005), this could arguably modify the formation rates and total numbers of particular binary populations in synthesis models. Therefore, a better understanding and calibration of the mass transfer rates, the degree of mass loss from binary systems, and the accretion process are needed in order to get a better, more realistic picture of the exotic stellar populations.

In this thesis, we present a new hydrodynamical approach to model episodic mass transfer in binaries, especially those with eccentric orbits for which many theoretical questions remain unanswered. First, in Chapter 2, we discuss important aspects of binary evolution and emphasize on the need for detailed hydrodynamical simulations of mass transfer for better understanding the variety of stellar objects observed. Our computational method, along with

a new, innovative approach are introduced and tested in Chapter 3. Chapter 4 is dedicated to the applicability of our new technique to binary stars. We discuss our initial conditions and show how our code performs in dealing with binary stars. We then present in Chapter 5 our first high-resolution simulations of mass transfer in eccentric binaries and show that our new approach is well suited for such purposes. We model two different binary systems with various eccentricities and separations and concentrate on how and when mass transfer is initiated, as well as how much mass is accreted by the companion star and/or lost from the system. The work presented in this thesis, apart from introducing an innovative treatment of boundary condition for the hydrodynamic modeling of stars, is aimed at better estimating mass transfer rates, mass accretion, and mass loss in binary systems and help better calibrate population synthesis codes. In particular, this work is relevant for the study of the origin of blue straggler stars, which may be linked to past binary interactions but still remains elusive to this day.

Chapter 2

On the Evolution of Binary Stars

From a theoretical point of view, the evolution of an isolated star has been fairly well understood for many decades now (see, e.g., Clayton 1984 and Iben 1991). Stars are mostly made up of hydrogen ($\sim$ 70%) and helium ($\sim$ 30%) and they spend most of their nuclear life converting hydrogen into helium on the so-called main sequence. These nuclear reactions release a tremendous amount of energy every second (according to the equation $E = mc^2$) which is emitted as X-rays, ultraviolet, visible, and infrared light. Stars come in a variety of masses, as shown in Figure 2.1a, with masses typically ranging from $\sim$ 0.08 $M_\odot$ for the M-type stars to $\sim$ 100 $M_\odot$ for the O stars (main-sequence stars are commonly classified using the letters O, A, B, F, G, K, and M, referred to as their spectral type, and is an indication of their surface temperature and mass). The luminosity, and hence the rate at which the nuclear reactions take place, depends mainly on the mass of the star, and the more massive the star is, the faster it burns its nuclear reservoir. For example, 20-$M_\odot$ stars live on the main sequence for "only" a few million years, whereas stars like our Sun or less massive will live for 10 to 100 billion years (for comparison, the estimated age of

the Universe is $\sim$ 13.7 billion years; see, e.g., Hansen & Kawaler 1994). When stars exhaust their hydrogen reservoir, they undergo drastic structural changes. Depending on the mass of the stars, the consecutive burning and exhaustion of hydrogen, helium, and heavier elements such as carbon, oxygen, silicon, and others all the way up to iron, forces the stars to expand, sometimes by many orders of magnitude. After exhausting hydrogen and helium, stars climb up the so-called red giant branch (RGB) or the asymptotic giant branch (AGB). During these late phases of stellar evolution, copious amounts of material are ejected into the interstellar medium through stellar winds, slowly peeling off the different layers of the stars and revealing the inner stellar core. At one point, when a star is unable to reach high enough temperatures to further process heavier elements, nuclear reactions shut off and the star is doomed to fade away. This is the death of the star, and most stars in the Galaxy will disappear in such a way and leave behind a white dwarf star, an earth-sized object with more or less half the mass of the Sun. These objects are usually composed of carbon and oxygen, although some (exotic) helium white dwarfs are thought to exist. On the other hand, for the most massive stars, this is not quite the end. For stars with initial masses greater than $\sim$ 10 $M_{\odot}$, nuclear reactions allow for the processing of heavier elements, sometimes up to the iron-group elements. When this happens, the iron core builds up in mass and, at some point, cannot support itself against the pull of its own gravity and collapses onto itself, creating a supernova explosion. The remnant of such an explosion is either a neutron star or, for stars initially more massive than $\sim$ 25 $M_{\odot}$, a stellar black hole.

Although the actual theory of stellar evolution has succeeded in describing the life of single stars, it breaks down when stars get too close to

each other because of tidal effects and possible episodes of mass transfer. As discussed in Chapter 1, we now understand that binary star evolution is an efficient (and important) way of forming all kinds of exotic stellar populations. As we discuss next, binary stars are common and a fairly large fraction of these are doomed to interact with their companion at some point in their life. The actual basic understanding of how binary stars form, interact, and evolve is also discussed and we emphasize on how crucial binaries are to the general understanding of galactic stellar populations.

2.1 Observations of binary stars

Binary stars, just like single stars, form in the cores of dense collapsing molecular clouds. However, whether they form from the prompt (or delayed) fragmentation of the latter collapsing cloud or from gravitational captures early on after the single stars have formed still remains unclear (see Tohline 2002 for a review of the status of binary star formation). Despite some gaps in the theoretical understanding regarding the formation of binaries, we know that stellar multiplicity is more the rule than the exception. Indeed, observations suggest that a large fraction of stars are part of multiple systems and it is not rare to find them in double, triple, quadruple, and even sextuple systems (e.g. α Gem). Surveys carried by Abt & Levy (1976), Duquennoy & Mayor (1991), Halbwachs et al. (2003), and Fischer & Marcy (1992) monitored stars with masses between ~ 0.1 and ~ 1.5 $M_{\odot}$ (i.e. spectral types $F-G$, K and M) for common proper motion and radial velocity variations and found that at least 50% of the stars in their sample were part of multiple systems (correcting for incompleteness, as longer periods may have been missed, may bring this

number to higher values). Interestingly, a survey of pre-main-sequence stars by Mathieu (1994) showed that new-born stars may even have a higher multiplicity and that their orbital parameter distributions are very similar to those of main-sequence stars, which may help better constrain the origin and formation mechanisms of the present day galactic binary populations. Although a complete description of the binary population (i.e. masses of stars, separation, eccentricities, etc) is difficult to obtain due to selection effects and observational limitations, it is observed that massive stars are more likely to be found in binary systems than their low-mass counterparts and that the distribution of secondary masses is representative of a random pairing from a typical field initial mass function (Duquennoy & Mayor 1991; see also Figure 2.1a). This can not be true however for massive O- and B-type stars as well as close binaries, i.e. those with $P \lesssim 10 - 15$ days, since they are preferentially found with comparably massive companions (Eggleton, 2006). The distribution of mass ratios ($q_1 \equiv M_1/M_2$) is hard to obtain as it requires spectroscopic data for both stars, but observations suggests that it is somewhat flat between $0.2 < q < 0.7$ and peaked around $q \approx 0.8 - 1.0$ (Halbwachs et al. 2003, Figure 7). This, however, depends on the mass of the primary star as well as on the separation. Figure 2.1b shows the period distribution from the Heintz (1969) and Duquennoy & Mayor (1991) samples. The distributions of the logarithm of the periods are roughly Gaussian and typically range from a fraction of a day to a few 10^5 days with a mean around ~ 200 years. Again, care must be taken here as this distribution may not be representative of binaries of all masses. Indeed, there seems to be a dependence of the mean period and the width of the period distribution on the primary mass as O-stars show a bias towards shorter periods (Eggleton, 2006), although this may be partly due to selection

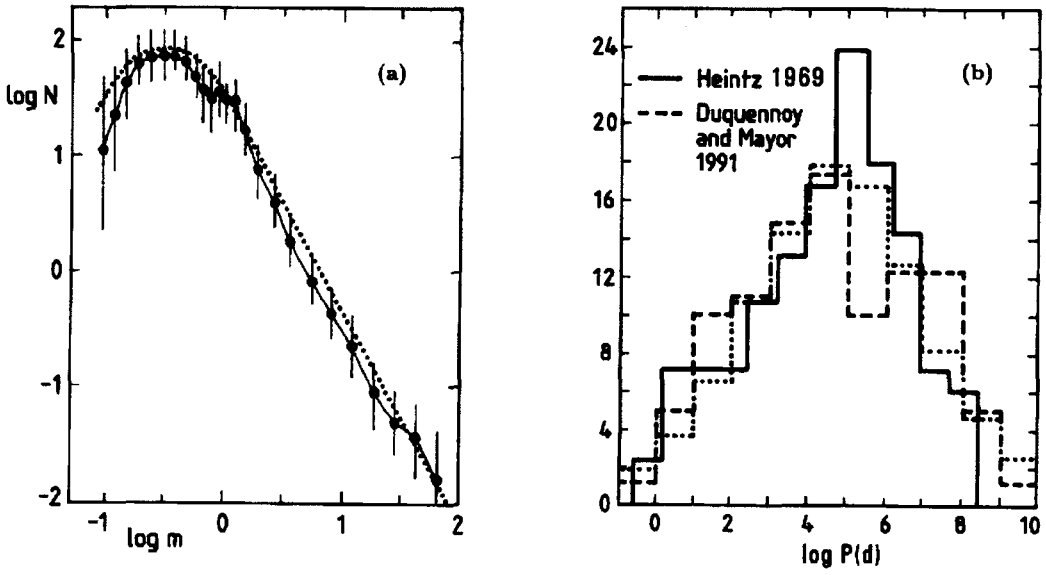

Figure 2.1 (a) Distribution of initial masses from Scalo (1986). (b) Normalized binary period distribution from the Duquennoy & Mayor (1991) and Heintz (1969) samples. The dotted lines are analytical approximations which, along with the figures, can be found in Eggleton (2006).

effects. Figure 2.2 shows the period-eccentricity relation for solar-type binaries in the open cluster M35 from Meibom & Mathieu (2005). In the case of the period-eccentricity relation, the results are much more consistent for all types of stars (early- and late-types, as well as evolved and planetary components) between each other and generally show that binaries with periods longer than 1 to 10 days have a wide range of eccentricities whereas most short-period binaries appear to be on circular orbits. Meibom & Mathieu (2005) argue that the period where this cut-off occurs is consistent with the circularization timescale and supports the idea of tidal evolution for these close systems. Tidal circularization and synchronization are the consequences of dissipative effects such as retarded tidal bulging and excitation and damping of gravity

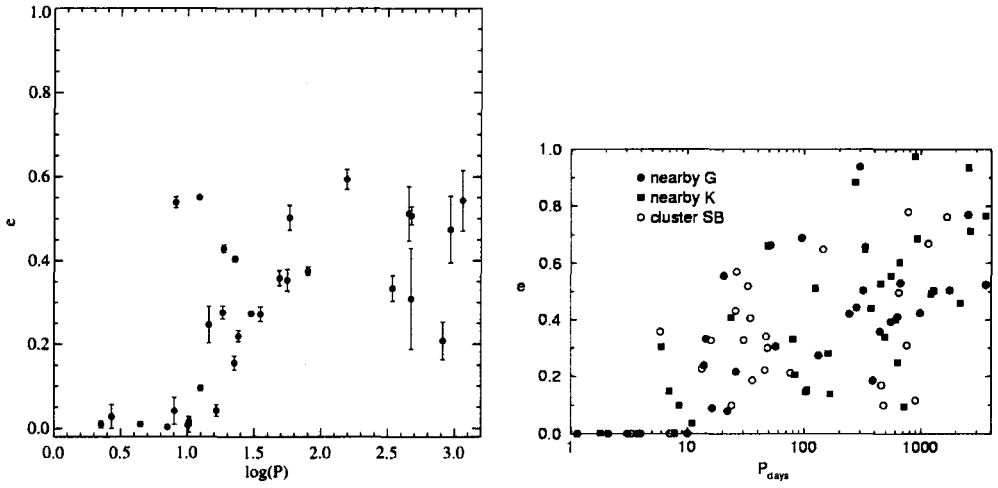

Figure 2.2 Period-eccentricity diagram for solar-type binaries in M35 (left; Meibom & Mathieu 2005) and the solar neighbourhood + Pleiades + Praesepe (right; Halbwachs et al. 2003). The period is in days and the period cut-off is around 10 days in both cases.

waves in a star's envelope due to a close companion. These oscillations in a star's envelope are slowly dissipated and orbital energy is removed until a state of minimum energy is reached, at which point the orbit is circular and the stars' rotation is synchronized with the orbital angular velocity (Zahn 1977; Hut 1981; Savonije & Papaloizou 1983; Meibom & Mathieu 2005). The circularization and synchronization timescales are usually assumed to be short (i.e. $\sim 10^6 - 10^8$ years), although they are still uncertain. As we shall see later, it is because of this period cut-off that authors have usually assumed that close and interacting binaries are circular (or become circularized very rapidly after the onset of mass transfer).

Because stars grow in size considerably as they evolve, there is a limit on how close they can be to a companion star. Indeed, for large enough separations, some stars will most likely never "feel" the presence of their companion and evolve just as if they were in isolation. Paczyński (1971) estimated that a

binary composed of a 5-$M_\odot$ star and a 2.5-$M_\odot$ companion is very unlikely to interact if the initial period is greater than $\sim 10^4$ days; for such large periods, the stellar radius of the primary will likely never reach the Roche lobe limit (see §2.2.1) and tidal and binary interactions, if any, will probably be inconsequential. Thus, even by using 10^4 days as a crude estimate for the period limit, the observed period distributions of Figure 2.1b suggests that a fairly large fraction of the observed binaries might interact at some point of their life.

The canonical value of $\sim 10^4$ days for the period cut-off of interacting binaries is not strictly constraining as it does not take into account effects such as supernova explosions, stellar winds and stellar encounters, which can all affect binary systems. Indeed, some stars lose material through a stellar wind which can be accreted by the secondary even in cases where the stars are well within their Roche lobe (§ 2.2.1) and may affect the subsequent evolution of the system. The case of the barium stars is a good example. These stars show enhanced s-process element abundances, which may be the result of accretion of such a wind from a white dwarf progenitor while on the red or asymptotic giant branches, where s-process elements are thought to be processed. Moreover, mechanisms such as magnetic braking and gravitational radiation may help getting rid of some orbital angular momentum and bring stars closer to each other, hence favoring close interactions. Similarly, Kozai cycles (Kozai, 1962) in hierarchical systems (i.e. multiple systems where an inner binary is orbited by one or more stars) can make the eccentricity of the inner binary vary greatly while keeping the period and semi-major axis constant. These cyclic changes in eccentricity can lead to tidal interactions, most likely at periastron passages, and close interactions such as mass transfer

(e.g. Eggleton & Kisseleva-Eggleton 2006). Binaries and hierarchical systems can also be formed dynamically through captures or exchanges and destroyed through mergers and collisions in dense environments such globular clusters (e.g. Pooley & Hut 2006). As a matter of fact, the high numbers of X-ray sources observed in globular clusters are now believed to be due to the high encounter and stellar capture rates typical of these dense environments (Binney & Tremaine, 1987). These dynamically-formed binaries are likely to be found, initially, in close eccentric orbits. The idea that binaries on eccentric orbits can be interacting with a close companion is supported by the compilation of 128 eccentric binaries by Petrova & Orlov (1999) (see also Raguzova & Popov 2005) identified 27 semi-detached or contact systems, among which some have an eccentricity greater than 0.1. Whether these eccentric binaries are primordial or were formed by capture is unknown, but they have remained on an eccentric orbit long enough for us to observe them despite the mechanisms at play in close binaries that lead to circularization and synchronization

.

2.2 Theoretical description of binary stars

Although there is plenty of evidence for close binary evolution, the actual evolution of such systems can probably only be better understood theoretically as these interactions occur and can last over nuclear timescales (i.e. $\sim 10^9$ years). Binaries are held together by gravitation, and Newton's law of gravitation shows that binary stars (or any two objects such as planets around stars) orbit their mutual centre of mass and that these orbits have the shape of (similar) ellipses, as depicted in Figure 2.3. In the reference frame of the centre

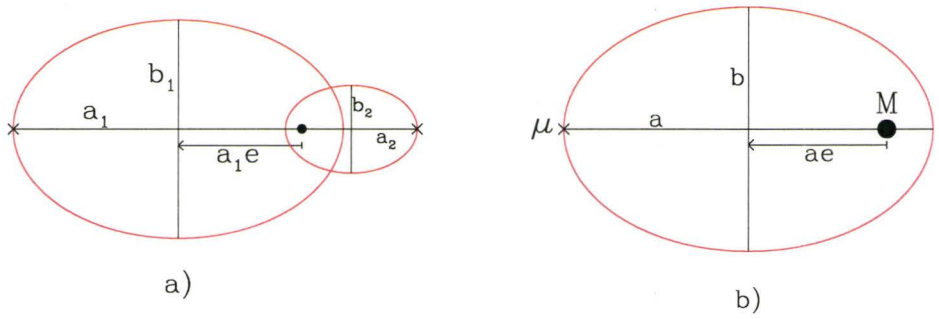

Figure 2.3 *a*) Ellipses of eccentricity $e = 0.5$ showing the path of both stars along their orbit around their centre of mass (solid dot). Their respective semi-major and semi-minor axes are labeled. *b*) Same eccentric system but viewed from the centre-of-mass reference frame, where it can be interpreted as a mass $\mu = M_1 M_2/(M_1 + M_2)$ orbiting a mass M=$M_1 + M_2$.

of mass, where a mass $\mu \equiv M_1 M_2/(M_1 + M_2)$ orbits a mass M= $M_1 + M_2$, the semi-major (a) and semi-minor (b) axes of the elliptic orbit of μ define the eccentricity $e = \sqrt{1 - b^2/a^2}$. The orbital period of a binary system can then be written as the generalized Kepler's third law:

$$P^2 = \frac{4\pi^2 a^3}{G(M_1 + M_2)}. \tag{2.1}$$

where P is the period, $a = a_1 + a_2$ is the orbital separation, G is the gravitational constant, and M_1 and M_2 the masses of both stars. This equation shows that the orbital period is inversely proportional to the total mass, and proportional to the third power of the separation. The period of a binary is probably the easiest piece of information to obtain as it can be deduced from radial velocity variations and photometric curves of transiting binaries. Moreover, the shape of the radial velocity variation curve can yield the eccentricity of the orbit as well as the node angle, whereas the amplitude of the velocity

variation, K, can yield precious information about the the mass ratio and the inclination of the orbit. Furthermore, information on the individual masses of the stars can be derived from the so-called binary mass function f,

$$f = \frac{(M_2 \sin i)^3}{(M_1 + M_2)^2} = \frac{K_1^3 P (1 - e^2)^{3/2}}{2\pi G}, \tag{2.2}$$

where i is the inclination of the orbit with respect to the plane of the sky. The binary mass function only yields the minimum mass of the (unseen) companion, unless the inclination of the orbit can be determined. To uniquely determine these orbital parameters for a particular system, one needs a double-lined spectroscopic or visual binary. In general, binary orbital parameters, as well as the overall trends discussed in §2.1, are determined using Equation 2.2.

2.2.1 The Roche approximation

For close interacting binaries the picture is slightly more complicated, as mass can be transferred. To better understand how this can happen, it is useful to use a reference frame rotating with the stars. This was first done by the French physicist Joseph-Louis Lagrange (1736-1813) in 1772, who, at the time, was studying the three-body problem. Under the assumptions of point masses (or, to a larger extent, centrally condensed stars) and circular and synchronous orbits, one can write the effective gravitational potential at any point in space as

$$\Phi = \frac{-GM_1}{\sqrt{(x - x_1)^2 + y^2 + z^2}} + \frac{-GM_2}{\sqrt{(x - x_2)^2 + y^2 + z^2}} - \frac{1}{2}\Omega^2 r^2 \tag{2.3}$$

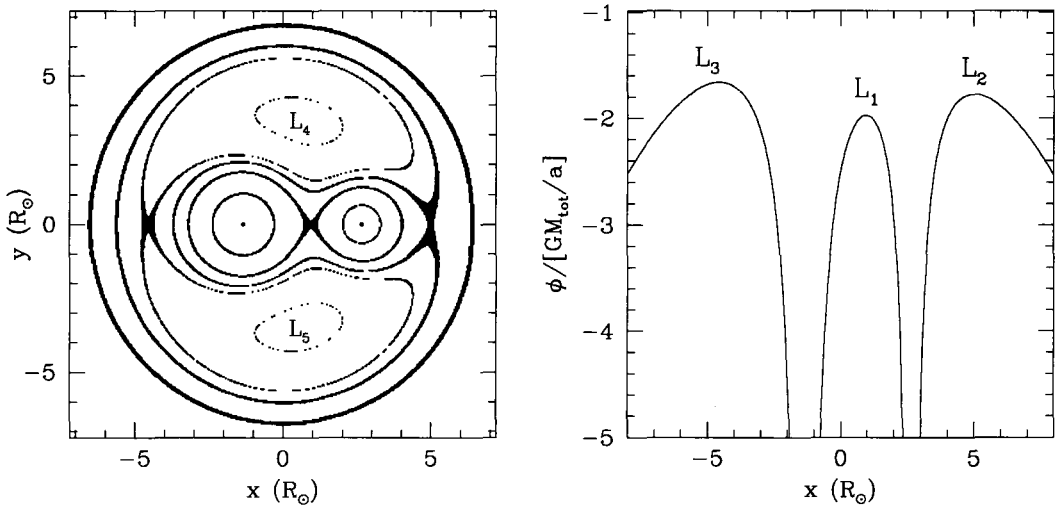

Figure 2.4 *Left*: Equipotentials for a binary system with $q_1 = 2$ and an orbital separation of 4 solar radii. The Lagrangian point L_3, L_1, and L_2 are located on the $y = 0$ axis (from left to right) whereas the L_4 and L_5 are labeled. *Right*: Potential as a function of x along the $y = 0$ axis, passing through the first three Lagrangian points and showing the stars' potential wells (located at x_1 and x_2).

where the stars of mass M_1 and M_2 are located at x_1 and x_2, respectively, such that the centre of mass is at the origin. Also, $r^2 = x^2 + y^2 + z^2$ and Ω is the angular velocity of the rotating reference frame. Figure 2.4 shows the equipotentials in the equatorial plane (i.e. z=0) described by Equation 2.3 for a binary with a mass ratio $q_1 \equiv M_1/M_2 = 2$, where M_1 and M_2 are the masses of the *initially* most and least massive stars, respectively. Note that there does not seem to be any clear convention on the definition of the mass ratio q as some authors use the more evolved star as the primary even though it might not be the more massive. Here, we use the notation of Eggleton (2006), as defined above. Close to each star, the equipotentials are circular, as one would expect for a single star. As we move further away from the stars, the gravitational contributions from both stars become non-negligible

and deform the equipotentials. The first equipotential that surrounds both stars is called the Roche Lobe (Édouard Albert Roche, 1820-1883), and forms a surface within which a star's potential dominates over its companion's. The Roche lobe intersects on a line joining the two stars at a point called the first Lagrange point, L_1. The second panel of Figure 2.4 shows the potential along the line connecting the two stars and clearly highlights the potential well created by each star as well as the potential wall separating the two stars. Lagrange had already noted that binaries generate equipotentials with five extrema; the first three points lying on the line joining the two stars and L_4 and L_5 at the tip of triangle with the base formed by the line joining the two stars. At these points, and in particular at the L_1 point, the *net* force on a test particle is zero. Therefore, if, for any reason, the radius of a star increases to overfill its Roche lobe, matter can be transferred into the secondary's potential well and be eventually accreted.

Although the Roche lobe is obviously not spherical, it is possible to define a radius R_L, called the Roche lobe radius, as the radius of a sphere with a volume equivalent to the volume of the (non-spherical) Roche lobe surface. Eggleton (1983) approximates it, to an accuracy of 1% over the whole range $0 < q_1 < \infty$, by

$$\frac{R_{L_1}}{a} \approx \frac{0.49 q_1^{2/3}}{0.6 q_1^{2/3} + \ln(1 + q_1^{1/3})}, \tag{2.4}$$

A rather simpler but cruder approximation also often used, correct to $\sim 3\%$ in the range $0 < q_1 < 0.8$, is given in Paczyński (1971):

$$\frac{R_{L_1}}{a} \approx 0.462 \Big(\frac{M_1}{M}\Big)^{1/3} = 0.462 \Big(\frac{q_1}{1 + q_1}\Big) \tag{2.5}$$

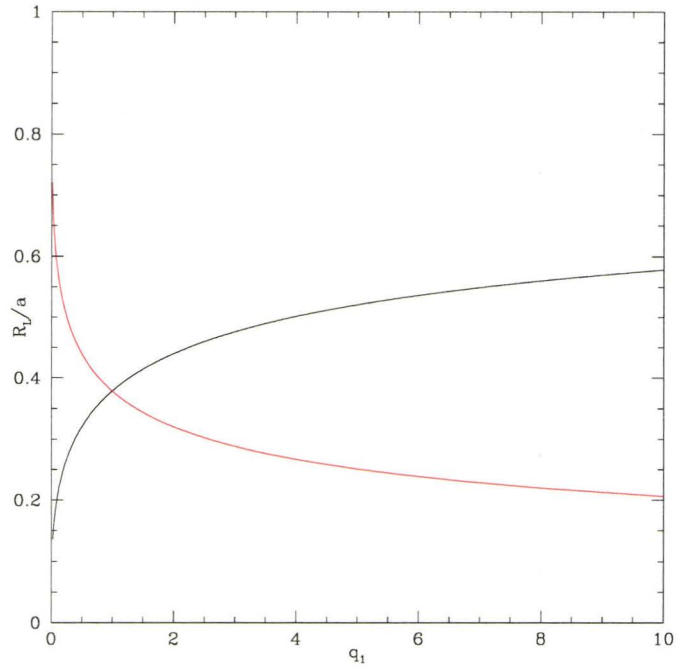

Figure 2.5 Roche lobe radii for the primary (black) and secondary (red) as a function of the mass ratio q_1, as described by Equation 2.4.

The Roche lobe radius of the secondary star can be obtained by using $q_2 \equiv 1/q_1$. Figure 2.5 shows the relationship between the Roche lobe radius and the mass ratio. We can see (1) that the Roche lobe radius increases as the separation and the mass ratio increases and (2) that it is always larger for the more massive star. Moreover, it is always only a fraction of the actual separation; only when the mass ratio gets very small does the Roche lobe radius (of the secondary) becomes comparable to the orbital separation.

There are many ways a star can be brought to fill its Roche lobe. First, as stars go through their nuclear life and run out of nuclear fuel, their hydrostatic structure changes as they go up the red giant branch (RGB) and they expand, sometimes by many orders of magnitude. This alone can cause a star to overfill its Roche lobe, without even changing the orbital separation.

Second, orbital shrinkage due to the loss of angular momentum can also cause stars to fill their Roche lobes. The most commonly invoked sources of angular momentum loss are stellar winds, gravitational wave radiation and magnetic braking. The last two mechanisms operate most effectively for close and compact binaries. Third, close fly-bys or captures of stars leading to the formation of (eccentric) binaries might bring two stars close enough (momentarily) for one of them to fill its Roche lobe and facilitate mass transfer.

In any case, once a star fills its Roche lobe and loses mass, we describe the situation as one involving mass transfer. Mass transfer between stars can significantly alter the properties and evolution of both stars, and the outcome of such binary evolution depends, among other things, on when, in the life of a star, mass transfer occurs. Kippenhahn & Weigert (1967) (see also Lauterborn 1970) were the first to make such a distinction and identified three main cases of mass transfer. Case A considers the evolution of a star overfilling its Roche lobe while still on the main sequence whereas case B treats the evolution of a star that has exhausted hydrogen in its core but has not yet reached the tip of the red giant branch, where helium fusion starts. Finally, case C deals with mass transfer in stars that have terminated core helium burning and reached the asymptotic giant branch (AGB) phase. The importance of such a distinction lies in (1) the composition of the donor star at the moment of mass transfer and (2) the structure and different responses of the donor star upon mass transfer.

2.2.2 Mass transfer: rate and stability

Once a star overfills its Roche lobe, mass is transferred to the companion's potential well. The rate at which mass is being transferred is, in general, a strong function of the degree of overflow of the donor, $\Delta R = R_1 - R_L$. Using simple physical assumptions and arguments, estimates for the mass transfer rates can be derived. In general, mass is assumed to be transferred through the L_1 point, and the flux of mass, or the rate, can be simply described by

$$\dot{M}_1 = -\rho_L v_s \sigma_{cross} \tag{2.6}$$

where ρ_L is the density of the star at the L_1 point, v_s is the sound speed and σ_{cross} is the cross section of the stream of matter. As shown below, it is possible to estimate these three quantities, and the reader is referred to Gokhale et al. (2007) and references therein for more details. The density at L_1 can be estimated by using Bernoulli's theorem, which states that the following quantity is conserved along any streamline for an inviscid fluid:

$$\frac{1}{2}v^2 + \int \frac{dP}{\rho} + \Phi = C \tag{2.7}$$

where C is a constant and the integral is to be taken along any streamline, from a reference point to the point under consideration. Considering an isothermal flow around the first Lagrangian point and making use of the ideal gas pressure law, $P = \rho KT/\mu m_H$, one can show that

$$\rho_L = \frac{1}{\sqrt{e}}\rho_{\rm ph}\exp\Big(-\frac{\phi_L - \phi_{\rm ph}}{v_s^2}\Big), \tag{2.8}$$

where $\rho_{\rm ph}$ and $\phi_{\rm ph}$ are the photospheric values for the density and the gravitational potential, respectively. Furthermore, we assume that the $v_{\rm ph} \ll v_L \simeq v_s$. Following Ritter (1988), estimates for $\phi_L - \phi_{\rm ph}$ can be obtained by expanding the Roche potential in terms of the Roche lobe and photosphere radii, R_L and $\mathrm{R}_{\rm ph}$, respectively, yielding a mass transfer rate equal to

$$\dot{M}_1 = -\dot{M}_0 \exp\Big(\frac{R_{\rm ph} - R_L}{H_p}\Big) \tag{2.9}$$

where H_P is the pressure scale height of the donor star in the Roche potential and $\dot{M}_0 \equiv \rho_{\rm ph} v_s \sigma_{cross}/\sqrt{e}$ is the mass transfer rate of a star exactly filling its Roche lobe. As expected, the mass transfer rate depends rather strongly on the degree of overflow ΔR and goes to zero exponentially if the star is within its Roche lobe. Ritter (1988) provides estimates for $\dot{M}_0$ of about 10^{-8} $\mathrm{M}_\odot \mathrm{yr}^{-1}$ and $H_P/R \simeq 10^{-4}$ for low-mass main-sequence stars. This model of mass transfer has been successfully applied to cataclysmic variables where the photosphere of the donor is located about one to a few pressure scale heights inside the Roche lobe, i.e. $R_L - R \gtrsim H_P$. Moreover, this shows that the finite extension of a star's photosphere should be accounted for when modeling stellar systems as mass transfer can still be achieved even when the observable surface of a star is within its own Roche lobe.

For cases where the mass transfer rates are much larger, Paczyński & Sienkiewicz (1972) (see also Eggleton 2006 and Gokhale et al. 2007) derived, in a similar way, the mass transfer rate in the case where the donor can be approximated by a polytrope of index n. In such cases, the mass transfer rate is

$$\dot{M}_1 = -\dot{M}_0 \Big(\frac{R - R_L}{R}\Big)^{n+3/2} \tag{2.10}$$

where $\dot{M}_0$, a canonical mass transfer rate, is a smooth function of M_1, M_2, and a and is approximately equal to M_1/τ_{HD} for an n=3/2 solar polytrope, where τ_{HD} is similar to the hydrodynamical timescale (Eggleton, 2006). This rate is equally zero when $\Delta R \leq 0$. The dependence of the mass transfer rate on $(\Delta R/R)$ is again found, although somewhat different than that of Ritter (1988). This mass transfer rate is applicable when the degree of overflow is much larger than the pressure height scale and happens on a dynamical timescale. It is generally referred to as the adiabatic mass transfer rate.

In any case, stars respond to mass loss by readjusting their structure on different timescales, and this response is crucial to the subsequent evolution of the system. Indeed, as we just saw, mass transfer rates depend on the degree of overflow of the donor star. However, the structure readjustment of the donor star as well as the change in the mass ratio q can change both the radius of the star, R_1, and the Roche lobe radius, R_L, and therefore the mass transfer rate. Let's consider different responses of the binary parameters that can affect the degree of overflow (Soberman, Phinney, & van den Heuvel 1997; Tout 2008). First, upon mass transfer, hydrostatic equilibrium is broken and a star quickly readjusts its structure on a dynamical timescale. We quantify this with the following parameter:

$$\zeta_{ad} = \left(\frac{\partial \ln R_1}{\partial \ln M_1}\right)_{s,X} \tag{2.11}$$

which addresses the rate of change of the radius upon mass loss (i.e. $\partial \ln M < 0$) for constant entropy and composition. It is negative for stars which are expanding and positive for stars which are shrinking. The dynamical response of the envelope of a star depends whether it is radiative or convective. Stars

with masses $\gtrsim 1.25$ $M_\odot$ have a radiative envelope which shrinks upon mass loss ($\zeta_{ad} > 0$; Morton 1960) whereas stars with $0.35 \lesssim M/M_\odot \lesssim 1.25$ have deep convective envelopes and expand upon losing mass ($\zeta_{ad} < 0$; Paczyński 1965). On the other hand, stars in thermal equilibrium also readjust their structure upon mass loss, although on a longer, thermal timescale. We can define the following parameter:

$$\zeta_{th} = \left(\frac{\partial \ln R_1}{\partial \ln M_1}\right)_X. \tag{2.12}$$

For unevolved main-sequence stars, $\zeta_{th} > 0$, while for red giants $\zeta_{th} < 0$. Thermal equilibrium states that the energy flux through any surface must be constant. For example, upon losing mass a radiative star contracts on a hydrodynamical timescale, which causes pressure and temperature to suddenly increase. This increase in temperature increases the rate of energy generation, and hence temperature, and the star expands again, until equilibrium is reached. Finally, as mass is being transferred, the mass ratio is also slightly modified, which inevitably changes the Roche lobe radius. We thus define the following exponent:

$$\zeta_L = \left(\frac{\partial \ln R_{L_1}}{\partial \ln M_1}\right)_{M,J}, \tag{2.13}$$

which is approximated by Eggleton (2006) by $\zeta_L = 2.13q_1 - 1.67$. This function is positive for $M_1 > 0.784M_2$, which, for a mass-losing primary, implies that the Roche lobe shrinks upon mass transfer (and expands for $M_1 < 0.784M_2$). A positive value of any of these mass-radius exponents means the star shrinks upon mass transfer and a negative value implies the star expands. The larger the absolute value of the exponent, the faster the response of the star.

It is the relative value of these three derivatives that dictates the evolution and stability of the mass transfer. If the star's radius increases faster than

the Roche lobe, then the mass transfer rate increases rapidly. On the other hand, if a star can maintain its radius at the Roche lobe radius, mass transfer will proceed smoothly and stably. The competition between these processes actually dictates the mass transfer stability. If $\zeta_L > \zeta_{ad}$, then the Roche radius shrinks faster than the radius of the star, and mass transfer grows rapidly and becomes unstable. If $\zeta_L < \zeta_{ad}$ but $\zeta_L > \zeta_{eq}$, then the initial adiabatic response of the star is to shrink below the Roche lobe on a dynamical timescale and to slowly readjust its thermal equilibrium on a (longer) thermal timescale and overfill its Roche lobe. Finally, if $\zeta_{ad} > \zeta_L$ and $\zeta_{eq} > \zeta_L$, the star always contracts faster than the Roche lobe and mass transfer fades, unless subsequent evolution or losses of angular momentum cause the star to fill its Roche again. The response of the Roche lobe radius upon mass transfer, coupled with the different responses of a star's radius, which can all occur on timescales ranging from a few hours to billions of years, inevitably make the modeling of mass transfer a challenging problem.

2.2.3 Orbital evolution due to mass transfer

As expressed by Equation 2.4, the Roche lobe is not only a function of the mass ratio q but also a function of the orbital separation. As one might expect from Kepler's third law of orbital motion, if the total mass of the system changes, the orbital period and the orbital separation ought to change. In order to better understand how these quantities evolve upon mass transfer, we can write the total angular momentum of a system of two point masses orbiting around their centre of mass and for which the spin contributions are

negligible as

$$L_{tot} = \mu r v = M_1 M_2 \left[\frac{Ga(1-e^2)}{M_1+M_2}\right]^{1/2} \tag{2.14}$$

where G is the gravitational constant, a the semi-major axis of the orbit, and e the eccentricity. Taking the time derivative yields

$$\frac{\dot{L}_{tot}}{L} = \frac{\dot{M}_1}{M_1} + \frac{\dot{M}_2}{M_2} - \frac{1}{2}\frac{\dot{M}}{M} + \frac{1}{2}\frac{\dot{a}}{a} - \frac{e\dot{e}}{1-e^2} \tag{2.15}$$

On the other hand, taking the time derivative of Kepler's third law yields

$$\frac{\dot{P}}{P} = -\frac{1}{2}\frac{\dot{M}}{M} + \frac{3}{2}\frac{\dot{a}}{a} \tag{2.16}$$

which allows us to rewrite Equation 2.15 as

$$\frac{\dot{L}}{L} = \frac{\dot{M}_1}{M_1} + \frac{\dot{M}_2}{M_2} + \frac{\dot{P}}{P} - \frac{\dot{a}}{a} - \frac{e\dot{e}}{(1-e^2)} \tag{2.17}$$

Equations 2.15 and 2.17 show that as the masses of the stars change and as mass and angular momentum are being lost from the system, both the orbital separation and the eccentricity change. The exact behaviour of these quantities depends of course on the degree of conservation of both total mass and total angular momentum.

For close binaries, it is generally assumed that tidal circularization occurs on timescales short enough that one can make the assumption that the orbit has circularized upon the start of mass transfer. For example, Tout (2008) gives an estimate of the circularization timescale for convective stars

with orbital separation a and radius of the largest star, R:

$$\tau_{circ} \approx \frac{2q_1^2}{1+q_1}\left(\frac{a}{R}\right)^8 \text{yr}. \tag{2.18}$$

This timescale can be as short as a few thousand years for close or overflowing systems, and it has generally been assumed that binaries have circularized at the moment of first contact. Furthermore, synchronization timescales are even shorter, and are approximated by

$$\tau_{sync} \approx q_1^2\left(\frac{a}{R}\right)^6 \text{yr}. \tag{2.19}$$

(Tout, 2008). Therefore, making the assumption of circular orbits reduces Equation 2.15 to

$$\frac{\dot{L}_{tot}}{L} = \frac{\dot{M}_1}{M_1} + \frac{\dot{M}_2}{M_2} - \frac{1}{2}\frac{\dot{M}}{M} + \frac{1}{2}\frac{\dot{a}}{a} \tag{2.20}$$

The total angular momentum in a (closed) system of two stars should be conserved, although some can be removed and lost by different mechanisms. In some instances, orbital angular momentum is removed by the emission of gravitational waves, mass loss through stellar winds, and magnetic braking. These mechanisms for removing angular momentum are functions of orbital separation and mass ratio, so only close binaries actually significantly suffer from them. Furthermore, here, we have neglected the spin contributions to the total angular momentum, although at short enough periods, their contributions may become significant. We will not discuss this contribution, but the interested reader is referred to, among others, Motl, Tohline, & Frank (2002); Sepinsky et al. (2007b, 2009).

2.2.4 Conservative mass transfer

Another assumption often used is that of conservative mass transfer, where both total mass and total angular momentum are conserved within the binary system. This is expressed as $\dot{M}_1 = -\dot{M}_2$ and $\dot{L}_{tot} = 0$. Equation 2.20 therefore reduces to

$$\frac{\dot{a}}{a} = 2\frac{\dot{M}_1}{M_1}\Big(1 - \frac{M_2}{M_1}\Big). \tag{2.21}$$

Since M_1 is assumed to be the donor (i.e. $\dot{M}_1 < 0$) and more massive star ($M_1 > M_2$), we get that, upon mass transfer, that the separation a decreases until we have mass ratio reversal, at which point the separation starts increasing again. This suggests that for main-sequence binaries, where the most massive is always the largest, thus the one losing mass, the separation decreases and the mass transfer is self-enhanced, even more so if the stars are convective and expand upon mass transfer.

As an example of how the degree of overflow can be determined analytically, we note that the following mass-radius relation holds for low-mass convective stars and non-relativistic white dwarfs:

$$R \propto M^{-1/3}. \tag{2.22}$$

Using Equation 2.5 for the Roche radius, and taking the respective time derivatives, one can show that the degree of contact is approximately given by

$$\frac{\dot{R} - \dot{R}_L}{R} \approx \frac{\dot{R}}{R} - \frac{\dot{R}_L}{R_L} = -2\frac{\dot{M}_d}{M_d}\Big(q_1 - \frac{2}{3}\Big). \tag{2.23}$$

where M_d is the mass of the donor star. Thus, since we assume the primary to be the donor, we get that the degree of overflow increases for $q_1 > q_{crit} = 0.666$.

Similarly, Tout (2008) gets $q_{crit} = 0.7$. Therefore, for $q_1 < q_{crit}$, mass transfer can proceed stably.

Stars probably do not accrete all the material that falls within their Roche lobe, however, as their structure has to readjust on a thermal timescale to the infalling material. If the rate is too fast, matter then just piles up around the secondary and possibly fills the Roche lobe, thus forming a common envelope around the whole system. It is conceivable that mass transfer is non-conservative, therefore making the orbital evolution more complicated to treat correctly analytically.

2.3 Eccentric binaries

Most of the theoretical background just derived applies only to circular orbits, which are a rather idealized study case. As discussed in §2.1, short-period binaries are mostly all on circular orbits, but many relatively close binaries also have eccentric orbits. In such eccentric binaries, mass transfer rates are not constant since the orbital separation continuously changes, and one could argue that Roche lobe overflow occurs periodically at periastron, when the two stars are closest to each other. This early phase of mass transfer arguably could create more semi-detached or contact systems than circular binaries alone and, to some extent, change the overall population of exotic stars of binary origin. This could especially be true in dense clusters where the formation of eccentric binaries through captures is more likely. However, the orbital evolution (i.e. orbital separation and eccentricity) of such binaries is still not well understood and constrained. In particular, a theoretical description of mass transfer in eccentric systems is not straightforward as the Roche lobe approximations of

circular and synchronous orbits cannot be used. One must therefore rely on other approximations to get the Roche lobe radius and estimate the rate of mass transfer. In this section, we review the current understanding of mass transfer and orbital evolution of eccentric binaries and emphasize on the need for better models in order to improve it.

2.3.1 Roche lobe and equipotentials

The study of non-synchronized, eccentric binaries has only recently been revived by Sepinsky et al. (2007a), who showed, analytically, that eccentric systems can evolve quite differently from circular binaries. First, the estimated radius of the Roche lobe for eccentric binaries can be smaller (or larger) than in the circular case, possibly allowing mass transfer to start earlier. This is shown in Figure 2.6, where the Roche lobe radius (normalized to the Roche lobe radius for the circular and synchronous case) for different values of the mass ratio q. The function $\mathcal{A}(f, e, \nu)$ characterizes the degree of asynchronism and depends on the ratio of rotational to orbital angular velocities at periastron (f), the eccentricity, and the true anomaly, ν, i.e. the angular position along the ellipse with respect to the primary focus and periastron. This function is directly proportional to f^2, and for circular and synchronized (i.e. f=1) orbits, we have $\mathcal{A}(f, e, \nu) = 1$. From Figure 2.6, we see that the Roche lobe radius can be smaller by more than 20% from that of the circular case for binaries with mass ratios close to unity rotating faster than the orbital velocity at periastron($f > 1$). The reverse is also true as binaries rotating slower than the orbital velocity at periastron ($f < 1$) can have a Roche lobe radius $\sim 10\%$ *larger* than the circular case. Second, depending on the degree of asynchronic-

ity and eccentricity, the geometry of the equipotential surfaces may change and allow mass to be ejected from the system through the L_1 point. Indeed, unlike for circular binaries, it is found that the usual Roche lobe can sometimes open up around the secondary star, potentially allowing any mass passing the L_1 point to leave the system. Moreover, in some cases, the potential at the L_3 point can be only slightly larger than that at the L_1 point, possibly also allowing for more mass to be lost from the system by that additional route. When this happens, generally for values of the function $\mathcal{A} \gtrsim 1.5$, we speak of non-conservative mass transfer. Although we expect mass to be ejected from almost any mass-transferring binary system, it is hard to estimate how much is

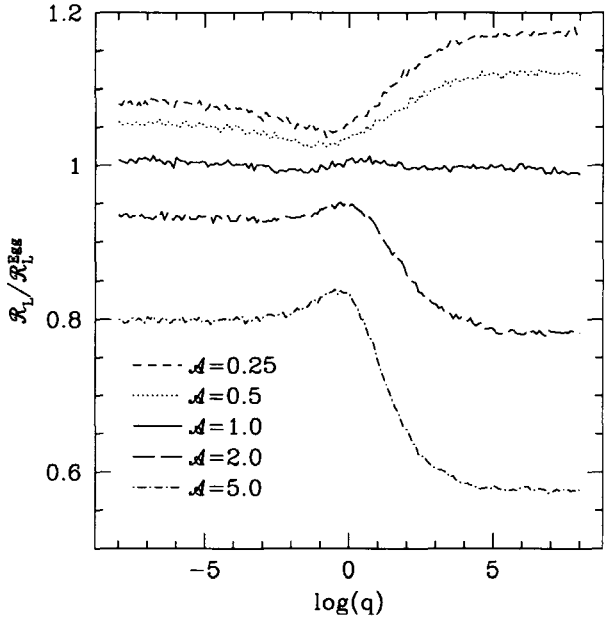

Figure 2.6 Roche lobe radius at periastron for the eccentric and asynchronous case normalized by the Roche lobe for the circular case as a function of the mass ration $q_1 = M_1/M_2$. The function $\mathcal{A}$ describes the degree of asynchronism. Circular and synchronous binaries have $\mathcal{A} = 1$, sub-synchronous binaries have $\mathcal{A} < 1$, and super-synchronous binaries have $\mathcal{A} > 1$. Taken from Sepinsky et al. (2007a).

actually lost and authors have generally used some parameterization to study the effect of non-conservative mass transfer on the evolution of mass transfer (Sepinsky et al., 2009) (hereafter, SWKR09). These results strongly suggest that eccentric and asynchronous binaries will likely undergo mass transfer during an earlier phase of their life (compared to circular binaries) and that the latter is likely to be non-conservative. These findings conceivably could alter the evolution of eccentric binaries in a different way than in the idealized circular case.

To emphasize on the need for better, more realistic models for binary stars, Dermine et al. (2010) studied the effect of radiation pressure on the shape of the equipotential surfaces of *circular* and *synchronized* binaries. Despite the idealized conditions assumed in this work (i.e. circular and synchronized), the addition of an extra terms in the potential equation (Eq. 2.3) significantly modifies the shapes of the equipotentials. As can be seen in Figure 2.7, which shows the equipotential contours in the orbital plane as derived from the potential described in Dermine et al. (2010), the shapes of the equipotentials become similar to those of the eccentric and asynchronous case discussed above. Each panel of Figure 2.7 uses a different values of the parameter f, the ratio of radiative force to the gravitational force. As in the case of eccentric binaries (see Figure 7 of Sepinsky et al. 2007a), the inner Roche lobe opens up for values of f greater that ~ 0.5, potentially allowing for mass transferred through the L_1 point to leave the system. Moreover, Figure 2.7 shows that for value of $f \gtrsim 0.5$, matter may leave one star through the L_3 point before even reaching the potential of the L_1 point. Radiation pressure becomes important for stars of spectral type around $A5V$ and earlier (Dermine et al., 2010). On the other hand, radiation pressure is not very important in the atmosphere of low-mass

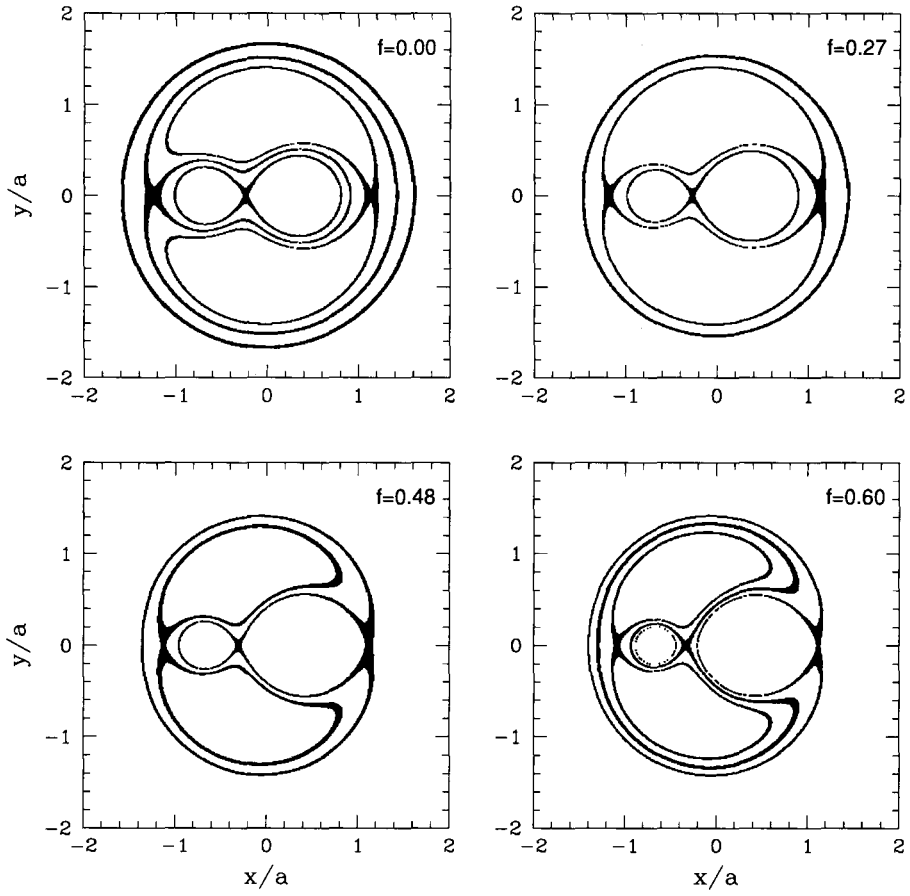

Figure 2.7 Equipotential contours for a $q_1 \equiv M_1/M_2 = 2$ binary system in which the radiative acceleration is taken into account with the parameter f, the ratio of the radiative to gravitational accelerations. The upper left panel with $f = 0$ corresponds to the classical Roche model. The extra term in the potential due to radiation pressure can modify significantly the shape of the equipotential surfaces. Adapted from Dermine et al. (2010).

stars, as the ratio of radiative acceleration to gravitational acceleration (f) is of the order of 10% or less (see Table 2 in Dermine et al. 2010). The authors also find that the contribution from radiative pressure to the potential also leads to a decrease, for all mass ratios, of the Roche radius. For the most extreme radiation fields, the estimates for the Roche radius can be a factor up to about two smaller. This work emphasizes again that the classical Roche

model does not strictly apply in most instances and that the addition of more realistic physical ingredients (e.g. asynchronism, eccentricity, radiation pressure) into the binary star model changes the results significantly from those of the idealized case of circular orbits.

2.3.2 Secular evolution

Analytical studies seem to suggest that, in most instances, the suitable and convenient circular and synchronized Roche model does not apply. Based on these conclusions, Sepinsky et al. (2007b) (hereafter, SWKR07) and SWKR09 went on to the study (analytically) the secular evolution of eccentric binaries due to episodic mass transfer. They further constrained their study by assuming a delta function for mass transfer ($\dot{M}_0 = 10^{-9}$ $M_\odot$/yr) centered at periastron and considered both conservative and non-conservative mass transfer. The authors find that depending on the mass ratio and eccentricity, the secular changes of orbital separation and eccentricity can be positive or negative, and can occur on timescales ranging from a few million years to a few billion years. Moreover, these timescales can, in some cases, be comparable to the orbital evolution timescales due to tidal dissipation and be additive or competitive with the latter. The total orbital evolution timescales, in Gyrs, for the orbital separation (τ_a) and eccentricity (τ_e) are shown in Figure 2.8 as contours for the conservative mass transfer scenario. The thick black line delimits regions where the orbital separation and eccentricity increase (left) and decrease (right). The break around q=0.87 (for a companion of mass 1.44 $M_\odot$) corresponds to the different tidal dissipation mechanism operating in stars of mass below and above $\sim$ 1.25 $M_\odot$. For example, the left panel of Figure 2.8

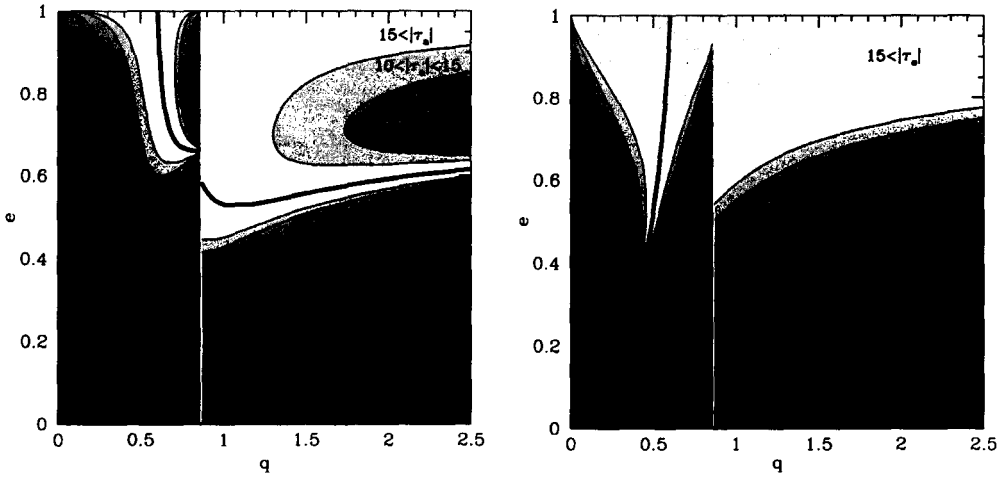

Figure 2.8 Contour plots of the orbital evolution timescales in Gyrs for the orbital separation (left) and eccentricity (right) under a (conservative) mass transfer rate of 10^{-9} $M_{\odot}$/yr and tidal dissipation for a binary with a 1.44-$M_{\odot}$ secondary. The thick black line delimits the regions of positive (left) and negative (right) rates of change of the quantity plotted whereas the vertical white line at q$\simeq$ 0.87 corresponds to a transition between the dominant tidal dissipation mechanism, which occurs around 1.25 $M_{\odot}$. Taken from Sepinsky et al. (2007b).

shows that for any eccentricity smaller that ~ 0.55, the orbital separation always increases, whereas for mass ratios greater than ~ 0.6 and eccentricities larger than ~ 0.55, the orbital separation decreases. The right panel of Figure 2.8 show, on the other hand, that for systems with mass ratios smaller than ~ 0.6, the eccentricity can increase, depending on the initial eccentricity. As expected, the timescales for circularization are longer for more eccentric binaries, and for systems with $e \gtrsim 0.6$, can be longer than 5 Gyrs. Thus, based on these findings, the authors suggest that the usual rapid circularization assumption is not always applicable and, in some cases, very unlikely. Note that the rates of secular evolution for a and e are directly proportional to the mass transfer rate, although the latter is poorly constrained. Moreover, SWKR09 concluded that relaxing the assumption of conservative mass transfer does not

change the overall conclusions of their previous work (SWKR07).

As mentioned above, these orbital evolution timescales scale linearly with the assumed mass transfer rate and, as one might expect, mass transfer probably does not happen right at periastron but rather over a finite extended period of time before and after the periastron passage. Furthermore, these refinements in the evolution of binary stars are generally not taken into account in stellar population synthesis and N-body codes nor have they been quantified and studied thoroughly in the past, and one could argue that they are important if one wants to get a better and more realistic picture of exotic stellar populations.

2.4 Stellar population synthesis and N-body codes

N-body codes (e.g. Aarseth, Tout, & Mardling 2008) are used to model and evolve systems of stars acted upon by external gravitational potential and self-gravity over galactic timescales. Along with dynamics, stars can also be evolved by introducing a simplified treatment of stellar evolution for both single and binary stars. Binaries are either primordial or formed dynamically through captures (by single or binary stars) and can be evolved and followed for long periods of time. Their evolution can not be fully (hydrodynamically and dynamically) modeled as it would require too many resources; rather, binary stars are evolved using physics first principles and binary stellar evolution prescriptions. N-body codes physically incorporate prescriptions for a large variety of stellar phenomena such as supernova and white dwarf natal

kicks, stellar collisions, angular momentum loss mechanisms, and close binary interactions such as mass transfer and common envelope evolution. Similarly, (binary) stellar population synthesis codes (e.g. Han et al. 2001) can model the evolution of a much larger number of stars without modeling their dynamics, hence allowing for faster computing of many different stellar populations. A simplified treatment of dynamics can be introduced however (e.g. Ivanova et al. 2005). Among others, Portegies Zwart & Verbunt (1996) and Hurley et al. (2002) (the `SeBa` and `BSE` binary evolution algorithms, respectively) have built algorithms for binary star evolution that can be incorporated into `N`-body codes. The treatment of close binaries in these codes is based on the approximation that evolution under tidal dissipation occurs relatively fast (see Equations 2.18 and 2.19), which allows for the use of the the Roche model for circular and synchronous binaries and the determination of the Roche radius R_L (see Equation 2.4) for stars approaching a contact phase. The use of this approximation also allows for the mass transfer rate to be estimated (see §2.2.2). For the case of eccentric orbits, the binaries are either subjected to instant synchronization (Hurley et al., 2002) or considered synchronized *and* circular at the onset of mass transfer (Portegies Zwart & Verbunt, 1996). Note that the use of this approximation, by construction, always yields to a decrease of the eccentricity with time as mass transfer takes place (i.e. $\dot{e}/e < 0$).

However, as discussed in §2.3.2, binaries can remain on eccentric orbits for much longer than what suggested by Equations 2.18 and 2.19 when mass transfer occurs only periodically. In such cases, the Roche radius is difficult to determine and the degree of overflow and the mass transfer rates are therefore hard to estimate. One way to get these estimates is by using hydrodynamical simulations, although only a handful of such simulations have been done.

2.5 Previous simulations of mass transfer in binary systems

To get a quantitative picture of mass transfer in binaries, it is better to use hydrodynamics. Although not suited for long, thermal- or nuclear-timescale simulations, hydrodynamical simulations can be useful for studying transient phenomena and episodes of stable mass transfer. Simple ballistic models (e.g. Warner & Peters 1972; Lubow & Shu 1975; Flannery 1975) and two-dimensional hydrodynamical simulations of semi-detached binaries (e.g. Sawada et al. 1986; Blondin et al. 1995) have generally been used in the past to study the general characteristics of the flow between two stars and the properties of accretion disks. Later three-dimensional models with higher resolution allowed for more realistic studies of coalescing binaries (e.g. Rasio & Shapiro 1994, 1995) and accretion disks in semi-detached binaries, all mainly focusing on the secular and hydrodynamical stability of binaries and on the structure of the mass transfer flow. More recently, Motl, Tohline, & Frank (2002) and D'Souza et al. (2006) used grid-based hydrodynamics to simulate the coalescence of fully-modeled $n = 3/2$-polytropes, representative of low-mass white dwarfs (i.e. $M \lesssim 1.0\ M_\odot$) and low-mass main-sequence stars (i.e. $M \lesssim 0.5\ M_\odot$). They also investigated the onset of dynamical and secular instabilities in close binaries and were able to get a quantitative agreement with theoretical expectations (as derived in §2.2.3), although the authors warn that their results may depend on the nonlinear development of these instabilities and that their conclusions should not be taken as definitive.

As for the hydrodynamics of eccentric binaries, only a few authors have investigated it. Regös et al. (2005) (see also Layton et al. 1998) studied the

shape of the equipotential surfaces in eccentric binaries using both analytical and numerical (SPH) approaches. Their findings agree with those of Sepinsky et al. (2007a), in that they find that mass can be lost from the L_2 point. However, their estimates for the Roche lobe radii are larger and similar to the Roche lobe radii for the circular and synchronized case. Interestingly, the authors also study the onset of mass transfer along the orbit for one binary and different eccentricities. They find that mass can be transferred through the L_1 point close to periastron passages and that some mass leaves the systems, similarly to the conclusions of Sepinsky et al. (2007a). However, the low resolution of these simulations (10,000 particles) does not allow for accurate mass transfer rate determinations. Church et al. (2009) have partially circumvented this problem using a new SPH technique for modeling mass transfer in cataclysmic variables, where the least massive star is losing mass to a compact white dwarf (modeled as a point mass). With the aim of getting better estimates of mass transfer rates, their innovative approach, originally called "oil-on-water", allows the authors to get a high *mass* resolution in the outer parts of the star and therefore resolve low mass transfer rates. Despite using a relatively low number of particles ($\sim 40,000$), most of the stars' mass is contained in a few "water" particles, allowing for the outer, "oil" particles to have a very low mass. By varying the eccentricity and periastron distances for one particular mass ratio ($q_2 \equiv M_2/M_1 = 0.6$), the mass transfer rates they obtain show qualitative behaviour in agreement with that predicted by Ritter (1988) (see Equation 2.9). Interestingly, Edwards & Pringle (1987) performed grid-based hydrodynamics calculations of polytropic semi-detached systems and compared the mass transfer rates to analytical estimates (see §2.2.2), with which they find good agreement. However, their simulations only modeled

a small rectangular box close to the L_1 point and did not encompass either the donor or the accretor and did not assess whether mass was lost from the system.

In most simulations to date, the accreting star is not modeled realistically, often using point masses or boundary conditions to model the surface and the accretion. This failure prevents from drawing any quantitative conclusions regarding (1) the accretion process and (2) the behavior of the accreted material onto the secondary star. Moreover, as pointed out by Sills & Lombardi (1997), the use of polytropes instead of realistic models may lead to significantly different internal structures for collision products, which may arguably be applicable to mass-transferring binaries. Also, in regards to the work of SWKR07 and SWKR09, mass transfer may not only start around periastron, but also continues for longer after the periastron passage (see simulations of Regös et al. 2005; Church et al. 2009). Hence, more work remains to be done in order to better understand how mass transfer operates and affects the evolution of eccentric binary systems.

2.6 Summary

In this chapter, it was shown that eccentricity and asynchonous rotation, as well as radiation pressure, can modify the basic features of (circular) binary systems that have usually been assumed for the study of binary evolution. For example, some of the equipotential surfaces were found to open up under certain circumstances, thus allowing for mass to be transferred and lost more easily. Also, the long-term evolution of such eccentric binaries was found to differ significantly from the circular case. The assumption of rapid circular-

ization does not always hold, which arguably could have a major impact on the statistics of binary populations in population synthesis and N-body codes. Based on these results and on the fact that previous hydrodynamical simulations did not encompass all the details of the mass transfer process, accretor and accretion process, we now propose to improve upon previous work by developing a new and innovative hydrodynamical technique aimed at modeling mass transfer in binary systems which will help better constrain key physical parameters such as mass transfer and accretion rates and mass loss in interacting binaries.

Chapter 3

Computational Method

As discussed in Chapter 2, the hydrodynamical modeling of binary stars can be achieved by a handful of different methods. Stellar evolution and population synthesis codes can evolve models of stars over nuclear timescales, but the fact that most of them are still only one-dimensional and rely on spherical symmetry renders the treatment of mass transfer rather suspect. These codes have usually relied on prescriptions based on physics principles and/or analytical estimates for approximating the mass transfer and accretion rates. For a more realistic modeling of hydrodynamical mass transfer, it is better to use hydrodynamics techniques since they can easily be adapted to model binary systems in three dimensions and physically follow the transfer of mass from one star to the other. However, most hydrodynamics codes have difficultly evolving binary stars for long periods of time (e.g. thermal or nuclear timescales) because the stellar hydrodynamical timescale is usually much shorter than the thermal and nuclear timescales. Also, thermal and nuclear mass transfer can occur at relatively low rates (i.e. $\lesssim 10^{-9} - 10^{-10}$ $M_\odot$ yr^{-1}) and can be dif-

ficult to resolve numerically. Larger mass transfer rates can be achieved in binary stars, although such episodes of mass transfer are not expected to last for long and therefore should be hard to observe. Despite these drawbacks, hydrodynamics still remain the best suited technique to get physical insights and constraints on the physics of mass transfer in binary stars occurring on dynamical timescales, during the amount of material transferred can be substantial. In this chapter, we describe our chosen hydrodynamical technique, namely Smoothed Particle Hydrodynamics, and introduce a new approach for the treatment of boundary conditions that is well suited for the hydrodynamical modeling of relatively low mass transfer rates in binary systems. Our code and the boundary conditions are tested and shown to behave well in the context of mass-transferring binaries.

3.1 Smoothed Particle Hydrodynamics

Hydrodynamics is the study of the motion of fluids under the influence of internal (e.g. pressure and viscosity) and external (e.g. gravitational) forces. The derivation of the basic equations governing the flow of fluids goes back a long time (e.g. Navier 1822; Poisson 1829; Saint-Venant 1843; Stokes 1845) and despite a firm theoretical understanding of simplified systems, different computational techniques have been introduced relatively recently to allow for the study of more complex systems for which an analytical treatment is impossible. One of these techniques, called Smoothed Particle Hydrodynamics (SPH), was introduced by Lucy (1977) and Gingold & Monaghan (1977) in the context of stellar astrophysics. Its relatively simple construction and versatility have allowed for the modeling of many different physical problems such as star

formation (Price & Bate 2009; Bate et al. 1995), accretion disks (e.g. Mayer et al. 2007), stellar collisions (Lombardi et al. 1995; Sills et al. 1997, 2001), galaxy formation and cosmological simulations (e.g. Mashchenko, Couchman, & Wadsley 2006; Stinson et al. 2009; Governato et al. 2009), but also geophysical fluid flows as well as engineering problems (e.g. Benz et al. 1986). Unlike grid-based/Eulerian hydrodynamics, which looks at how the density, for example, changes at one point in space over time, SPH is a Lagrangian technique, meaning that it instead follows the fluid elements as they are pushed around and evaluates the density, for example, at that particles' location. This Lagrangian nature renders the modeling of complex and asymmetric phenomena as well as the implementation of additional physics rather straightforward. Since SPH follows the fluid elements in space, it conserves mass (unlike grid-based methods) and simply accounts for free surfaces. Moreover, SPH has the advantages of being naturally adaptive (as the spatial resolution becomes higher in regions of high density, and vice versa) and easily coupled to N-body or tree methods for gravity calculations. Finally, the spatial domain of interest does not have to be known ahead of time as hydrodynamical quantities are calculated only where particles are found. The code we present here was briefly introduced in Bate (1995) and is based on an earlier version presented in Benz (1990) and Benz et al. (1990). Here, for sake of completeness, we summarize the main constituents of our code; the reader is referred to these early articles for complimentary details.

The basic assumption of SPH is that the value of any smooth function at any point in space can be obtained by averaging over the known values of the function around this point. In its simplest version, this smoothing procedure

can be expressed as

$$f(\mathbf{r}) = \int f(\mathbf{r}\prime)\delta(\mathbf{r} - \mathbf{r}\prime)d\mathbf{r}\prime \tag{3.1}$$

where $\delta(\mathbf{r} - \mathbf{r}\prime)$ is a normalized delta function whose value is zero everywhere except at $\mathbf{r} = \mathbf{r}\prime$, thus yielding $\langle f(\mathbf{r})\rangle = f(\mathbf{r})$. By using a smoother function to do the averaging, we can get the averaged value of the function around $\mathbf{r}\prime$:

$$\langle f(\mathbf{r})\rangle = \int f(\mathbf{r}\prime)W(\mathbf{r} - \mathbf{r}\prime; h)d\mathbf{r}\prime = f(\mathbf{r}) + O(h^2) \tag{3.2}$$

where $W(\mathbf{r} - \mathbf{r}\prime; h)$ is called the smoothing kernel and h is called the smoothing length. The smoothing kernel determines the volume (or spatial extent) over which the averaging is to take place, which in turn is determined by the smoothing length. As discussed at length in Hernquist & Katz (1989) and Benz (1990), approximating $f(\mathbf{r})$ by $\langle f(\mathbf{r})\rangle$ is second-order accurate in h for even kernels. This smoothing procedure is depicted in Figure 3.1 for the case of a discrete distribution of points, where the weighted contribution of neighbouring points is used to determine the averaged value of an arbitrary function at a point in space. As for the kernel, we require that it is normalized to unity, i.e.

$$\int W(\mathbf{r}; h)d\mathbf{r} = 1, \tag{3.3}$$

and that it behaves like a delta function in the limit $h \rightarrow 0$ such that we get

$$\lim_{h\rightarrow 0}\langle f(\mathbf{r})\rangle = f(\mathbf{r}). \tag{3.4}$$

Now, for a discrete distribution of N points, we can write the number density

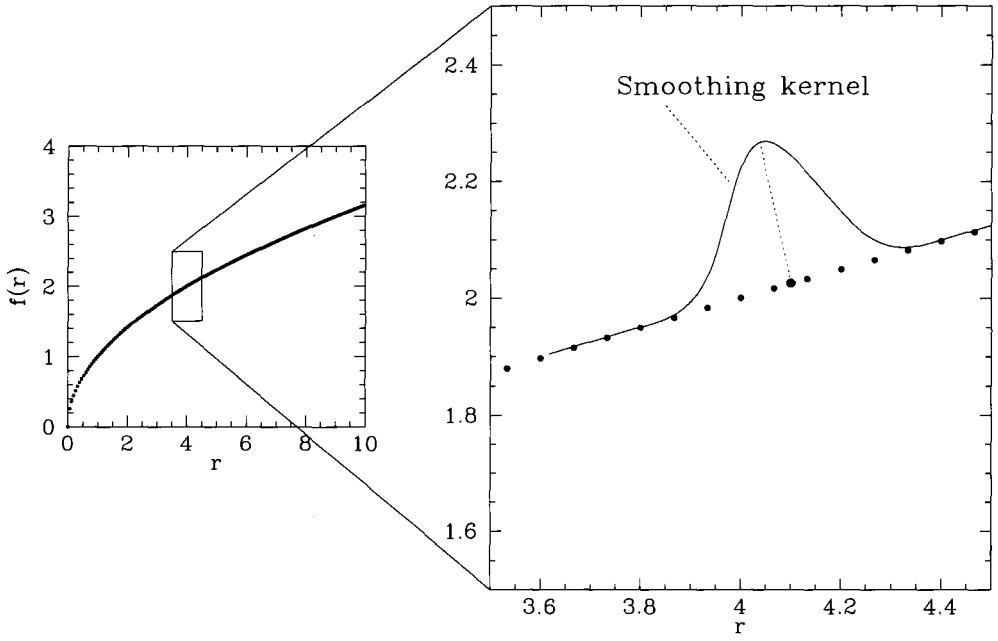

Figure 3.1 The value of a function $f(r)$ represented by a discrete distribution of points (left panel) can be averaged using a smoothing kernel (right panel). At any point $\mathbf{r}\prime$ (e.g. red dot), the smoothing kernel weighs the contribution from the neighbouring points where the value of the function is known to find $\langle f(\mathbf{r}\prime)\rangle$. The height of the smoothing kernel represents the relative weight given to each neighbouring point whereas the width of the kernel is proportional to the smoothing length (h).

as

$$n(\mathbf{r}) = \sum_{j=1}^{N} \delta(\mathbf{r} - \mathbf{r}_j), \tag{3.5}$$

whereas, for a fluid, the *average* number density can also be written as

$$n(\mathbf{r}_j) = \frac{\rho(\mathbf{r}_j)}{m_j} \tag{3.6}$$

where m_j is the mass of each fluid element. Multiplying the integrand in 3.2

by the ratio of these last two equations (which is equal to 1) yields

$$\langle f(\mathbf{r}) \rangle = \sum_{j=1}^{N} \frac{f(\mathbf{r}_j)}{\rho(\mathbf{r}_j)} m_j W(\mathbf{r} - \mathbf{r}_j; h). \tag{3.7}$$

which represents the basic SPH approximation scheme. Essentially, this equation shows that the average value of a function $f(\mathbf{r})$ at $\mathbf{r}$ is determined by summing the weighted contribution of all the neighbouring points j (see Figure 3.1). Choosing, for example, $f(\mathbf{r}) = \rho(\mathbf{r})$ gives the density of an SPH particle:

$$\rho_i = \sum_j m_j W(r_{ij}, h) \tag{3.8}$$

where $r_{ij} = |\mathbf{r}_i - \mathbf{r}_j|$ and where we have dropped the brackets for clarity. The density of an SPH particle can be seen as being the weighted average over all its neighbours. There exist many forms for the smoothing kernel (e.g. Price 2004) that satisfy the normalization condition and the limiting behaviour of a delta function. Exponential and Gaussian kernels have been used in the past but their infinite extension makes them rather computationally expensive to use as the summations must be carried over all particles. To circumvent this problem, we rather use the compact and spherically symmetric kernel first suggested by Monaghan & Lattanzio (1985):

$$W(r,h) = \frac{\sigma}{h^\nu} \begin{cases} 1 - \frac{3}{2}q^2 + \frac{3}{4}q^3 & \text{if } 0 \leqslant q < 1 \\ \frac{1}{4}(2-q)^3 & \text{if } 1 \leqslant q < 2 \\ 0 & \text{otherwise} \end{cases} \tag{3.9}$$

where $q \equiv r_{ij}/h_{ij}$, ν is the number of dimensions, and $\sigma = [2/3, 10/(7\pi), 1/\pi]$ is the normalization constant for the 1-, 2-, and 3-dimensional cases, respectively.

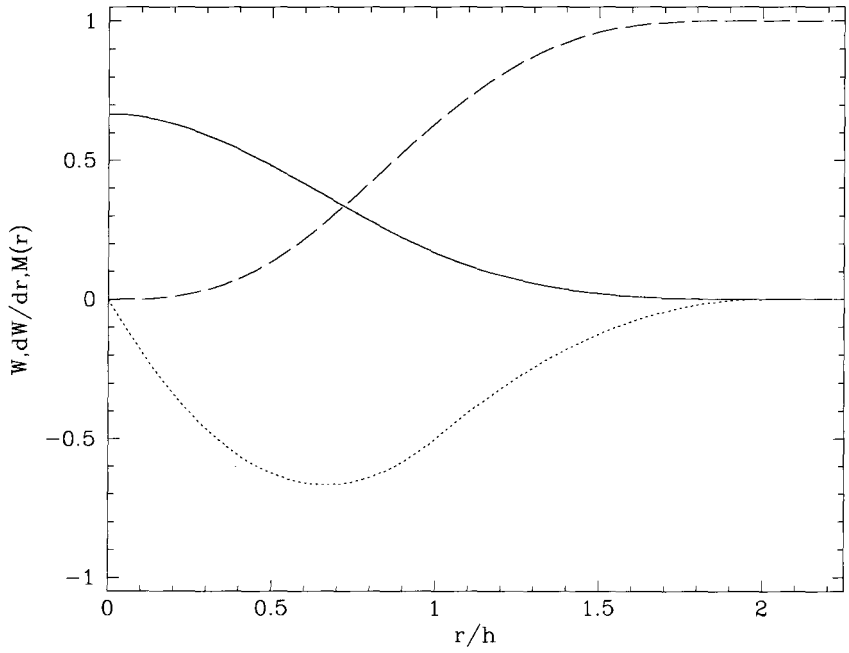

Figure 3.2 The spherically compact kernel first introduced by Monaghan & Lattanzio (1985) (solid line), as well as its radial derivative (dotted line) and the enclosed mass M(r) (dashed line) as a function of the normalized radial distance.

Note that the indices have been dropped for clarity. This kernel is symmetric and, as shown in Figure 3.2, its first derivative is continuous. Moreover, its compact support of size $2h$ limits the calculations only to the particles located within two smoothing lengths of the particle of interest, whereas the contribution from particles located outside $2h$ is identically zero. Finally, one can also understand the smoothing of an SPH particle as a smoothing of its mass within the volume of the kernel. Figure 3.2 also shows the enclosed mass within a particle's volume, which is determined by integrating the kernel from the centre of a particle of mass m to a radius r: $M(r) = 4\pi m \int_0^{r'} W(r', h) r'^2 dr'$.

3.1.1 Hydrodynamics

It is possible to derive the SPH momentum equation from the integral form of the Euler equations for inviscid flows using a similar approach as that derived in §3.1. We write Euler's equation for inviscid fluids as

$$\frac{\partial \mathbf{v}}{\partial t} + (\mathbf{v} \cdot \nabla)\mathbf{v} = -\frac{\nabla P}{\rho} \tag{3.10}$$

which can be rewritten in terms of the Lagrangian derivative as we follow any fluid element as it moves along the fluid flow:

$$\frac{d\mathbf{v}}{dt} = -\frac{\nabla P}{\rho} \approx -\nabla\Big\langle\frac{P}{\rho}\Big\rangle - \frac{P}{\rho^2}\nabla\Big\langle\rho\Big\rangle. \tag{3.11}$$

The last step follows from applying the same method as described in §3.1. More details can be found in Benz (1990). Then, using equation 3.7 on both terms on the right-hand side, we can rewrite the average values as summations over a discrete number of points, yielding, after rearranging the terms, the symmetric form of the SPH momentum equation:

$$\frac{d\mathbf{v}_i}{dt} = -\sum_j m_j\Big(\frac{P_i}{\rho_i^2} + \frac{P_j}{\rho_j^2}\Big)\vec{\nabla}_i W_{ij} \tag{3.12}$$

where the gradient of the kernel ($\vec{\nabla}_i W_{ij}$) is taken with respect to the position of particle i, and $d\mathbf{v}_i/dt$ is the acceleration of particle i. Some other authors have used slightly different expressions for the momentum equation (e.g. Hernquist & Katz 1989) for different reasons. Moreover, this form of the momentum equation conserves linear momentum. This can be shown by taking the time

derivatives of the total momentum,

$$\frac{d\vec{P}}{dt} = \sum_i m_i \frac{d\vec{v}_i}{dt} = \sum_i m_i \Big[- \sum_j m_j \Big(\frac{P_i}{\rho_i^2} + \frac{P_j}{\rho_j^2} \Big) \vec{\nabla}_i W_{ij} \Big], \tag{3.13}$$

which, by noting that $\vec{\nabla}_i W_{ii} = 0$ and $\vec{\nabla}_j W_{ij} = -\vec{\nabla} W_{ji}$, adds up to zero. Similarly, angular momentum is also conserved locally between pairs of particles since the forces are directed along the line joining the centre of the particles. Indeed, we have

$$\frac{d\vec{J}}{dt} = \frac{d}{dt} \sum_i m_i \vec{r}_i \times \vec{v}_i = \sum_i m_i \vec{r}_i \times \frac{d\vec{v}_i}{dt} = 0 \tag{3.14}$$

where the last term is identically zero because the vector from the rotation axis to particle i, $\vec{r}_i$, is parallel to the the vector $d\vec{v}_i/dt$ (more precisely, the vector $\vec{\nabla}_i W_{ij}$), thus nulling the cross product.

3.1.2 Thermodynamics

The thermodynamics of the gas is described using the internal energy equation, which follows from the first law of thermodynamics with no heat source ($\mathrm{d}Q = 0$) and dissipation:

$$du = -PdV = \frac{P}{\rho^2} d\rho \tag{3.15}$$

where du is the change in thermal energy per unit mass, PdV is the work done by the gas during expansion or contraction, and V the volume per unit mass ($V = 1/\rho$). This equation simply states the conservation of energy for an adiabatic process during which no energy enters or leaves the system. Dividing

both side by dt yields

$$\frac{du}{dt} = \frac{P}{\rho^2}\frac{d\rho}{dt}, \tag{3.16}$$

(Price, 2004) and replacing with the time derivative of the density equation (Eq. 3.8), the change in time of the internal energy becomes

$$\frac{du_i}{dt} = \frac{P_i}{\rho_i^2}\sum_j m_j(\mathbf{v}_i - \mathbf{v}_j)\cdot\vec{\nabla}_i W_{ij}. \tag{3.17}$$

The velocity term in equation 3.17 comes from the time derivative of the kernel:

$$\frac{dW_{ij}}{dt} = \frac{\partial W_{ij}}{\partial t} + \frac{\partial W_{ij}}{\partial r_{ij}}\frac{\partial r_{ij}}{\partial t} = (\mathbf{v}_i - \mathbf{v}_j)\cdot\vec{\nabla}_i W_{ij} \tag{3.18}$$

It can be shown that equation 3.17 conserves total energy by taking the time derivative of the total internal energy and showing that it is equal to the change in total kinetic energy. Furthermore, this form of the energy equation does not lead to negative energies for particular situations, unlike other forms of the energy equation (Benz, 1990).

3.1.3 Artificial viscosity

So far, no term in the previous dynamical equations prevents the interpenetration of particles in strong shocks and allows for the dissipation of kinetic energy into heat. This can be accounted for by introducing an artificial viscosity term in the momentum and energy equations. Despite the various forms artificial viscosity can take (e.g. Lombardi et al. 1999), we use the Monaghan

form (Monaghan 1989), which is given by

$$\Pi_{ij} = \frac{-\alpha\mu_{ij}c_{ij} + \beta\mu_{ij}^2}{\rho_{ij}}. \tag{3.19}$$

Here, unless otherwise specified, α and β are constants set to 1.0 and 2.0, respectively (see Lombardi et al. 1999; Bate 1995), and

$$\mu_{ij} = \begin{cases} \frac{(\mathbf{v}_i - \mathbf{v}_j)\cdot(\mathbf{r}_i - \mathbf{r}_j)}{h_{ij}(|\mathbf{r}_i - \mathbf{r}_j|^2/h_{ij}^2 + \eta^2)} & \text{if } (\mathbf{v}_i - \mathbf{v}_j)\cdot(\mathbf{r}_i - \mathbf{r}_j) < 0 \\ 0 & \text{if } (\mathbf{v}_i - \mathbf{v}_j)\cdot(\mathbf{r}_i - \mathbf{r}_j) \geq 0. \end{cases} \tag{3.20}$$

Also, $c_{ij} \equiv (c_i + c_j)/2$ is the mean sound speed defined as $c_i = (\gamma P_i/\rho_i)^{1/2}$ where γ is the heat capacity ratio. Again, this form of the viscosity can be shown to conserve energy as the change in internal energy due to the artificial viscosity is counterbalanced by a change (of opposite sign) of the total kinetic energy. Other forms of artificial viscosity such as that of Balsara (1995) and Hernquist & Katz (1989) offer different advantages. In particular, Balsara's artificial viscosity introduces a switch that turns viscosity on and off in regions of strong compression and large vorticity, respectively. The Balsara artificial viscosity thus has the advantage of being suppressed in shear layers. However, the use of unequal-mass particles (as is the case in this thesis) requires some shear viscosity as spurious motion is observed when massive and light particles interact closely (e.g. Lombardi et al. 1999). We have observed spurious motion in our low-resolution test simulations of single stars and, for this reason, we use Monaghan's viscosity in this thesis as it yields more stable configurations.

The dissipation of energy due to artificial viscosity modifies the momentum and energy equations. With this contribution, equations 3.12 and

3.17 respectively become

$$\frac{d\mathbf{v}_i}{dt} = -\sum_j m_j \Big(\frac{P_i}{\rho_i^2} + \frac{P_j}{\rho_j^2} + \Pi_{ij} \Big) \vec{\nabla}_i W_{ij} \tag{3.21}$$

and

$$\frac{du_i}{dt} = \sum_j m_j \Big(\frac{P_i}{\rho_i^2} + \frac{1}{2}\Pi_{ij} \Big) (\mathbf{v}_i - \mathbf{v}_j) \cdot \vec{\nabla}_i W_{ij}. \tag{3.22}$$

Note that the addition of artificial viscosity in the momentum and energy equations does not affect the conservation properties of the SPH formalism previously discussed.

3.1.4 Self-gravity and neighbours list

For self-gravitating systems, the addition of the gravitational acceleration into the momentum equation (Eq. 3.21) is necessary. The long range over which gravitational force acts makes it necessary, in principle, to sum over all particles, yielding the following contribution:

$$\vec{\nabla}\phi_i = G \sum_{j=1}^{N} \frac{M(r_{ij}, h_{ij})}{r_{ij}^2} \frac{\mathbf{r}_{ij}}{r_{ij}}, \tag{3.23}$$

where $M(r_{ij}, h_{ij})$ is the enclosed mass within a radius r_{ij} from neighbor j. The mass of a particle is smoothed over its volume, as depicted in Figure 3.2, and particles that overlap *feel* only the pull from the mass enclosed between their centre. For particles that do not overlap, the enclosed mass sums up to the total mass of the particles.

Direct N-body summations are extremely costly in terms of CPU time (scaling as N^2), so we use a binary tree, as described at length by Benz et al.

(1990), to calculate the gravitational accelerations from particles outside $2h$ and build the list of nearest neighbours. Note that other methods can also be used to for the calculation of the gravitational acceleration (e.g. oct-tree, grid, FFT; see Wadsley et al. 2004). The binary tree we use searches among all particles for mutual closest neighbours and, upon successfully finding them, forms nodes. A node can be formed of two particles, a particle and a node, or two nodes. In addition, nodes are positioned in space at the centre of mass of the two components under consideration, have mass $M_n = m_i + m_j$ and a radius R_n proportional to $(h_i + h_j)$. The procedure of grouping particles and nodes is repeated until one node remains. The calculation of the gravitational force from each node takes into account the quadrupole moment correction and nodes that satisfy an opening angle criteria are opened up to access the constituents. The criterion for opening the nodes is

$$\frac{R_N}{r_{in}} < \theta \tag{3.24}$$

where r_{in} is the distance between the particle of interest and the node n and θ is a constant set to 0.5 (see Bate 1995). For comparison, an opening angle of $\theta = 0$ implies that all the nodes are opened and translates into a direct N-body calculation. Thus, a given particle will see a small group of close particles — its neighbours — and a number of nodes with increasing size as it looks further away. The use of a binary tree also allows for the creation of a neighbour list for each particle. Nodes which overlap with the particle under consideration are opened up and searched for neighbours located within $2h$. We enforce that the number of neighbors is kept roughly constant at each timestep by adjusting the smoothing length. Typically, every particle has ~ 50

neighbours, but this number is allowed to vary between 30 and 70. Keeping the number of neighbours roughly constant (~ 50) ensures that the properties of the particles are accurately calculated and allows for higher spatial resolution in regions of high densities.

To allow for the smoothing length to vary both in time and space, we use the method suggested by Benz (1990), which is based on the following scaling:

$$h = h_0 \left(\frac{\rho_0}{\rho}\right)^{1/3} \tag{3.25}$$

Taking the time derivative and making use of the continuity equation, we get

$$\frac{dh}{dt} = \frac{1}{3} h \nabla \cdot \mathbf{v}, \tag{3.26}$$

where the divergence of the velocity for particle i is calculated using

$$(\nabla \cdot \mathbf{v})_i = \frac{1}{\rho_i} \sum_j m_j (\mathbf{v}_j - \mathbf{v}_i) \cdot \nabla_i W_{ij}. \tag{3.27}$$

Note, however, that by introducing a spatial- and time-dependent smoothing length, additional terms involving the derivative of h should be included in the momentum and energy equations. As discussed by Benz (1990) and Bate (1995), the omission of these additional terms introduces an error in the calculation of the gravitational potential energy as the smoothed mass distribution of each particle changes with the (evolving) smoothing length. Although this error is taken into account in our code when calculating the gravitational energy (see Benz 1990), it is worthwhile mentioning at this point that some authors have derived a set of (similar) SPH equations from a variational approach that consistently handles these extra terms involving the derivative of

h (see, e.g., Springel & Hernquist 2002; Price 2004; Price & Monaghan 2007).

3.1.5 Equation of state

To relate density and pressure, we assume in this work an equation of state (EOS) for ideal gases of the form

$$P = (\gamma - 1)\rho u, \tag{3.28}$$

where ρ is the density and u is the internal energy per unit mass of a given particle and $\gamma = 5/3$ is the heat capacity ratio. Such a value for γ is appropriate for monatomic gases, and also applies to low-mass stars with a deep convection zone. Other EOS, such as polytropic, isothermal, and variable-gamma (e.g. Bate et al. 1995) can easily be implemented in SPH. Some authors have also used more realistic EOS for modeling compact neutron stars (Rosswog et al., 2004) and rocky materials for the simulation of the formation of the moon upon impact with the Earth (Benz et al. 1986).

3.1.6 Integration in time

Equations 3.21, 3.22, and 3.26 are evolved in time using a second-order Runge-Kutta-Fehlberg integrator (e.g. Benz 1984) with individual particle timesteps. This integration scheme allows for a maximum absolute change for any evolved quantities, which defines a maximum timestep given by

$$\delta t_{RK} = \sqrt{\frac{512\delta t_{old}\lambda}{|Q_{new} - Q_{old}|}} \tag{3.29}$$

(Bate et al., 1995). Here, λ is an arbitrary tolerance for the change of the quantity Q (e.g. $\vec{r}$, $\vec{v}$, h, or u) and δt_{old} is the previous timestep. On the other hand, the viscous form of the Courant condition (Monaghan, 1992) gives another maximum time step, defined as

$$\delta t_c = \frac{0.3h}{c_s + h|\nabla \cdot \mathbf{v}| + 1.2(\alpha c_s + \beta h|\nabla \cdot \mathbf{v}|)} \tag{3.30}$$

where c_s is the sound speed, $\vec{v}$ is the velocity of the particle, and α and β are the two artificial viscosity parameters (see Equation 3.19). The last term in the denominator is only included if $\nabla \cdot \vec{v} < 0$. A third condition on the time step, often called the force condition, can be written as

$$\delta t_F = 0.3\sqrt{\frac{h_i}{\mathbf{a}_i}} \tag{3.31}$$

(Bate, 1995) where $\mathbf{a}_i$ is the net acceleration on particle i. Basically, it prevents any particle from moving over large distances within one timestep. Particles are evolved with the smallest of these three timesteps. In addition, we use individual timesteps as a way of speeding up the code by evolving on small timesteps only the particles requiring smaller timesteps. All the timesteps are binned in multiple of 2 and particles are evolved starting with those with the smallest timestep until all the particles are synchronized on the largest timestep allowed. This is one of the major improvements that was made to the original code by Bate (1995).

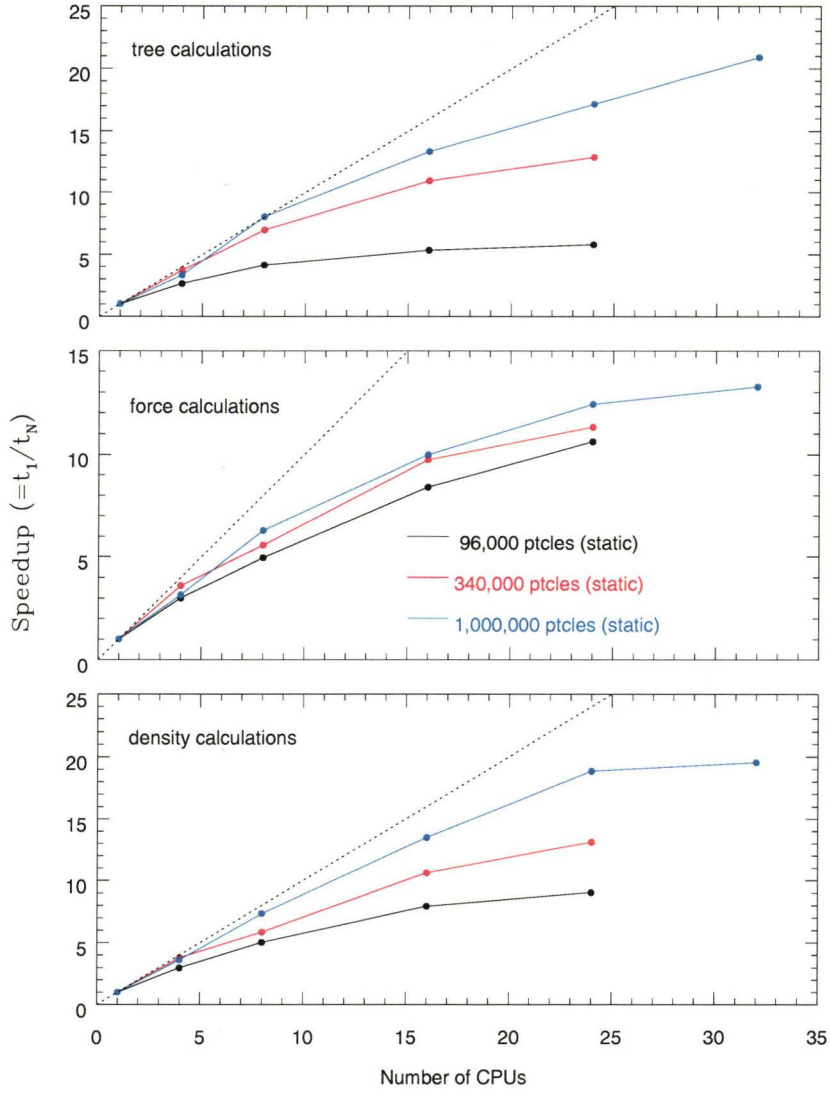

Figure 3.3 Scaling of our parallel SPH code with the number of CPUs for the relaxation of a single stars using different number of particles. t_1 and t_N are the total CPU times taken for serial and parallel runs, respectively. The dashed line represents the 1-to-1 ratio.

3.1.7 Parallelization

Our code was parallelized using OpenMP directives and Figure 3.3 shows the scaling of its performance (in terms of total CPU time) as a function of the

number of CPU used for different parts of the code for the simple relaxation of a fully modeled star (see §3.2.3). Typically, more than $\sim$ 80% of the CPU time is spent in the tree calculations, so the upper panel is representative of the overall performance of our code. We see that our code scales more or less linearly up to $\sim$ 24 CPUs for simulations of $\sim 10^6$ particles. For low-resolution runs (e.g. 96,000 particles or less), using too many CPUs results in overhead, where the time spent initializing and sharing the parallel sections of the code takes more time than the actual calculations. Most of the tests and large-scale simulations presented in this thesis were run on SHARCNET's shared memory systems `Silky` and `School` (www.SHARCNET.ca) under the normal member queue as well as under our 2009 dedicated resources awarded time.

3.2 Benchmark tests

Now that we have laid down the basic inner workings of our SPH code, we show in this section three standard hydrodynamical benchmark tests, namely the shock tube test, the adiabatic collapse, and the relaxation of a star, that demonstrate the capabilities and limitations of our codes to reproduce standard hydrodynamical benchmark tests. We hope to convince the reader that our code behaves physically, to a level of accuracy comparable to other SPH codes, and that it is well suited for the purposes of this thesis.

3.2.1 Shock tube

The shock tube test (Sod 1978) is a classical test that provides good insights into the treatment of artificial viscosity (for cases where self-gravity is not taken into account) because of the formation of shocks. A shock tube consists

of a tube with a high pressure and density fluid on one side and a lower pressure and density fluid on the other, separated by an imaginary diaphragm. Upon release of the diaphragm, we expect the formation of a shock and other characteristic features which can be compared with analytical expressions. Following Lombardi et al. (1999), the initial set up consists of a one-dimensional tube of length unity aligned with the x-axis and centered at $x = 0$ where particles are equally spaced along the tube. On the left side of the tube, density and pressure are set to $\rho_l = 1.0$ and $p_l = 1.0$, respectively, whereas we set $\rho_r = 0.25$ and $p_r = 0.12402$ on the right-hand side of the tube. Using an adiabatic EOS (Eq. 3.28) with a constant ratio of specific heats $\gamma = 5/3$, we get $u_l = 1.5$ and $u_r = 0.744$ on either sides of the tube. We use Monaghan's viscosity (see §3.1.3) with α=β=1.0 and η^2=10^{-2} and allow for the smoothing lengths to change in time according to equation 3.26. For this particular test, we use a total of 2500 equal-mass particles and keep the number of neighbours between 8 and 16 (mean number of neighbours being 12). Figure 3.4 shows the density, pressure, internal energy, and velocity (v_x) profiles for our 1D-tube after 0.10 time units. Our results are also compared with the analytical expressions (c.f. Rasio & Shapiro 1991) and show good agreement, comparable to what most other authors get (e.g. Hernquist & Katz 1989; Lombardi et al. 1999; Price 2004). The sharp jumps at $x \approx 0.07$ is most likely due to the jump in the initial conditions at the centre of the tube, and the shock, discontinuity, and rarefaction waves (from right to left) are clearly visible and well resolved by our code. Although this 1D test provides support that we are treating shocks and artificial viscosity adequately, it does not provide any insight into the correctness of our three-dimensional code.

We therefore also model a three-dimensional shock tube with similar

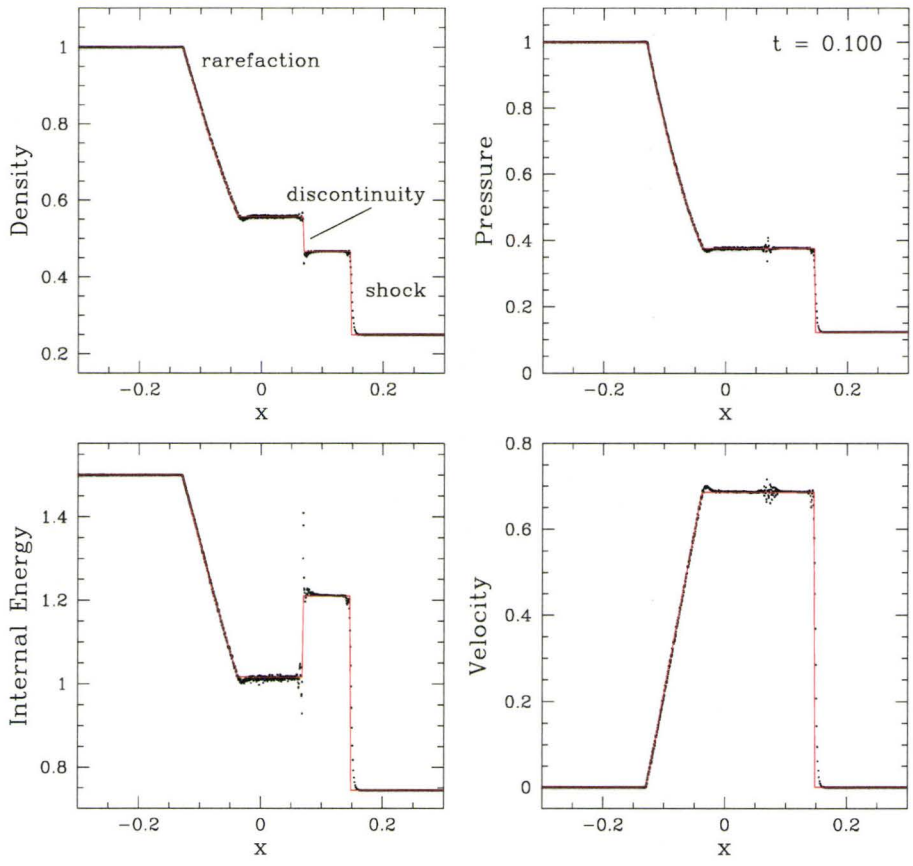

Figure 3.4 Results from our 1D shock tube calculations with 2500 particles and γ=5/3 compared with the analytical profiles (red lines). Our initial conditions give rise to some spurious motion at the discontinuity but the overall profiles are very well matched by the analytical profiles.

initial conditions to assess the validity of our full 3D code. In this case, we set up a rectangular box of particles with sides at $x = \pm 1$, $y = \pm 1/2$, and $z = \pm 1/2$ with particles distributed on a cubic lattice with only small random perturbations in the position of the particles (10% of the initial spacing between the particles). In addition, we use 6×10^5 equal-mass particles in order to get a good particle sampling in all three directions, along with a mean number of neighbours of ~ 50. We use Monaghan's viscosity (Equation 3.19) with $\alpha = 1.0$ and $\beta = 2.0$, identical to what we use in our simulations presented in

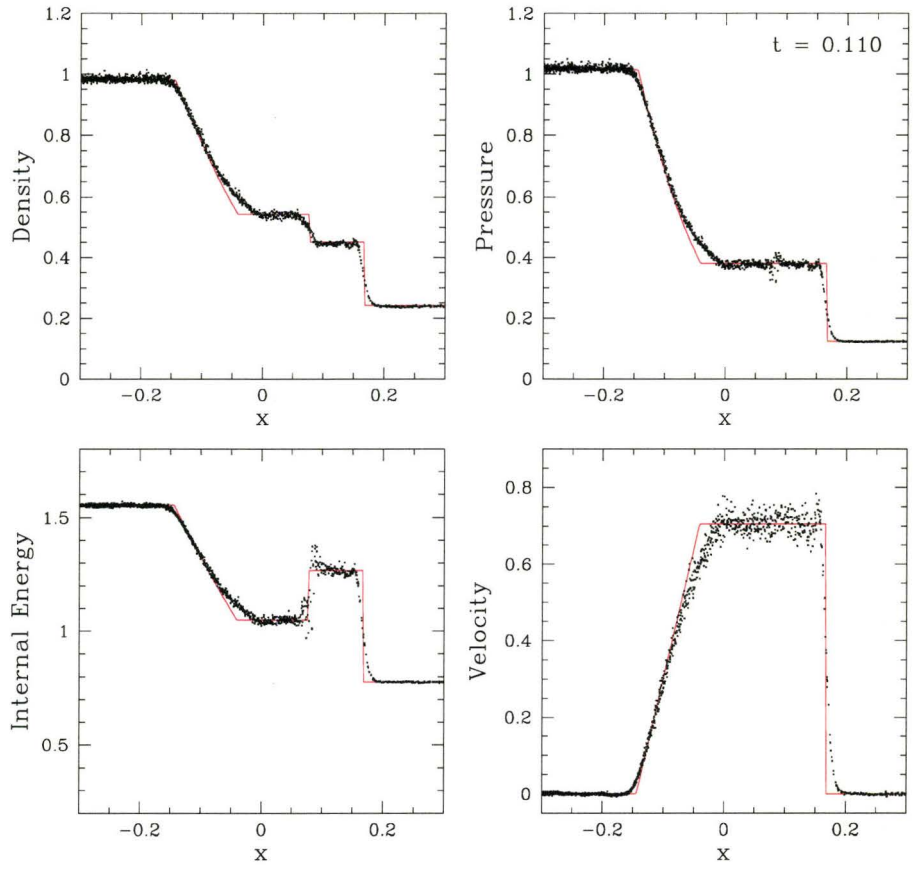

Figure 3.5 Results from our 3D shock tube calculations with 6×10^5 particles and γ=5/3 compared with the 1-D analytical profiles (red lines). Only particles close to the x-axis are shown.

Chapter 5. Here, the particles are initially distributed within their respective side of the box and then relaxed using boundary conditions (see §3.3), such that the particles reach an equilibrium configuration within their half of the tube. This ensure that the initial expansion of the gas, upon release, is along the $x-$axis, i.e. along the jump in the initial conditions. The results are shown in Figure 3.5 along with the one-dimensional analytical profiles. Only particles close (i.e. $\sim 2h$) to the x-axis are shown such that the boundary effects are negligible. The agreement with the analytical profiles is not as good as in

the 1D case but is qualitatively comparable to other authors' 3D shock tubes (e.g. Rasio & Shapiro 1991; Lombardi et al. 1999). The main characteristics of the shock tube, namely the shock, discontinuity, and rarefaction waves are clearly present, although not as sharply resolved as in the 1D case. We note that Wadsley et al. (2004), for example, get an excellent agreement between their 3D simulation and the analytical profiles, and we emphasize that better care in the preparation of the initial conditions would definitely improve the agreement between the simulated and analytical profiles.

3.2.2 Adiabatic collapse

As a further demonstration of the capabilities of the code, we show the results of the gravitational collapse of an adiabatic sphere. This test is not only useful for further validating the treatment of shocks but also for assessing the gravitational force implementation of our code. We use a similar initial set up as that of Hernquist & Katz (1989) with the exception that we use a cubic lattice with 6272 particles to start with, rather than a random distribution. The gas sphere, of mass M= 1 and radius R= 1, is initially isothermal with a thermal energy per unit mass per particle of 0.05 and a density profile $\propto 1/r$. We also conveniently set G= 1 so that the calculated quantities are dimensionless and match those of Hernquist & Katz (1989). We use the artificial viscosity of Monaghan with $\alpha = 1.0$ and $\beta = 2.0$ and a mean number of neighbours of $\sim$50. Such a set up leads to an initial collapse of the gas sphere until a shock forms at $t \approx 0.8$. Soon after, the pressure gradient becomes large enough to halt the collapse and the gas sphere starts expanding. The systems oscillates few a times and eventually reaches equilibrium. Figure 3.6 shows the den-

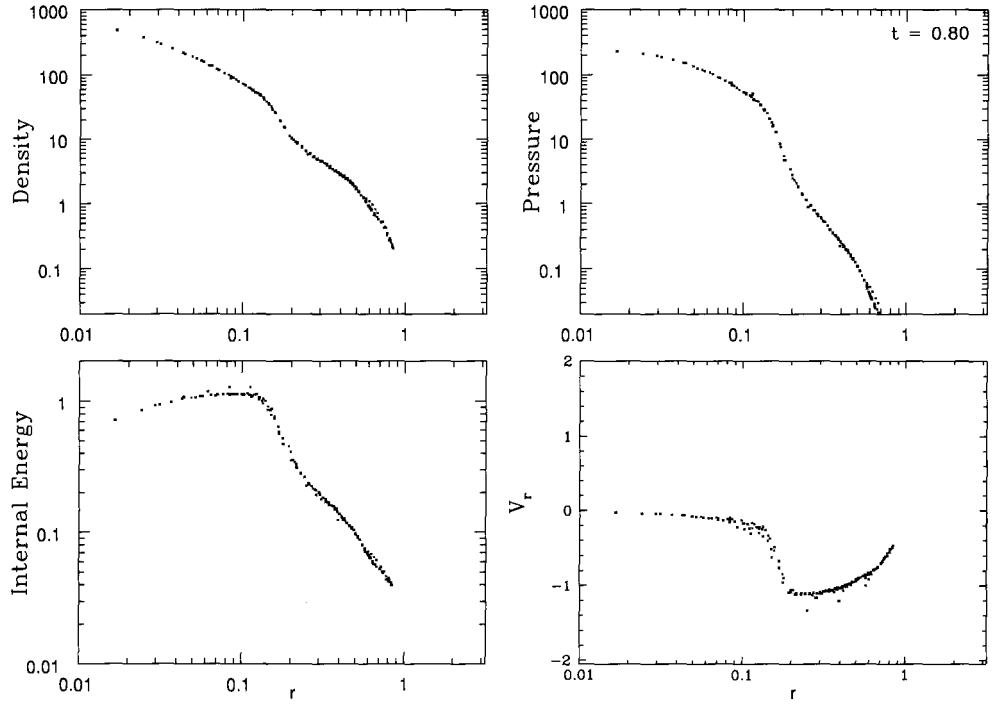

Figure 3.6 Density, pressure, internal energy, and radial velocity profiles at $t = 0.8$ (code units) of the adiabatic collapse of a gas sphere with $R = M = G = 1$ and $\gamma = 5/3$.

sity, pressure, internal energy, and radial velocity at t= 0.8 of the collapse. Although no analytical expressions exist to describe the evolution of such a collapse, our results quantitatively match those of other authors (Hernquist & Katz, 1989; Humble, 1999). We also show in Figure 3.7 the kinetic, thermal, potential, and total energies (summed over all the particles) as a function of time for the same adiabatic collapse simulation. The initial collapse as well as the first rebound are clearly visible as the gravitational energy first decreases and then climbs back up to its equilibrium value. The total energy is well conserved as it changes by no more than $\sim 0.6\%$ of its initial value over the whole duration of the simulation, with a maximum change of $\sim 1.5\%$ during the maximal compression phase ($0.8 \lesssim t \lesssim 1.2$). Moreover, the shapes and ab-

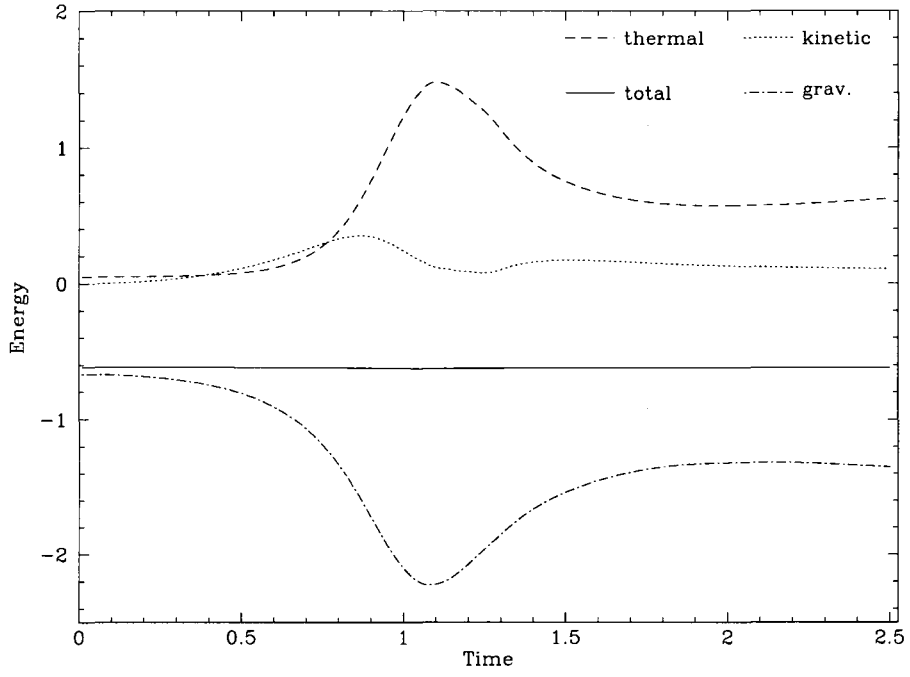

Figure 3.7 Energies (in code units) of the adiabatic collapse of an isothermal gas sphere. Total energy is conserved up to $\sim$ 0.6% over the duration of the simulation and changes by at most $\sim$ 1.5% during maximal compression ($0.8 \lesssim t \lesssim 1.2$).

solute values of the energies are in excellent agreement with those of Hernquist & Katz (1989).

3.2.3 Modeling and relaxation of stars

The relaxation of a star is a good test to measure the accuracy of both hydrodynamical and gravitational forces calculations as hydrostatic equilibrium requires a fine balance between these two forces. To realistically model SPH stars, we use theoretical density profiles as given by the Yale Rotation Evolution Code (YREC; Guenther et al. 1992). This codes can evolve stars of different masses and metallicities through the main sequence and up the red-giant

branch, thus allowing us to model many different types of stars. Although the physical EOS used in YREC is slightly different that the one used to model our stars (see §3.1.5), the purpose of the relaxation of our stars is to allow for the smoothing of these small differences in the EOS and the different profiles. Next, SPH particles are equally spaced on a hexagonal close-packed lattice extending out to the radius of the star, as specified by the YREC code. The theoretical density profile is then matched by iteratively assigning a mass and calculating the ensuing density (recall equation 3.8) for each SPH particle. We stop the iterations when the density profile of the SPH particles matches that given by YREC. Typically, particles at the centre of the stars are more massive than those located in the outer regions, by a factor depending on the steepness of the density profile (high-mass stars are more centrally condensed and hence have a steeper particle mass radial profile). As discussed by Lombardi et al. (1999), the initial hexagonal configuration that we use has the advantage of being stable to perturbations but also tends to arise naturally during the relaxation of particles. A description of how the hexagonal close-packed lattice configuration can be implemented is found in Lombardi et al. (2006). Once set up, stars are relaxed for a few dynamical times in order for the configuration to redistribute some of its excess thermal energy and settle down. A damping term proportional to each particle's velocity can also be added to the momentum equation during the relaxation in order to limit the oscillations and bring the star to equilibrium faster. Figure 3.8 shows a 0.8-$M_\odot$ main-sequence star relaxed for 20 dynamical times ($\tau_{dyn} = \sqrt{R^3/GM}$; here we use solar units, which yields $\tau_{dyn} \simeq 30$ min.) along with the density, internal energy, particle mass and smoothing length profiles. Panel *a* shows the particles located within two smoothing lengths of the $z = 0$. During the relaxation, the star readjusts

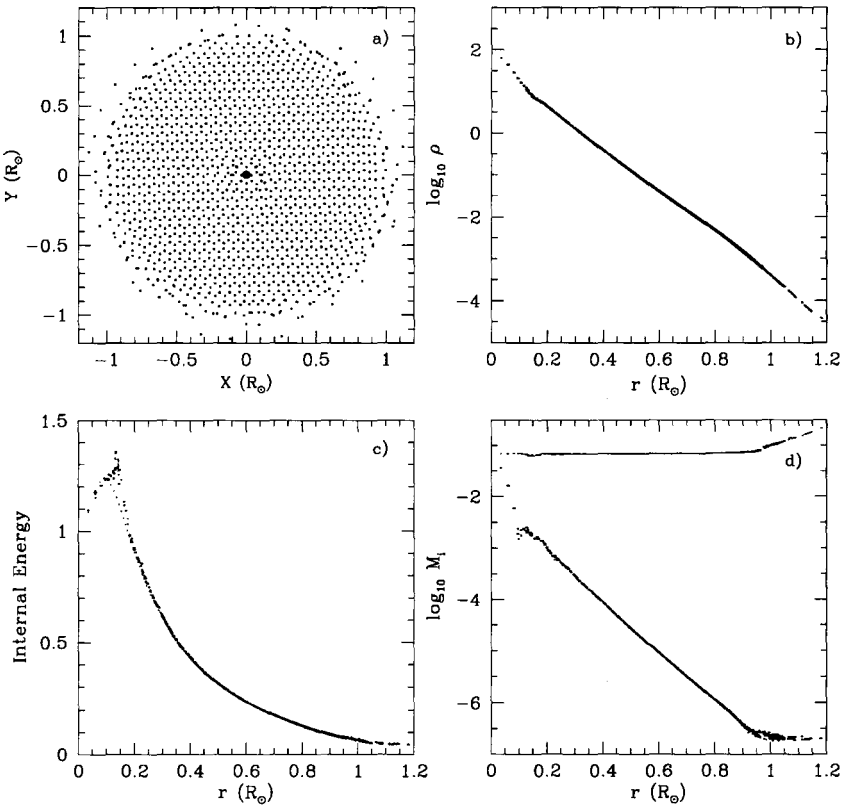

Figure 3.8 Relaxation of a 0.8-$M_\odot$ main-sequence star after 20 τ_{dyn} modeled with a total of 15952 particles. Particles within a few smoothing lengths of the $x-y$ plane are displayed in panel *a*). The initial hexagonal configuration can still be seen as well as a central point mass (red dot). The density (*b*) and internal energy (*c*) profiles are displayed in black and compared to their initial profiles, in red. Panel *d*) shows the particle mass (black) and the smoothing lengths (green) profiles as a function of radius at the end of the relaxation.

its structure slightly by oscillating and eventually reaches hydrostatic equilibrium after $\sim$10 τ_{dyn}. Interestingly, the final relaxed configuration still shows the hexagonal close-packed pattern of the initial set up, emphasizing that the initial configuration is already close to equilibrium. The density and internal energy profiles are also compared to their initial (theoretical) profiles, marked in red, and both match qualitatively well even after 20 τ_{dyn}. As discussed above, the range in masses for the SPH particles depends on the steepness of

the star's density profile. In this case, we see that the mass range almost five orders of magnitude. We see no problems in using particles of different masses here since, as the star reaches hydrostatic equilibrium, massive particles in the core do not interact with lighter particles at the surface. Likewise, we see that the smoothing lengths at the surface of the star increase slightly. This is due to a surface/boundary effect where the void of neighbours on one side of a particle is counterbalanced by an increase of the smoothing length so that it has enough neighbours (recall discussion of §3.1.4).

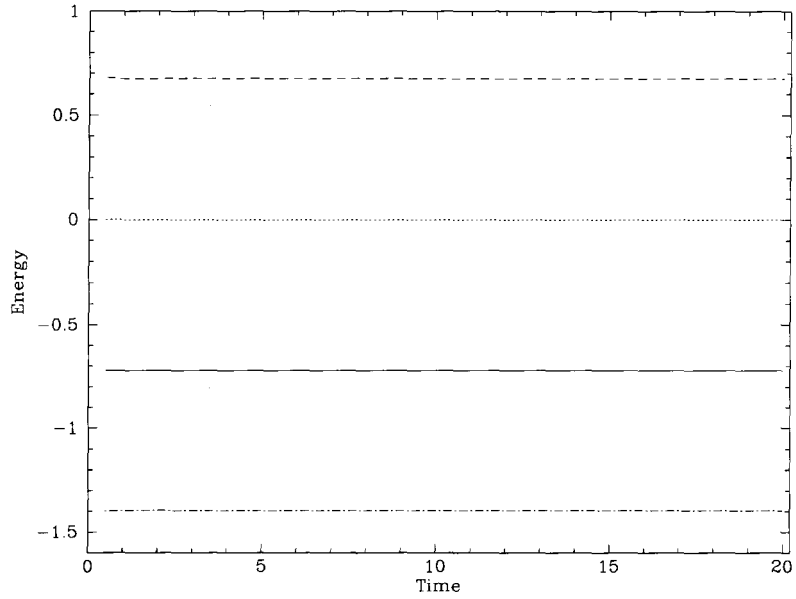

Figure 3.9 Energies during the relaxation of a 0.8-$M_\odot$ main-sequence star. Total and kinetic energies (solid and dotted lines, respectively) are very well conserved whereas gravitational (dash-dotted) and internal (dashed) energies oscillate slightly during the relaxation.

Finally, Figure 3.9 shows the different energies as a function of time for the relaxation of the same 0.8-$M_\odot$ star. The oscillations at the beginning of the relaxation can barely be seen in the gravitational and thermal energy curves (they vary by less than 1%), again emphasizing on the near-equilibrium

initial hexagonal configuration used to model the star. The total energy in the system is also conserved to a high accuracy (better than 0.01%) during the whole duration of the relaxation. Kinetic energy remains negligible for the whole duration of the relaxation as only the outermost and lightest particles undergo the oscillations seen during the relaxation.

3.2.3.1 Point masses

For cases where the density gets too large at the centre of the stars (e.g. massive stars or giant branch stars), our iterative method for determining the mass of particles partially fails at reproducing the density profile in the core. In such cases, we either need to increase the spatial resolution by using more particles or manually add mass by using so-called point masses. Sometimes, increasing the number of particles is not an option as it also increase the computational resources needed, and so we have to rely on point masses. Point masses interact with each other and with SPH particles only via the gravitational force. In our code, the latter is calculated directly via a direct `N`-body type summation. Moreover, our code uses the smallest of the particles's timesteps to evolve the point masses forward in time. Despite their name, point masses are also smoothed in space (using a smoothing length) to avoid diverging forces during close interactions. Typically, we give the point mass the same smoothing length as the initial star configuration. The relaxation of the 0.8-$M_{\odot}$ star shown in Figures 3.8a and 3.9 was done with a point mass at the centre of the star to correct for the cuspy density and particle mass profiles.

3.3 Improved boundary conditions

We now discuss the implementation of boundary conditions in SPH, focusing mainly on the application of such boundary condition to the hydrodynamical modeling of mass transfer in binary stars. In this context (and as briefly discussed in Chapter 1), boundary conditions can be used to isolate regions of interest in stars, hence reducing the total number of particles without decreasing the spatial resolution. Indeed, as discussed by Deupree & Karakas (2005), the inner parts of stars in close binaries generally remain unaffected by the presence of a companion, and only the structure of the outermost layers is modified by such close tidal interactions. This result prompted us to develop a new, innovative treatment of boundary conditions in SPH that allows the modeling of only the outermost parts of the stars without worrying about the inner regions. The advantages of using boundary conditions for the modeling of mass transfer in binary systems are that (1) CPU time is spent solely on particles actually taking part in the mass transfer or being affected by the companion and (2) it allows, for a given spatial resolution, to speed up the simulations as fewer particles are being used. Conversely, for the same amount of CPU time, this allows for the use of more particles, therefore enhancing the spatial and mass resolutions.

SPH codes calculate hydrodynamical quantities (e.g. density) by averaging over a sufficiently large number of neighbours. For particles located close to an edge or a boundary (e.g. the wall of a container), two things happen. First, since there are no particles on one side of the boundary, a large pressure gradient exists and the particles tend to be pushed outside of the domain of interest. Second, if the number of neighbours is kept fixed by requirements,

as it is the case in our code, then the smoothing length is overly increased until enough particles are enclosed by the particle's smoothed volume. This has the effects of decreasing the spatial resolution at the boundary and making the particle's density smaller than what it really should be. In some circumstances, this can be problematic and to avoid such complications, the implementation of boundary conditions is required.

Boundary conditions have usually been modeled in two different ways. The first of them was introduced by Monaghan (1994) (see also Monaghan 1997) who modeled boundary conditions with fixed particles exerting a purely repulsive force of the form of a Lennard-Jones potential. This particular potential, which was first applied to molecular dynamics, was successfully applied in SPH to model free-surface flows with special applications to breaking dams and wave makers. This technique, however, has not gained much attention as the number of particles needed to properly model the boundary can get rather large (see Monaghan 1997). On the other hand, boundary conditions have also been implemented using so-called *ghost* particles, first introduced by Takeda, Miyama, & Sekiya (1994). Ghost particles are just like SPH particles: they contribute to the density of SPH particles and provide a pressure gradient. This pressure gradient thus prevents SPH particles from approaching or penetrating the boundary. However, instead of evolving their position in time at every timestep, ghost particles are created dynamically every time an SPH particle gets within two smoothing lengths ($2h$) of the boundary. When this occurs, the position of each ghost is mirrored across the boundary from that of its SPH (parent) particle whereas the mass and density of the ghost are identical to its parent's. Thus, the need for ghosts (and a boundary) occurs only when a particle comes within reach of the boundary. The left panel of

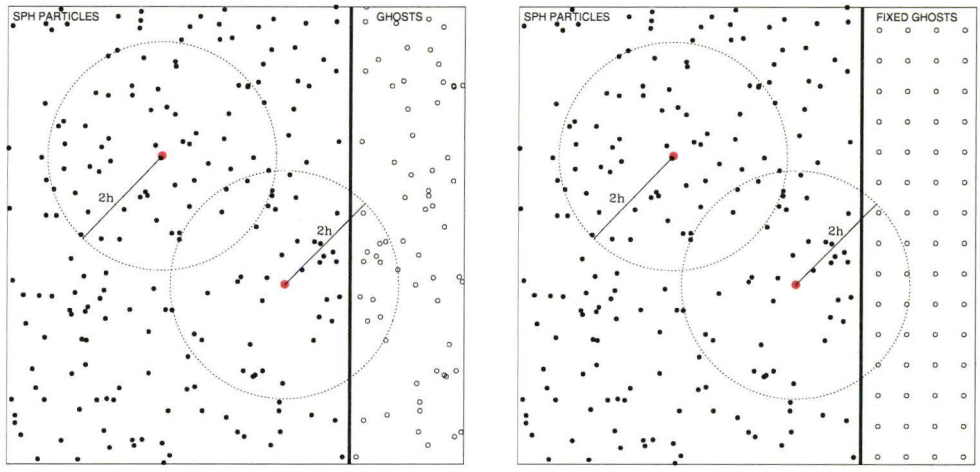

Figure 3.10 Illustrations showing how boundary conditions are implemented using mirrored (*left*) and fixed (*right*) ghosts. SPH and ghost particles are represented by solid and open dots, respectively, and the boundary is represented by the solid line. In panel *a*), the position of the ghosts mirror that of their parent SPH particle across the boundary whereas in panel *b*), the ghosts are fixed in space. The density calculation of SPH particles includes the contributions from *all* particles located within two smoothing lengths of them.

Figure 3.10 exemplifies the use of mirrored ghost particles into the calculation of the density of any SPH particles close enough to the boundary. Finally, free-slip (i.e. frictionless) and no-slip boundary conditions can be modeled by giving the ghosts a velocity parallel or opposite to their parent's, respectively, and including them in the viscosity contribution to the momentum and energy equation (Equations 3.21 and 3.22) of SPH particles.

3.3.1 Applications to stars

We have tested the boundary conditions discussed above on stars in hydrostatic equilibrium (see §3.2.3) and have realized that ghosts created dynamically lead to spurious motion close to the boundary and to the formation of a

small gap (of order h) in between the boundary and SPH particles. We think the reason for this behaviour comes from the fact that SPH particles located very close to the boundary can have very close ghost neighbours. The contribution from these close ghosts to the density and acceleration of the SPH particle is therefore overestimated and a gap forms in the radial distribution of particles. Moreover, since the mass of the ghosts is identical to that of their parent, the density profile at the boundary is flat, unlike that of a realistic model star, and the pressure gradient can be underestimated. For these reasons, we use a slightly different approach, based on the work of Morris, Fox, & Zhu (1997) and Cummins & Rudman (1999) on incompressible flows, for the modeling of boundary conditions. The approach of these authors differs from the mirrored ghost approach in that the ghosts are created once, at the beginning of the simulation, and their relative position remains fixed in time. Here, we further improve upon this technique in order to model the outer parts of self-gravitating stars (see Figure 3.10). Starting from our relaxed configurations, we identify any particles as ghosts if they are located within three smoothing lengths *inside* of the boundary, which, at this point, is arbitrarily determined. Particles located above the boundary are tagged as SPH particles, whereas the remaining ones are erased and replaced by a central point mass whose total mass accounts for both the particles removed and those tagged as ghosts. Figure 3.11 illustrates our boundary conditions for the case of a spherical star, where the initial, hexagonal configuration of the ghosts can be observed. Here, we use three smoothing lengths of ghosts as a first safety check in order to prevent SPH particles from penetrating the boundary. If this were to happen, then an SPH particle would still "see" enough particles in its neighbourhood. As a second safety check however, we enforce that no

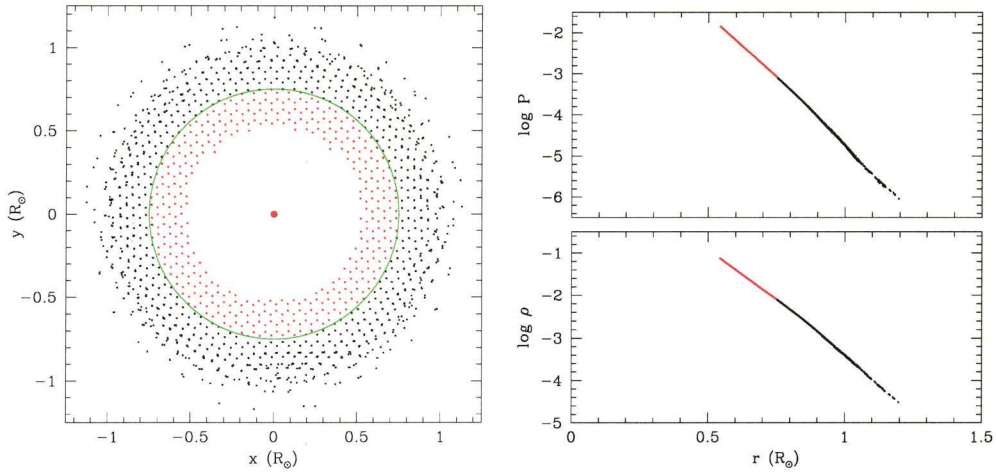

Figure 3.11 *Left*: Example of a star modeled with ghost particles (small red dots), SPH particles (black dots), which are found beyond the boundary (green line), and a central point mass (big red dot). *Right*: Density and pressure profiles of the ghosts (red) and SPH particles (black) showing the gradients at the boundary, as expected for realistic models of stars. This ensures that the ghosts provide the right pressure gradient onto the SPH particles located close to the boundary. In both panels, only the particles located within $2h$ of the equatorial plane are plotted.

particle goes further than one smoothing length inside the boundary by repositioning above the boundary any such particle, with its velocity changed to that of the ghosts. By using our initial configuration for the setup of ghosts, we ensure that the ghosts' position, internal energy, and mass are scaled to the right values and that the ensuing pressure gradient maintains the global hydrostatic equilibrium, as shown in the right panel of Figure 3.11. Moreover, the overall density and pressure profiles fall right on top of the theoretical profiles. As mentioned above, we include ghosts when calculating the artificial viscosity contributions. However, here, ghosts are not included in the gravitational force calculations as their total mass is replaced by the central point mass.

As mentioned, the position of the ghosts is not evolved. Rather, their

position is changed according to that of the central point mass and all the ghosts and the point mass move as one solid object. At each smallest timestep, the point mass is advanced, and the ghosts are advanced, by a simple translation, by the same amount. We further impose solid rotation onto the ghosts, with an assumed angular velocity, and move the ghosts accordingly at each timestep. We only model solid rotation, where all the ghost particles rotate at the same angular velocity, independent of the radial position of the particles. The ghosts' angular velocity is assumed fixed in time but, for cases where it might be expected to change (e.g. when modeling the tidal synchronization of binary stars), it can be adjusted continuously such that rotation period remains synchronized with the orbital period. In the latter case, we suggest that the angular velocity can be adjusted simply using Kepler's third law:

$$\omega^2 = \frac{G(M_1 + M_2)}{a^3} \tag{3.32}$$

where a is the separation between the centre of masses. Note however that we have not made use of this correction in the work presented in this thesis.

In order to conserve momentum, we also take into account the reaction force onto the ghosts and the point mass. Indeed, ghosts exert a pressure gradient force on the SPH particles and the reverse must also be true. Since the point mass and the ghosts move together, we impart this acceleration directly to the point mass according to the following relation:

$$\mathbf{a}_{pm}^{gh} = -\sum_i \frac{m_i}{m_{pm}} \mathbf{a}_i \tag{3.33}$$

where i represents the SPH particles interacting with the ghosts and a_i is

the hydrodynamical acceleration imparted to particle i from ghost j. This is Newton's third law applied to the ghosts and the SPH particles. This term is added to the usual gravitational acceleration of the point masses. Note also that at this point in our code, $\mathbf{a}_i$ has already been calculated so that this calculation requires no extra CPU time.

To demonstrate how our boundary conditions behave when both hydrodynamical and gravitational forces are taken into consideration, we relax a 0.8-$M_\odot$ star while giving it an angular velocity of 0.10 (code units). Once it reaches equilibrium, we remove the particles in the central regions and make use of our boundary conditions, i.e. we create ghosts and put a central point mass. We give the star, the ghosts and the central point mass the same translational velocity value as well as an angular velocity. Figure 3.12 shows the energies for this simulation including ghosts particles evolved for 70 τ_{dyn}. The slight decrease in gravitational and internal energies is due to rotation, which made the star expand slightly due to the outward acceleration. Given the angular velocity for this particular simulation ($\omega = 0.10$), the star complete nearly one full rotation over the duration of the simulation, and no signs of instability are observed in the density nor internal energy profiles. Overall, the total energy is well conserved again. These results suggest that the treatment of boundaries is adequate, at least for isolated stars in translation and rotation.

3.4 Summary

In this chapter, we presented our computational method, namely Smoothed Particle Hydrodynamics, and outlined its main equations and inner workings.

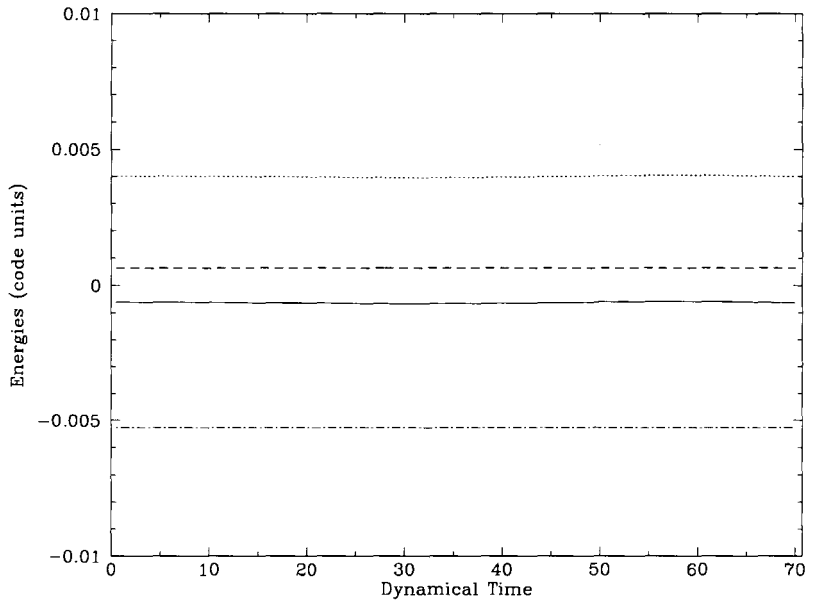

Figure 3.12 Different energies, in code units, as a function of dynamical time during the translation and rotation of a 0.8-$M_\odot$ main-sequence star modeled with ghost particles. Again, total and kinetic energies are the solid and dotted lines, respectively, whereas gravitational and internal energies are shows as dash-dotted and dashed lines, respectively.

We showed that our code can reproduce standard benchmark tests for the treatment of shocks (shock tube in 1D and 3D) and that it can handle hydrodynamics and self-gravity self-consistently in the case of adiabatic collapse and the relaxation of a main-sequence star. We also discussed previous implementations of boundary conditions and introduced an innovative way of dealing with them in the context of stellar hydrodynamics. In particular, using fixed ghost particles, we are able model only the outermost layers of stars while giving them arbitrary translational and rotation velocities. We also showed that the total energy is well conserved during simulations involving our boundary conditions. We hope to have convinced the reader that our code is *numerically* reliable and well suited for stellar hydrodynamics problems. We now

show, in Chapter 4, that our code is *physically* reliable and that it yields sensitive results when dealing with binary stars and close interactions such as mass transfer.

Chapter 4

Initial Conditions for Binary Mass Transfer Calculations

In this chapter, we discuss initial conditions for modeling binary stars with SPH. In particular, we develop a self-consistent technique for relaxing binary stars in non-inertial reference frames which allows us to model and evolve circular binaries over many orbits. Our results also show that our code can accurately follow (and maintain) two stars on relatively tight orbit for many tens of the stars' dynamical time. We also show that our novel way of modeling stars with ghost particles yields similar results and that it can appropriately be applied to the modeling of mass transfer in binary systems. We discuss the limitations of our relaxation procedure as well as our new approach, with an emphasis on the conditions under which they each perform best. Finally, we introduce the different binary systems that we will be using for our full-scale simulations of eccentric binaries, with an emphasis on the different theoretical expectations based on the different masses of the stars involved.

4.1 Binary star relaxation

As discussed in §3.2.3, stars must be relaxed prior to being used in any kind of simulations. Although the initial SPH particle density and thermal energy profiles are iteratively adjusted to match the theoretical profiles obtained from a stellar evolution code, which are by construction in hydrostatic equilibrium, the initial setup are not quite in equilibrium. Therefore, we must allow our stars to self-consistently readjust their structure so that they reach hydrostatic equilibrium by evolving them for a few dynamical times. This is even more true for binary systems since the tidal effects from the companion star is not taken into account when calculating the theoretical profiles. Therefore, great care must be taken when preparing binary systems for SPH simulations.

There are two physical ingredients that have to be accounted for when preparing binary stars for SPH simulations. First, the companion's tidal pull, which gives the typical elongated, tear-drop shapes to close binary stars is easily taken into account by putting the two stars in the same relaxation simulations. Second, stellar rotation, which tends to slightly reshape stars (the faster the rotation, the more important this effect), must be accounted for since binary stars do rotate. Indeed, binary stars will only reach hydrostatic equilibrium when their (spin) rotation is synchronized with the orbital angular velocity such that the same faces of the two stars always face each other. In a reference frame that is centered at the centre of mass of the binary and that rotates with the same angular velocity as the stars along their orbit, the two stars should be at rest. However, in such a rotating frame, the two stars are at rest only if a centrifugal term is added to the acceleration of the SPH particles. Therefore, by assuming that our stars should be at rest in a rotating reference

frame, we can find the right conditions under which the stars will relax and reach equilibrium. The procedure we use is similar to that outlined in Rosswog et al. (2004) and Gaburov et al. (2010).

As just mentioned, the two orbiting stars should be at rest in a rotating reference frame. The mutual gravitational pull between the two stars only tends to bring them closer to each other, so we must introduce a fictional centrifugal acceleration[1] that will counterbalance the inward gravitational pull. The centrifugal acceleration is defined as

$$\mathbf{a}_c = \Omega^2 \mathbf{r} \tag{4.1}$$

where Ω is the angular velocity of the rotating frame and r is the distance from the axis of rotation. Since we assume an orbital separation when initializing our binary systems (i.e. we know $\mathbf{r}$), it is therefore possible to find an angular velocity Ω that cancels the stars' net gravitational accelerations. Note that we do not account for the Coriolis force[2] since the system is assumed to be at rest in the rotating frame (actually, it takes a few dynamical timescales to achieve), in which case the Coriolis force is (or becomes) negligible. At each timestep, we determine the angular velocity necessary such that the net (i.e. hydrodynamical + gravitational) acceleration of the centre of mass of each star is zero. The net acceleration of the centre of mass of star i is calculated

[1]The centrifugal force is not an actual force, but rather a pseudo-force that originates only from the fact that we are using a rotating (or a non-inertial, in more general terms) reference frame.

[2]The Coriolis force is another fictional force that arises when an object is moving in a rotating reference frame. It is written as $\mathbf{a}_{Cor} = -2\boldsymbol{\Omega} \times \mathbf{v}$, where $\mathbf{v}$ is the velocity of the object under consideration.

in the following way:

$$\mathbf{a}^i_{\rm cm} = \frac{\sum m_j(\mathbf{a}^{\rm hyd}_j + \mathbf{a}^{\rm grav}_j)}{M_i} \tag{4.2}$$

where M_i, $\mathbf{a}_{hyd}$ and $\mathbf{a}_{grav}$ are, respectively, the total mass and the hydrodynamical and gravitational accelerations of star i. The sum is taken over all particles of star i. Given that the centre of mass of star i is at

$$\mathbf{R}^i_{\rm CM} = \frac{\sum m_j \mathbf{r}_j}{M_i}, \tag{4.3}$$

we get the following condition for the angular velocity:

$$\Omega^2_i = \frac{\sum m_j(a^{\rm hyd}_j + a^{\rm grav}_j)}{\sum m_j r_j}. \tag{4.4}$$

where r_j is the distance of the particle to the axis of rotation of the binary. We find the angular velocity for both stars and then take the average value, which we use to calculate the necessary centrifugal acceleration to be added to the total acceleration of each SPH particle. Lastly, to ensure that the orbital separation is kept constant during the whole duration of the relaxation, we reposition the star's centre of mass to the original separation by a simple translation after each (largest) timestep.

Using this method to relax a binary, the angular velocity typically oscillates only slightly at the start of the relaxation and eventually settles down near its final equilibrium value. As for the case of single stars, we add a damping term proportional to the particle's velocity ($\eta\mathbf{v}$, where we set $\eta \simeq 1$ such that oscillations are quickly damped) to the total acceleration of the particles such that the relaxation is faster. Typically, binary stars being relaxed wobble and oscillate until an equilibrium configuration is reached. In general,

we perform the relaxation procedure for $\sim$30 τ_{dyn}, which usually takes longer than a typical SPH simulation since it requires looping over all the particles for calculating the acceleration and position of the centres of mass. Figure 4.1 shows the different energies, in code units, as a function of time for the relaxation of a $0.60 + 0.60$ $M_{\odot}$ binary with an orbital separation of 3.25 $R_{\odot}$. Overall, the total energy is very well conserved and only slight oscillations in the gravitational and thermal energies can be seen. The greatest change in any kind of energy occurs during the first few timesteps where all the energies are calculated by considering the contribution from two stars, hence the initial abrupt change in all the energies. Also, we see that the kinetic energy reaches a minimum around which it more or less remains constant for the remainder of the relaxation, suggesting that the star has reached equilibrium. An example of such a detached, relaxed binary is shown in Figure 4.2.

As a final note, we note that it is possible to obtain semi-detached or contact configurations by simply decreasing the orbital separation during the binary relaxation. Following the work of Rosswog et al. (2004) (see also Renvoizé et al. 2002), the orbital separation can be updated using a rate of the following form:

$$\dot{a} = \frac{(a - A_{RL})}{\eta \tau_{dyn}}, \tag{4.5}$$

where A_{RL} is the separation at which the primary fills it Roche lobe, τ_{dyn} is the largest dynamical timescale and η is a constant whose value is arbitrarily set to $\sim 20 - 30$. However, this should be used with care as mass transfer can be initiated during the relaxation. We have not extensively tested this approach and more work remains to be done on this aspect of the relaxation procedure to ensure equilibrium semi-detached or contact configurations.

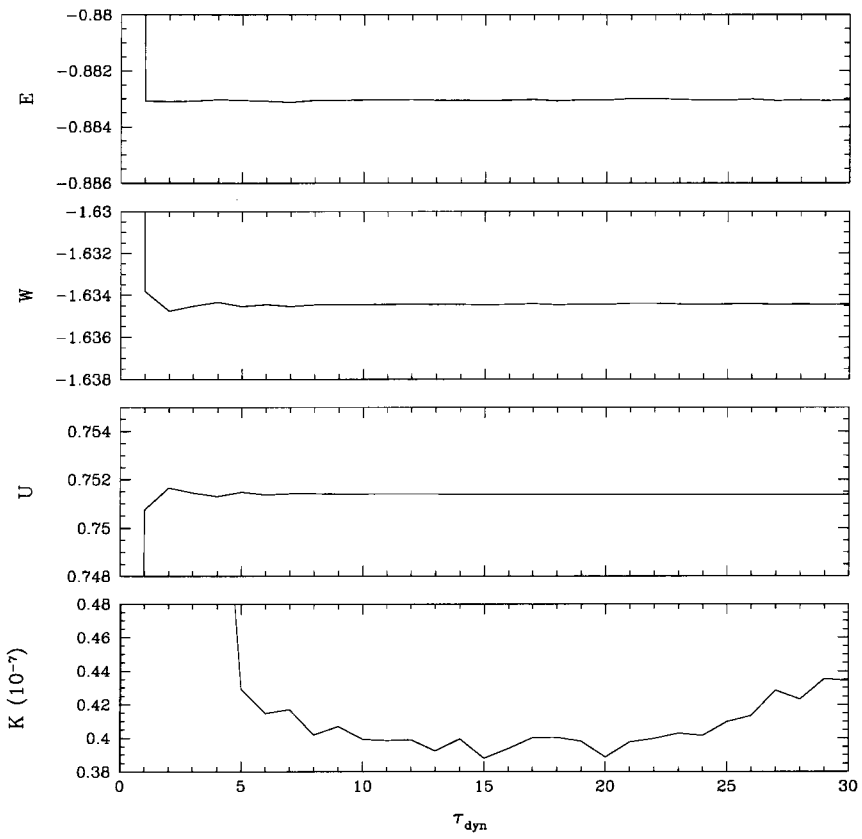

Figure 4.1 Energies (in code units) during the relaxation of a $0.60 + 0.60$ $M_{\odot}$ modeled with 200,000 particles.

4.2 Circular orbits

Once relaxed, the stars are put in an inertial reference frame in which they orbit around each other. For circular orbits, the velocities are simply converted by using the angular velocity obtained from the binary relaxation procedure and the distance from the respective centre of mass. As an example of our relaxation procedure, we have evolved different wide *circular* binaries, consistently relaxed using the approach presented in §4.1, for a small number of orbits. In particular, we are interested in the binary separation as we do not expect it to change significantly since (1) the stars are well within their Roche

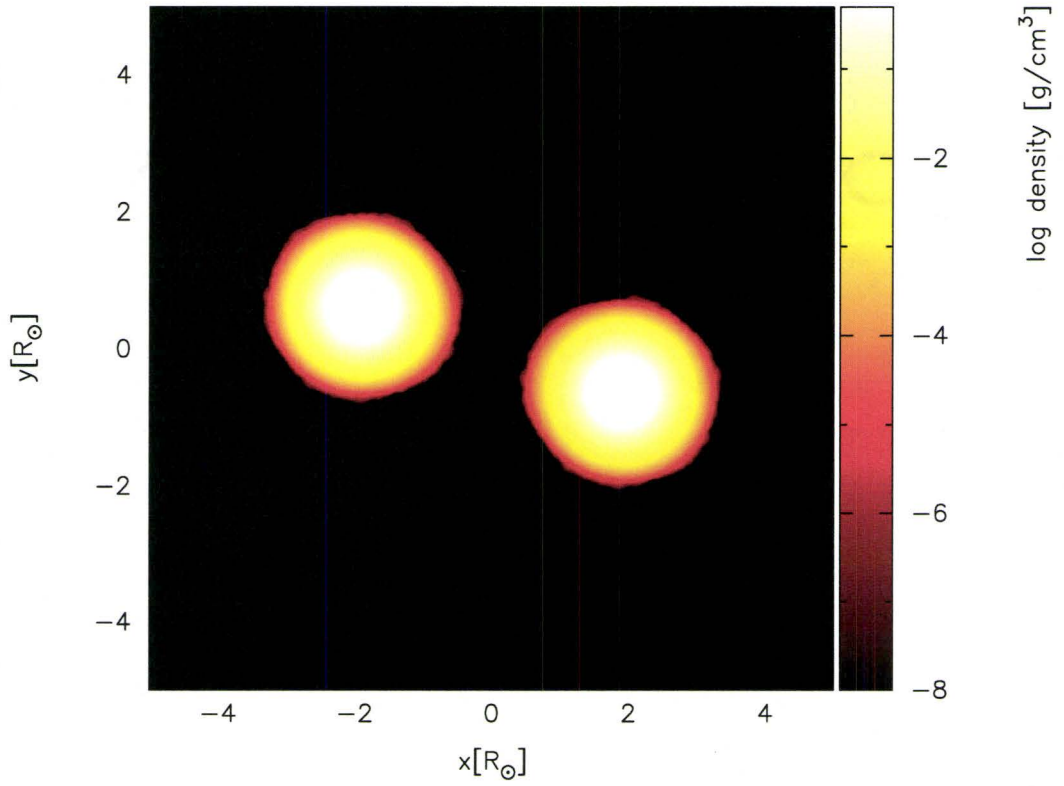

Figure 4.2 Logarithm of density in the orbital plane for a detached relaxed binary with two stars of masses 0.80 $M_\odot$.

lobe and no mass transfer of any kind is expected and (2) the stars are, *a priori*, assumed to be in equilibrium for such a configuration. This is an important assessment of the physicality and numerical integration capabilities of our hydrodynamical code as, for simulations of mass transfer, it is imperative that any changes in orbital separation be driven by the mass transfer itself and not the initial conditions and/or numerical errors inherent to our method. Therefore, we assess the capabilities of our relaxation technique by evolving detached binaries where the separation should remain constant.

First, we present the results of the evolution of a $0.60 + 0.60$ $M_\odot$ binary ($q = 1$) with each star fully modeled with $\sim 105,000$ SPH particles (i.e.

without a boundary) with an initial separation of 3.25 $R_\odot$ for six orbits. In this case, our relaxation procedure yields an angular velocity of $\Omega = 0.1875$ which is the same as the Keplerian value. Given the relatively large initial separation, this is not surprising. Figure 4.3 shows the different energies of the system as well as the orbital separation between the centres of mass of the stars, all normalized to their initial value, as a function of time. It is quite impressive how well the total energy is conserved as well as all the other forms of energy. Moreover, the orbital separation remains constant, to better than $\sim 0.25\%$, for over six orbits. The slight (anti-symmetric) variations observed in the orbital separation and the kinetic energy are an indication that either the system is on an eccentric orbit and that the initial velocity is slightly off or the stars have not quite reached hydrostatic equilibrium. However, at this level, we attest that our code can properly (and physically) evolve two stars in orbits around each, given that they were initially relaxed.

Next, we show lower-resolution simulations of similar binary systems modeled both with and without boundary conditions. Now that we know that our binary relaxation procedure is adequate and allows us to model circular binaries for a number of orbits, we wish (1) to assess the effects of our boundary conditions on such simulations and (2) the benefits that we gain by modeling stars with boundary conditions. Figures 4.4 and 4.5 show the normalized energies and orbital separation for two $0.80 + 0.80$ $M_\odot$ binaries both modeled with an initial orbital separation of 4 $R_\odot$ but different number of particles. The red and black lines correspond to the systems modeled with and without boundary conditions, respectively, and we see that introducing the boundary conditions smoothes the oscillations observed for the fully modeled binaries. This smoothing of the oscillations can be explained by the fact that we have

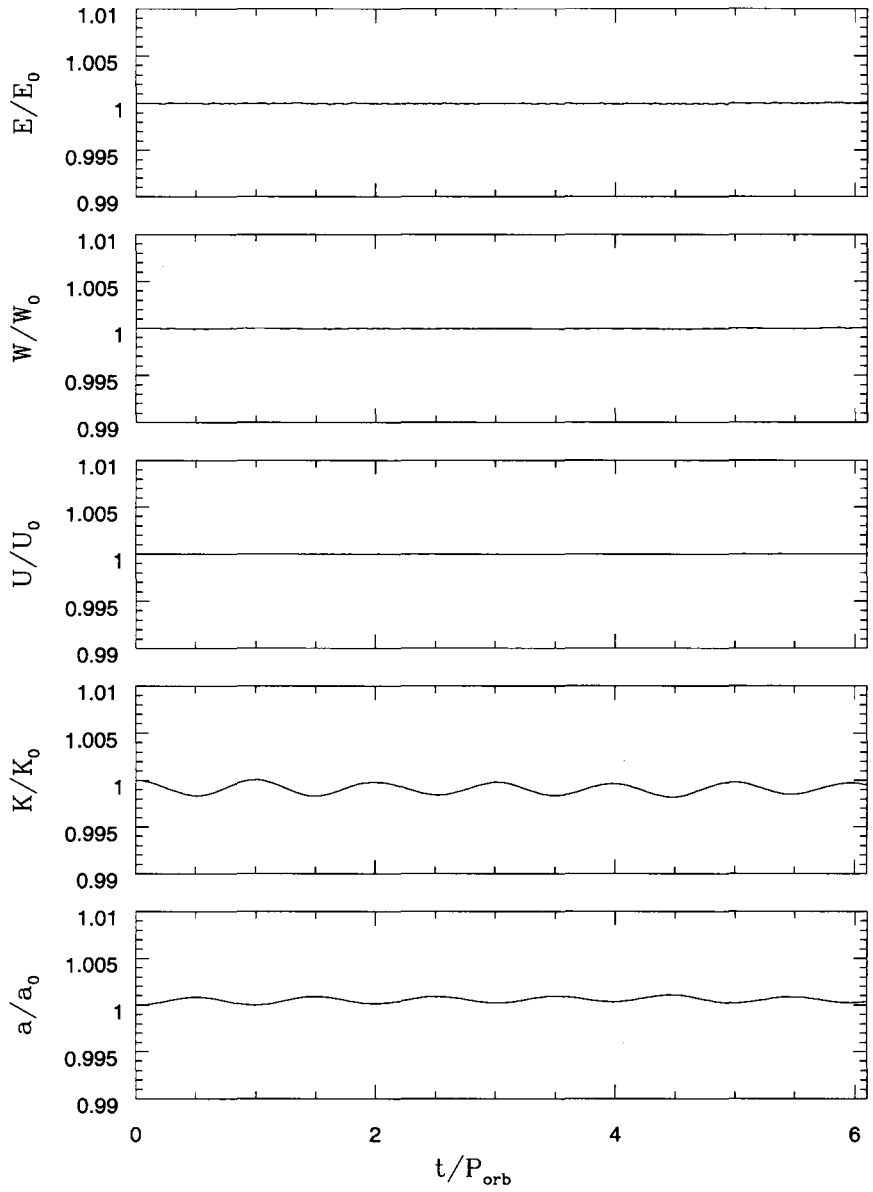

Figure 4.3 Normalized energies and orbital separation as a function of time for a 0.60+0.60 $M_\odot$ binary modeled with ~200,000 particles initially relaxed using the method of §4.1 with fixed orbital separation.

replaced the inner SPH particles in each star by a central point mass, therefore changing the way the gravitational acceleration is calculated for most of the mass of the stars and also limiting the amount of oscillating mass. Indeed,

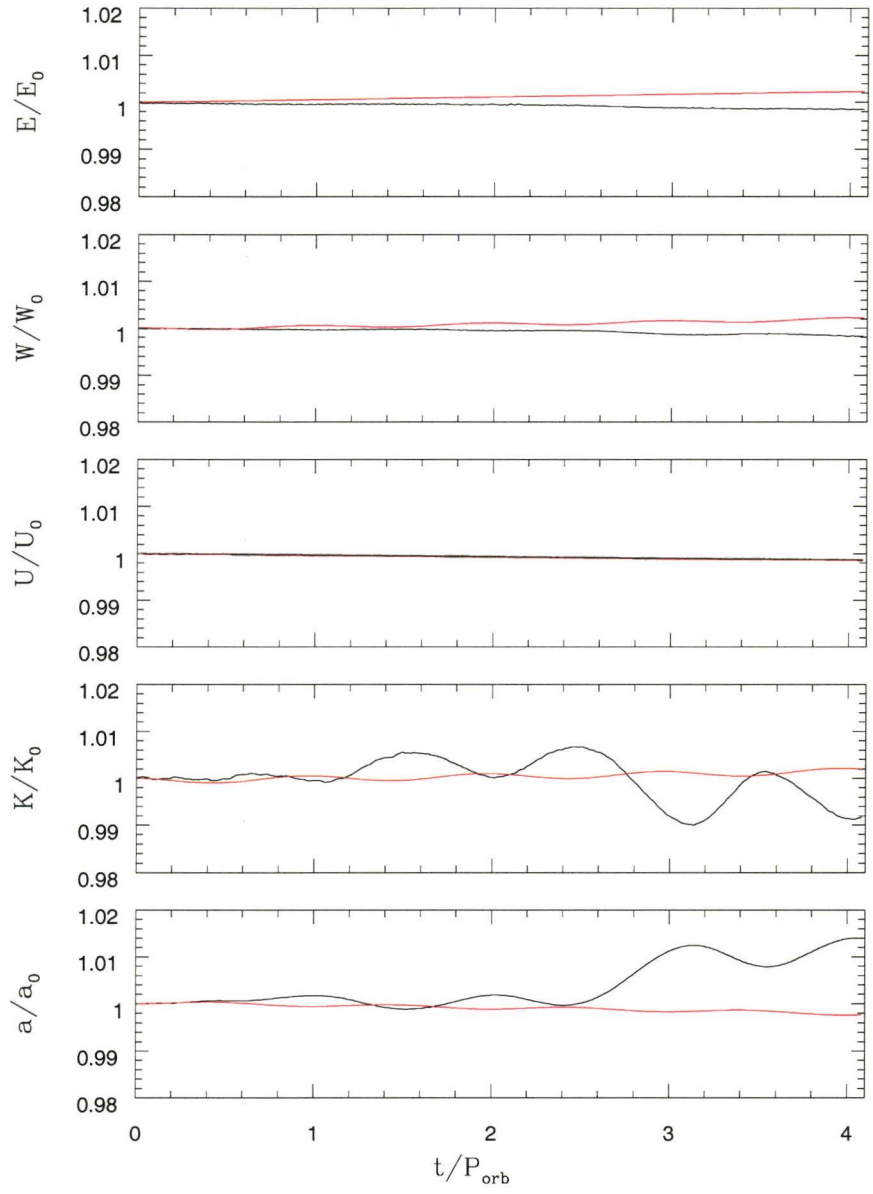

Figure 4.4 Comparison of the normalized energies and orbital separation as a function of time for a 0.80+0.80 $M_\odot$ binary modeled with (red) and without (black) boundary conditions. The former contains $\sim 20,000$ particles whereas the latter contains $\sim 40,000$ particles.

when using point masses, the gravitational acceleration on them is calculated with direct summations over all the particles rather than by a tree. For the fully modeled stars, once the oscillations get too large, then the structure of the

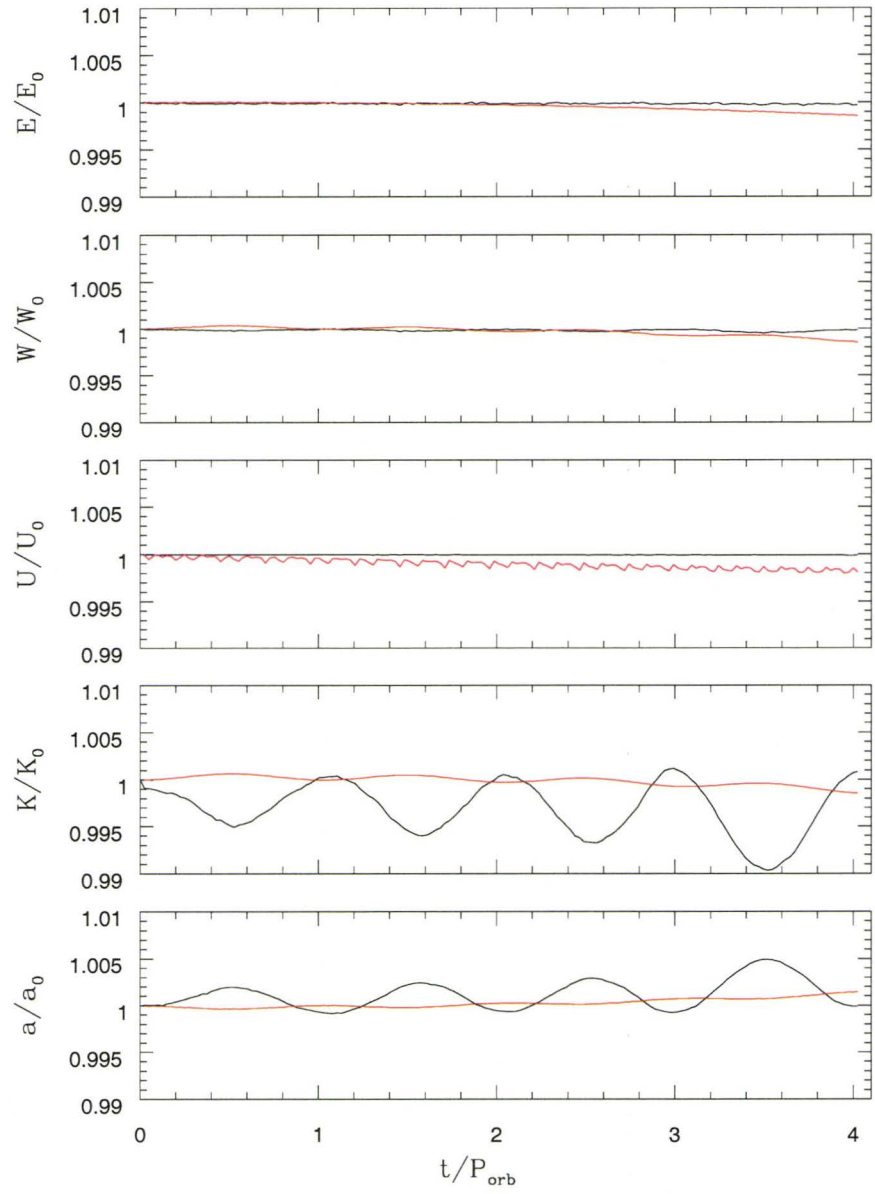

Figure 4.5 Comparison of the normalized energies and orbital separation as a function of time for a 0.80+0.80 $M_{\odot}$ binary modeled with (red) and without (black) boundary conditions. The former contains $\sim 240,000$ particles whereas the latter contains $\sim 150,000$ particles.

stars has to readjust (slightly) and it is difficult to reach an equilibrium state. In all cases, on the other hand, the total energy is fairly well conserved over the whole duration of the simulations and changes by no more than $\sim 0.25\%$. We

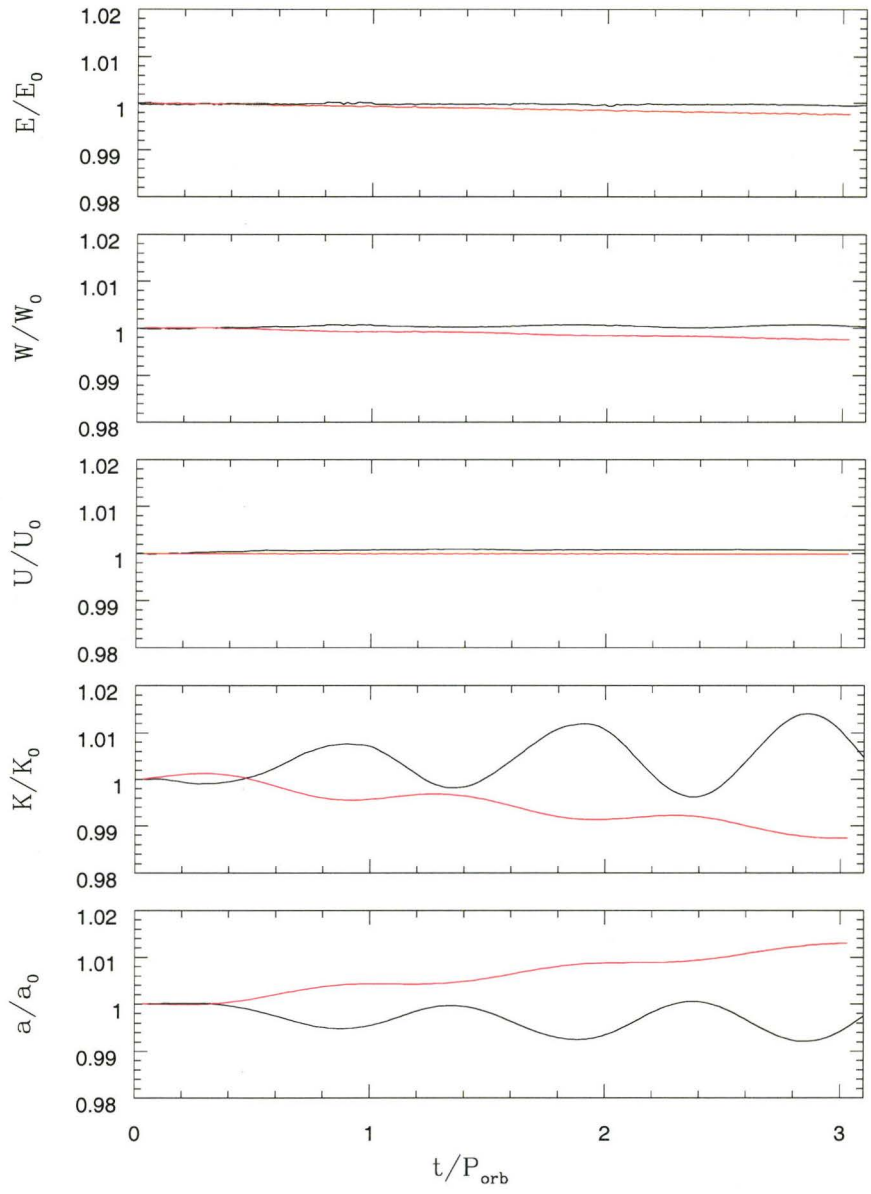

Figure 4.6 Comparison of the normalized energies and orbital separation as a function of time for a 0.80+0.48 $M_{\odot}$ binary modeled with (red) and without (black) boundary conditions and $\sim 20,000$ particles.

also notice that using more particles, i.e. having a better spatial resolution, increases the quality of the evolution of the orbits. Indeed, over the same number of orbits, the orbital separation in our high-resolution simulation (Fig.

4.5) varies by less than 0.5%, unlike the low-resolution one (Fig. 4.4) which has changed by $\sim 2\%$ after four orbits. We note that differences in the initial conditions (i.e. stars not quite in hydrostatic equilibrium) could explain such a difference in the orbital evolution. Similarly, Figure 4.6 show the evolution of a $0.80 + 0.48$ $M_{\odot}$ binary system for over three orbits and a relatively low number of particles. Note that only the primary is modeled with the use of our boundary conditions for reasons that are discussed in §4.3. Again, the orbital separation remains fairly close to its initial value, to within 2% at the end of four orbits, although it seems to be slowly increasing towards the end of the simulation. The total energy is again fairly well conserved (better than 0.5%) and only the kinetic energy oscillates significantly, which is the result of the orbital separation changing over time, as can be seen by the mirrored behaviours of the kinetic energy and the orbital separation.

Although using our boundary conditions introduces the need to directly calculate the contribution from all the particles to the point masses' gravitational acceleration, we find that the evolution of binary systems can be faster by up to $\sim$ 50% when modeled with boundary conditions. The amount of CPU time saved by using our boundary conditions of course depends on the location of the boundary, which changes the number of both SPH and ghost particles. Finally, when comparing our results of circular orbits with those of other authors, we find that our binary relaxation procedure yields quantitatively comparable orbital behaviours. Indeed, the results of Benz et al. (1990) show oscillations of $\sim 1-2\%$ in the orbital separation over three orbits whereas the simulations from Dan, Rosswog, & Brüggen (2009) of two unequal-mass binaries showed a constant orbital separation for many tens of orbits with an accuracy of $\sim 1\%$. Motl, Tohline, & Frank (2002) and D'Souza et al. (2006),

using a specifically designed grid-based hydrodynamics code, both could maintain equal- and unequal-mass binaries on circular orbits with an accurary of $\sim 0.25\%$ over five orbits.

4.3 Numerical limitations

We have tested our binary relaxation procedure extensively for both equal- and unequal-mass binaries and the latter have always shown to be more difficult to relax properly and evolve on a circular orbit for many orbits. The reason for this difference in behaviours arises from the fact that the equal-mass systems that we have modeled are perfectly symmetric, i.e. the two stars are exact replicas of each other. In such cases, the gravitational acceleration calculations should be equal and opposite and the two stars are evolved with the same timesteps. For the case of unequal-mass binaries, symmetry is broken in the force calculation and we have to deal with particles of different masses in the two stars having different timesteps. Therefore, care must be taken as the two stars might be evolved on different timesteps, thus rendering the relaxation less certain.

Our technique for modeling only the outermost layers of stars using boundary conditions works particularly well for stars of equal mass. In addition, we note that our technique works well for stars that are centrally condensed, where most of the mass in contained within a small fraction of the star's radius. This is generally the case for stars with masses $\gtrsim 0.8$ $M_{\odot}$, but also depends on the evolutionary phase of the modeled star as evolved stars become more centrally condensed. We have not extensively tested the dependance of our boundary conditions on the type of stars modeled, but one of

the reason for such a behaviour is that when the amount of mass beyond the boundary is significant (i.e. $\gtrsim 5 - 10\%$ of the total mass of star), the point mass feels a non-negligible gravitational pull from these SPH particles, which, because of the back-reaction force that we include (see §3.3), tends to make the orbit less stable. Therefore, we suggest that using our new boundary conditions with centrally condensed stars will in general yield better agreement with fully modeled stars. Moreover, in such instances, replacing the core of the stars by a massive point mass is also more representative.

4.4 Setting up the binaries

We now describe the binary systems that will be used in Chapter 5 to study mass transfer in eccentric binaries. We also briefly discuss some of theoretical expectations, as derived in Chapter 2, applicable to each of these systems.

The stars modeled in this thesis are all relaxed separately first, and then relaxed in a rotating reference frame using the binary relaxation procedure presented in §4.1. Typically, the relaxation procedure takes $\sim 2 - 3$ weeks on `SHARCNET`'s shared memory system `SILKY` with $16 - 20$ CPUs for simulations containing $800,000$ particles. In all cases, the more massive star is expected to overflow its Roche lobe at some point along its orbit and the initial orbital separation is chosen such that overflow does not occur at apastron but rather close to periastron. Once the relaxation is over, we use our new technique described in Chapter 3 and replace the core of each star with ghost particles and central point masses to model the boundary. Ghosts and SPH particles are given an angular velocity, as determined from our binary relaxation procedure, and the binaries are evolved in an inertial reference frame in which the stars

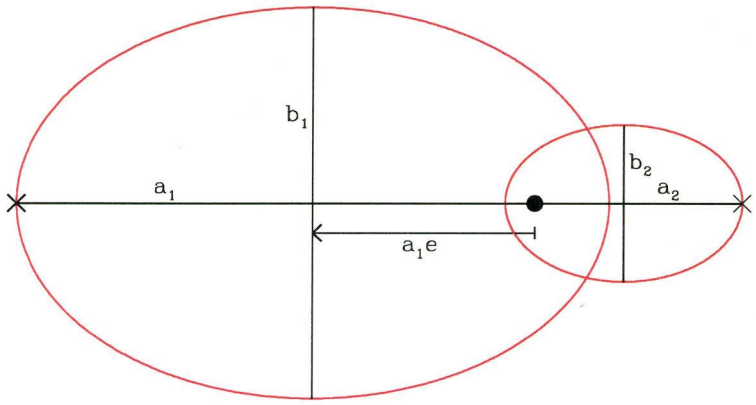

Figure 4.7 Ellipses of eccentricity $e = 0.5$ showing the semi-major and semi-minor axes. From this simple geometry and the use of conservation of energy along the orbit, it is possible to get the initial orbital velocity at apastron for our starting models (see text).

are moving around each other. For eccentric orbits, there exists no reference frame in which the stars are at rest, and therefore the procedure outlined in §4.1 cannot be applied. However, we can relax the stars with our binary relaxation procedure if we further assume that the stars are synchronized at apastron, and start their orbit from there. This is similar to the relaxation procedure of Church et al. (2009). We determine the initial velocities for our eccentric binaries by recognizing that, at apastron, the semi-major axis is related to the initial separation between the two stars (see Fig. 4.7):

$$a = \frac{r_{ap}}{(1+e)} = \frac{|\vec{r_2} - \vec{r_1}|_{ap}}{(1+e)} \tag{4.6}$$

where $\vec{r_1}$ and $\vec{r_2}$ are the respective position vectors of stars 1 and 2 with respect to the origin, and e is the eccentricity. The relative velocity at apastron is given

by

$$v_{ap} \equiv |\vec{v_2} - \vec{v_1}|_{ap} = \sqrt{\frac{G(M_1 + M_2)}{a}\left(\frac{1-e}{1+e}\right)} \tag{4.7}$$

By setting the centre of mass at the origin, we also get the following relations between the relative positions and velocities of the stars:

$$m_1\vec{r_1} = -m_2\vec{r_2} \qquad m_1\vec{v_1} = -m_2\vec{v_2}, \tag{4.8}$$

from which, when combined with equation 4.7, we can get the velocities of the stars at apastron:

$$v_{1_{ap}} = \frac{M_2}{M_1 + M_2} v_{ap} \tag{4.9}$$

$$v_{2_{ap}} = -\frac{M_1}{M_1 + M_2} v_{ap}, \tag{4.10}$$

where v_{ap} was defined in Equation 4.7. Finally, we note that the orbital plane lies along the $X-Y$ axes whereas the orbital and rotation spins point towards the negative Z direction (i.e. counterclockwise rotation). In all of our simulations, the ghosts' angular velocity remains fixed to its initial value, which is consistent with the fact that eccentric binaries are asynchronous and the (spin) angular velocity barely changes over a few orbits. This approximation for a constant angular velocity is consistent with the findings of Church et al. (2009) who did not observe any changes in the spin angular velocity in their simulations of mass transfer in cataclysmic variables.

4.4.1 0.80 + 0.48 $M_\odot$ binary

The first binary system we model contains low-mass main-sequence stars with masses of 0.80 and 0.48 $M_\odot$ both evolved for 13.5 gigayears, i.e. the age of

the Galaxy, which is also representative of some of the oldest stars in globular clusters. For this binary, the larger star, whose outermost layers are mostly convective, is losing mass and while its radius is expected to expand, its Roche lobe is expected to decrease (until the mass ratio q_1 becomes smaller than $\sim$0.784; see §2.2). The orbital separation, on the other hand, is also expected to decrease, at least until the mass ratio is reversed. Therefore, mass transfer should be self-sustained in this system since the mass-losing star increasingly overfills its Roche lobe, and the ultimate fate of such a system is most likely coalescence. We chose such a set up to demonstrate how our technique deals with relatively large mass transfer rates and assess its limitations. Moreover, such low-mass stars are actually among the high-mass end of the actual stellar population in globular clusters as the turn-off mass is around 0.8 $M_\odot$. It is thus interesting to study if (and how) episodes of mass transfer in such systems can rejuvenate a star and significantly increase its main-sequence lifetime, thus possibly forming a blue straggler.

The initial separation of this binary system, at apastron, is set to 4 $R_\odot$ such that the stars do not overflow their Roche lobe at apastron. The ghost particle boundary is set at 0.8 $R_\odot$ for the 0.8-$M_\odot$ star and 0.35 $R_\odot$ for the 0.48-$M_\odot$ star, both corresponding to $\sim$ 75% of the stars' radii. At these radii, most of the mass of the stars is encompassed by the boundary while still leaving enough particles to interact with the companion. The total number of particles is $\sim 600,000$ and the mass of SPH particles in each star is $\sim 4 \times 10^{-3}$ $M_\odot$ and $\sim 3 \times 10^{-2}$ $M_\odot$ for the 0.8- and 0.48-$M_\odot$ stars, respectively. Figure 4.8 shows the initial density, internal energy and particle mass radial profiles. The difference in SPH particle mass is mostly due to the fact that the density profile of the 0.48-$M_\odot$ star is much flatter than the the 0.80-$M_\odot$ star.

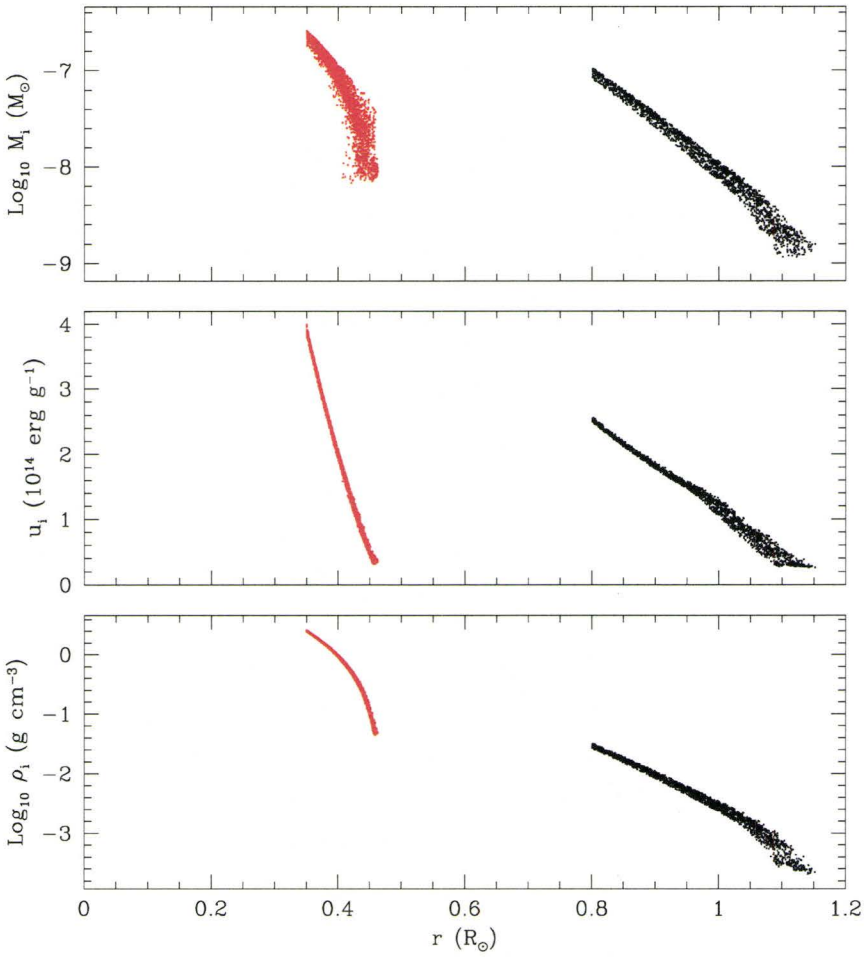

Figure 4.8 Density, internal energy, and mass radial profiles for the $0.80 + 0.48$ $M_\odot$ binary at the beginning of the simulation. The black dots are for the 0.8-$M_\odot$ star whereas the red dots are for the 0.48-$M_\odot$ star. As can be seen from the slightly scattered density and internal energy profiles, only the less dense, more massive star suffers from tidal forces.

Although the particle masses and internal energy at the surface are similar for both stars, the density contrast is substantial and this should prove difficult for any infalling material to penetrate into the secondary's envelope. We will discuss the accretion history of our simulations in §5.4. Table 4.1 lists the orbital parameters of the simulations performed along with some preliminary results. We modeled various eccentricities with the same initial (apastron)

Table 4.1. Parameter space explored along with preliminary results for the 0.80+0.48 $M_\odot$ binary

Model #	r_{ap} ($R_\odot$)	e	a ($R_\odot$)	P (τ_{dyn})	r_{peri} ($R_\odot$)	# orbits	Mass transfer	Notes
1	4	0.10	3.63	38.4	3.27	1.0	N	—
2	4	0.20	3.33	33.7	2.66	1.0	Y	1
3	4	0.25	3.20	31.8	2.40	5.0	Y	—
4	4	0.30	3.07	29.9	2.15	5.0	Y	—
5	4	0.35	2.96	28.3	1.92	0.5	Y	2

Note. — *1*: only a few particles transferred (see §5.7). *2*: mass transfer rate too large for the boundary to handle; particles penetrate boundary (see §5.7).

separations, which allows us to assess, among other things, the behaviour of our boundary conditions under increasingly large mass transfer rates.

4.4.2 1.50 + 1.40 $M_\odot$ binary

Second, we model more massive main-sequence stars with masses of 1.50 and 1.40 $M_\odot$ that are are mostly radiative and therefore are expected to shrink upon mass transfer. In this case, the two stars are 1.5 Gyrs old so that the more massive star is on the verge of leaving the main sequence. Again, since the donor is the more massive star, the Roche lobe is expected to decrease initially as well as the separation (until the mass ratio is reversed). In the circular orbit case, these responses of the stars and orbit would regulate the mass transfer process and lead to a stable situation. However, the theoretical expectations may differ as mass transfer is only episodic in eccentric binaries. We initially start the stars at a separation of 6 $R_\odot$, which places them well

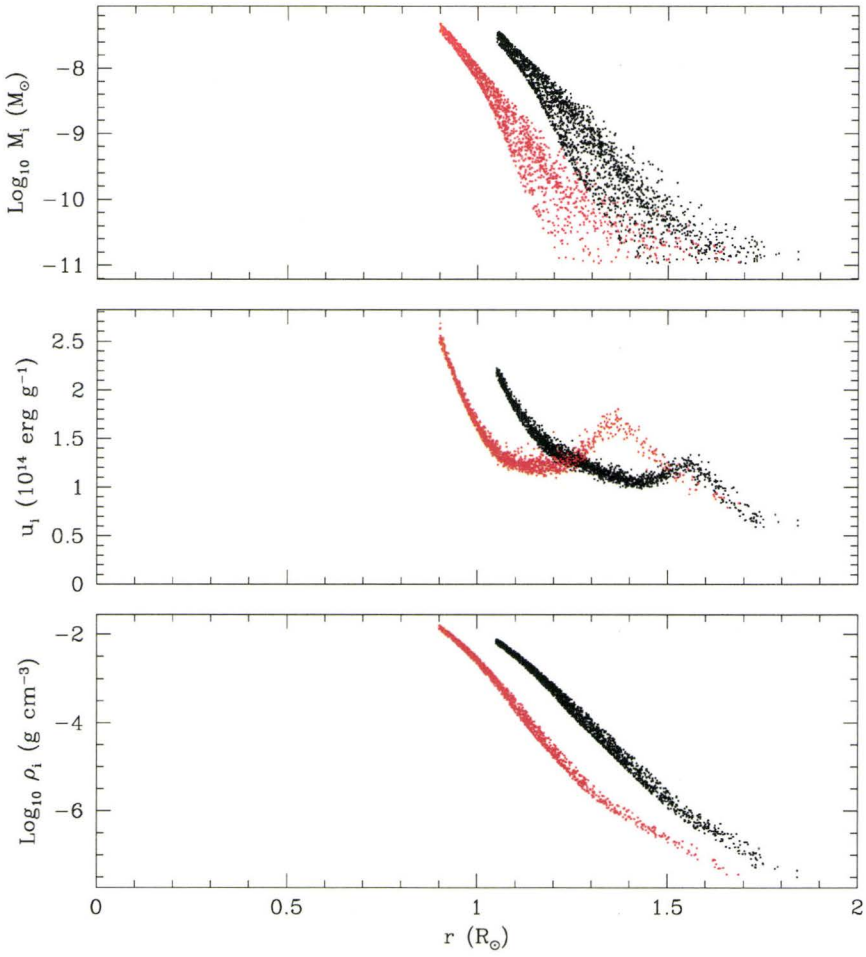

Figure 4.9 Density, internal energy, and mass radial profiles for the $1.50 + 1.40$ $M_\odot$ binary at the beginning of the simulation. The black dots are for the 1.50-$M_\odot$ star whereas the red dots are for the 1.40-$M_\odot$ star.

within their respective Roche lobes. The location of the boundaries is chosen, again, roughly around 75% of the total radius of the stars, corresponding to a radius of 1.05 and 0.90 $R_\odot$ for the primary and the secondary, respectively. The total number of particles is $\sim 440,000$ and, consequently, the total mass in SPH particles in the primary amounts to $\sim 1.16 \times 10^{-3}$ $M_\odot$ whereas the secondary contains $\sim 1.65 \times 10^{-3}$ $M_\odot$ of SPH particles. The remainder of the mass is contained in the central point masses. The small amount of mass

Table 4.2. Parameter space explored along with preliminary results for the $1.50 + 1.40$ $M_\odot$ binary

Model #	r_{ap} ($R_\odot$)	e	a ($R_\odot$)	P (τ_{dyn})	r_{peri} ($R_\odot$)	# orbits	Mass Transfer	Notes
6	6	0.15	5.22	44.0	4.43	4.00	Y	—
7	6	0.20	5.00	41.2	4.00	5.00	Y	—
8	6	0.25	4.80	38.8	3.60	6.00	Y	—
9	6	0.30	4.62	36.6	3.23	3.00	Y	1

Note. — *1*: mass transfer too large for the boundary to handle; particles penetrate boundary (see §5.7).

contained in our stars implies that our mass transfer simulations will not model the mass ratio reversal and should hardly see any changes in orbital separation.

We show in Figure 4.9 the density, internal energy, and particle mass profiles of the two components of this system. Unlike with the $0.80 + 0.48$ $M_\odot$ system, the density, internal energy, and particle mass profiles of both stars are very similar. We therefore expect the envelope of the secondary to interact somewhat more with the infalling material and maybe provide some kind of feedback into the system. Moreover, the particle masses of each star span the same range, unlike with the $0.80 + 0.48$ $M_\odot$, and this is arguably numerically more stable. Indeed, having particles with different masses (sometimes by many orders of magnitude) can lead to spurious motion and can be unwanted (see, e.g., Lombardi et al. 1999). Note, however, that we do not observe any spurious motion in our low-mass binary simulations, so this spurious motion effect might not be as important as noted by previous authors, at least in the

context of dynamical mass transfer. Table 4.2 lists the parameters for all the simulations that we have run with this system along with some preliminary results.

4.5 Summary

In this chapter, we presented our binary relaxation procedure and demonstrated its performances both on stars fully modeled with SPH particles and on stars modeled with our new boundary conditions. Our results showed that our code can evolve circular binaries to better than $\sim 2\%$ in orbital separation for many orbits. In particular, our method works especially well for equal-mass binaries. Also, we showed that the total energy is well conserved over many orbits. We finally discussed the limitations of our relaxation procedure and introduced the binary models that will be used in Chapter 5 for our full-scale mass transfer simulations.

Chapter 5

Episodic Mass Transfer in Eccentric Binaries

In this chapter, we apply our new technique presented in Chapters 3 and 4 to eccentric binaries. We showed that our new method is well suited for the modeling of mass transfer in binary systems and we now apply it to the binary systems discussed in Chapter 4 using various eccentricities, with the aim of getting a better understanding mass transfer in eccentric binary systems. Although the parameter space is large and that we explore only parts of it, we focus on getting a better idea of how eccentric binaries evolve upon episodic mass transfer. More particularly, we are interested in the mass transfer rates involved in such interactions, which could help calibrate stellar population synthesis and N-body codes that include and evolve eccentric binaries. Our new approach also allows us to follow the accretion process and investigate how much matter is actually (and more physically) accreted onto the secondary, which could provide a better understanding of conservation of mass in interacting eccentric binaries. But first, we discuss the overall behaviours observed

in our two sets of simulations.

5.1 0.80 $M_\odot$ + 0.48 $M_\odot$

As discussed in Chapter 4, the low-mass binary is interesting from the point of view that the mass transfer rate should, in theory, be self-enhanced and that the secondary is much denser than the primary. To demonstrate the general trends observed in our successful simulations, we use our own visualization tool and show, in Figures 5.1 and 5.2, the logarithm of the density for Model 3 ($e = 0.25$) in the XY- and XZ planes, respectively. Each image is 12 $R_\odot$ by 12 $R_\odot$ and the density scale ranges from 10^{-10} g cm^{-1} (dark) to 1 g cm^{-1} (white). In Figure 5.1, only particles located within two smoothing lengths of the orbital plane (i.e. $z = 0$) are plotted. Note that ghosts do not contribute to the density as calculated by our image processing program either, hence the slightly lower densities at the boundaries. In Figure 5.2, only particles located within two smoothing lengths of the line joining the two point masses are plotted. In other words, we are seeing the systems as if we were rotating with it such that we would always be perpendicular to the line joining the centres of mass. The 0.8-$M_\odot$ star is the largest of the two stars and the density contrast between the two stars is obvious from these plots. The point masses are represented by solid blue dots at the centre of each star. Interestingly, we can already note that mass transfer occurs only periodically, close to periastron, and that it shuts off when the stars are further apart. Moreover, we see that the secondary is retaining some of the transferred mass, forming some kind of envelope, whereas the primary does not seem to be affected strongly from losing mass. The density of the accreted material around the secondary is

much lower than that of the secondary's surface layer and this may have some implications for the long-term accretion of this material (discussed further in § 5.4). Some mass is also lost from the secondary's far side through the L_2 point whereas no (or very little) mass is lost through the primary's far side through the L_3 point. Such a mass loss is not surprising as the potential well of the secondary is shallower than that of the primary, even though asynchronism can bring these two Lagrangian points close to the same level, as discussed in Chapter 2. From Figure 5.2, we also observe the envelope surrounding the secondary, suggestive of a shell rather than a disk.

Figures 5.3 and 5.4 show, on the other hand, the thermal energy for the same system and for the same dynamical times as Figures 5.1 and 5.2. Unlike the density profiles, the internal energy profiles of these two stars are much more alike. Interestingly, the material surrounding the secondary is hotter than the secondary's surface (the cooler, redder ring around the secondary is actually its own surface layer). Thus, the secondary does not seem to be affected by the accreted material, at least on a dynamical timescale. Moreover, we see that the mass transfer stream in between the two stars is actually cooler than the surrounding material. This is more obvious in the XZ-plane view of Figure 5.4. This is due to the fact that the material in the mass transfer stream is expanding at the expense of its own thermal energy. Eventually, however, this material gets heated up as can be seen in the lower left panel where the mass transfer has (temporarily) shut off and the secondary is surrounded by an almost uniform envelope. The whole system eventually becomes engulfed in a relatively warm but low-density envelope that extends for many solar radii. It can be noted that the interior of the primary seems to contain some very low internal energy material, although no particles are ob-

served within the boundary. This is due to the contribution of a few particles close to the surface with relatively large smoothing lengths that reach inside the boundary. This is more obvious in the XZ-plane view of the system. No such thing is observed for the secondary however.

Finally, we show in Figures 5.5 and 5.6 the different energies and total angular momentum, respectively, normalized to their initial value, as a function of time for the same system (i.e. Model 3). From these Figures, we see that the total energy is fairly well conserved during the whole duration of the simulation. It varies by at most $\sim 3\%$ and seems to do so periodically. The eccentricity of this system is obvious from the shape of the curve of the kinetic energy as it peaks at periastron, halfway through the orbital period, and decreases almost back to its initial value. The different values of the extrema of the kinetic energy suggest that the orbital separation is changing. Similar behaviours are observed for all the models over their whole duration. As for the gravitational energy, it varies in the same fashion as the kinetic energy, whereas the thermal energy stays constant to within less than 0.5% over the whole duration of the simulation. Similarly, the total angular momentum also varies around its initial value, by no more than 2.5% over the whole duration of the simulation. We use the binary's centre of mass as the rotation axis when calculating the total angular momentum of the system and all of the angular momentum is, as expected, in the z-direction, i.e. perpendicular to the orbital plane. The angular momentum in the other directions is at least four orders of magnitude smaller and remains proportionally small for the whole duration of the simulations. We think the small variations in the total angular momentum observed in our simulations are most likely due to the angular velocity of the ghosts being artificially maintained at a fixed value.

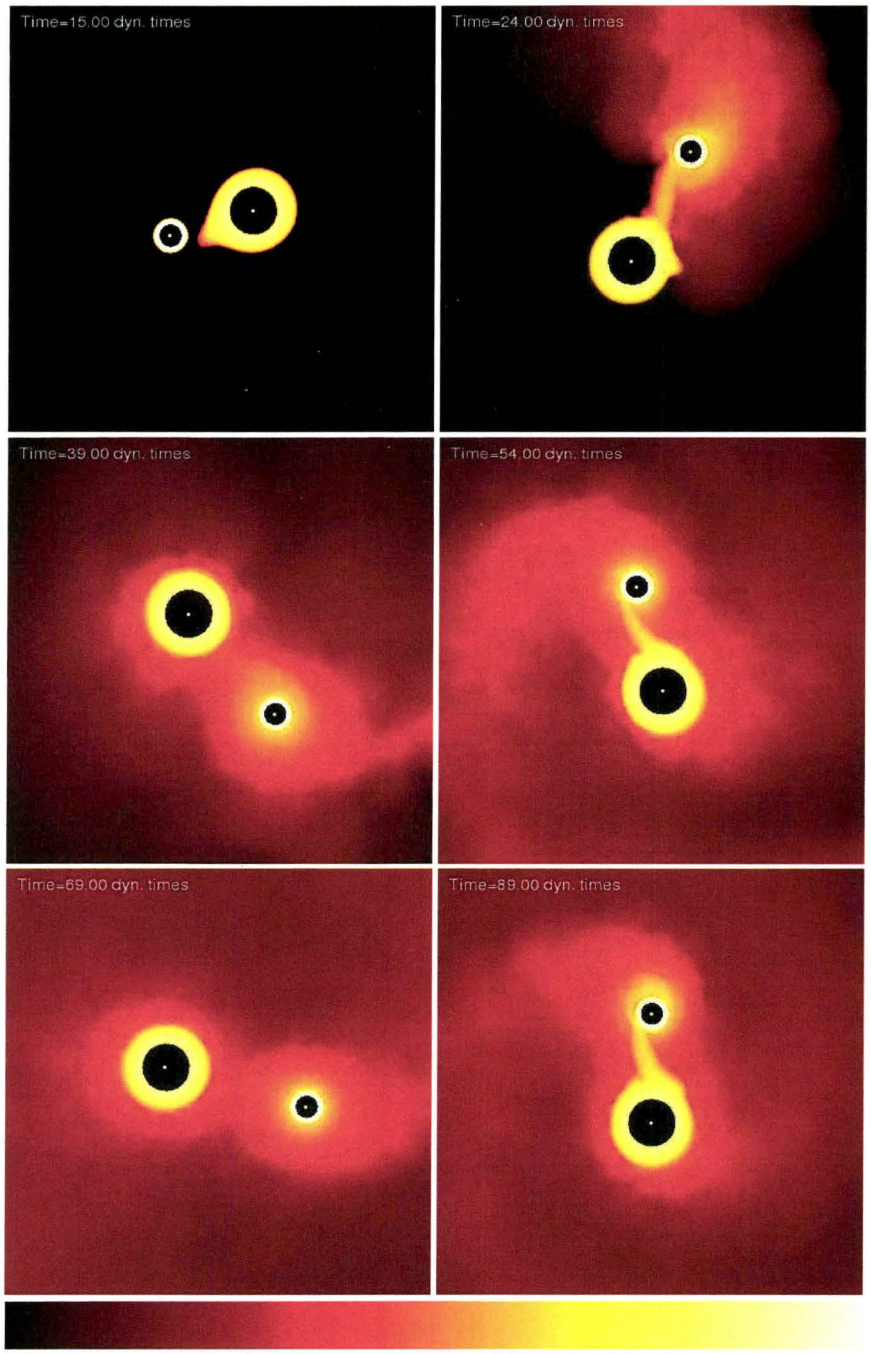

Figure 5.1 Logarithm of the density in the XY-plane for Model 3 ($e = 0.25$). Each image is 12 $R_\odot$ by 12 $R_\odot$ and the density scale ranges from 10^{-10} g cm^{-1} (dark) to 1 g cm^{-1} (white). Point masses are represented by the solid white dots and the orbital period is 31.80 τ_{dyn} ($\sim$ 14 hours).

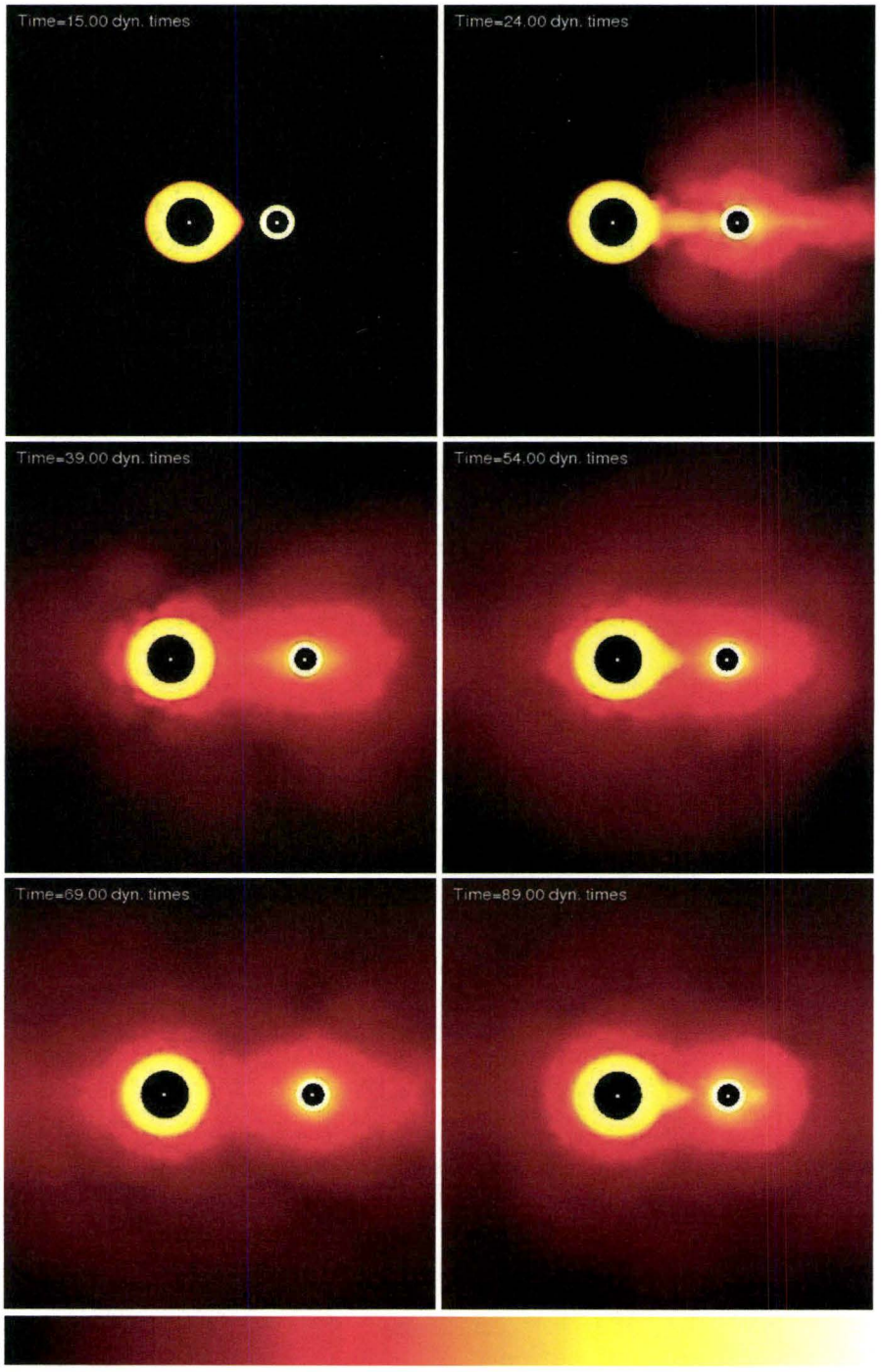

Figure 5.2 Similar to Figure 5.1 but in the XZ-plane.

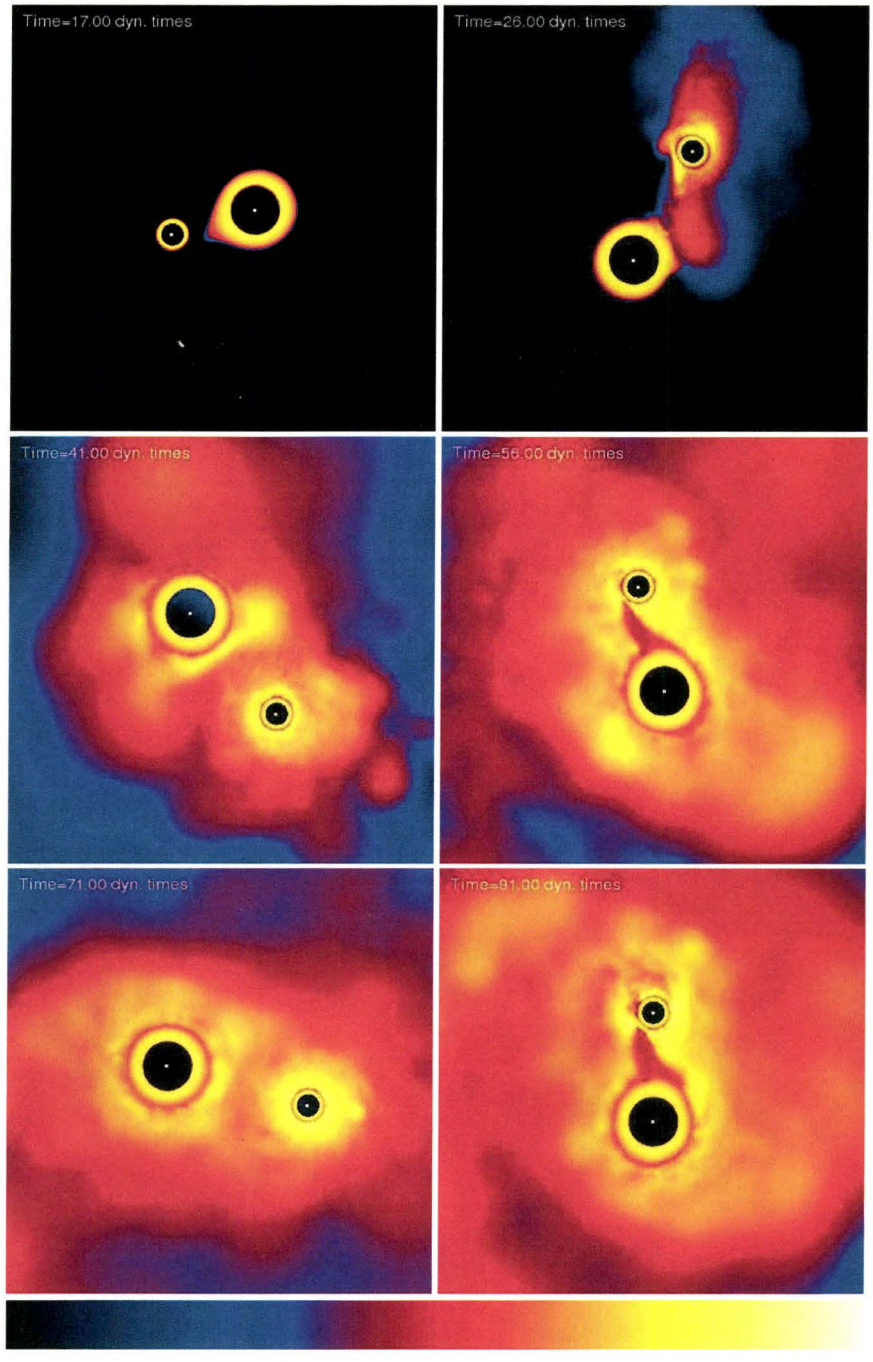

Figure 5.3 Logarithm of the internal energy in the XY-plane for Model 3 ($e = 0.25$). Each image is 12 $R_\odot$ by 12 $R_\odot$ and the internal energy scale ranges from 10^{12} erg g^{-1} (dark blue) to 10^{15} erg g^{-1} (white). Point masses are represented by the solid white dots and the orbital period is 31.80 τ_{dyn} ($\sim$ 14 hours).

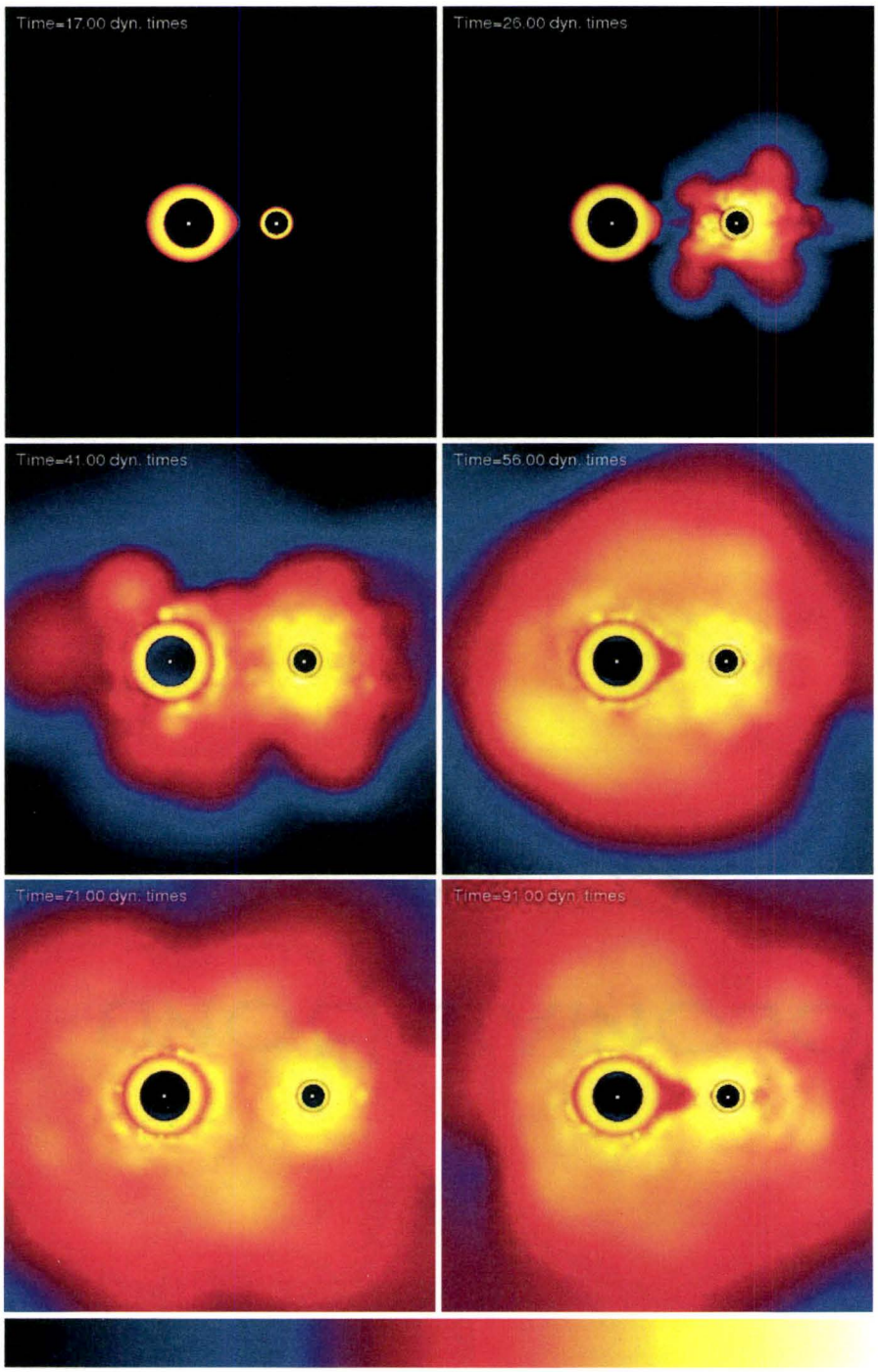

Figure 5.4 Same as Figure 5.3 but in the XZ-plane.

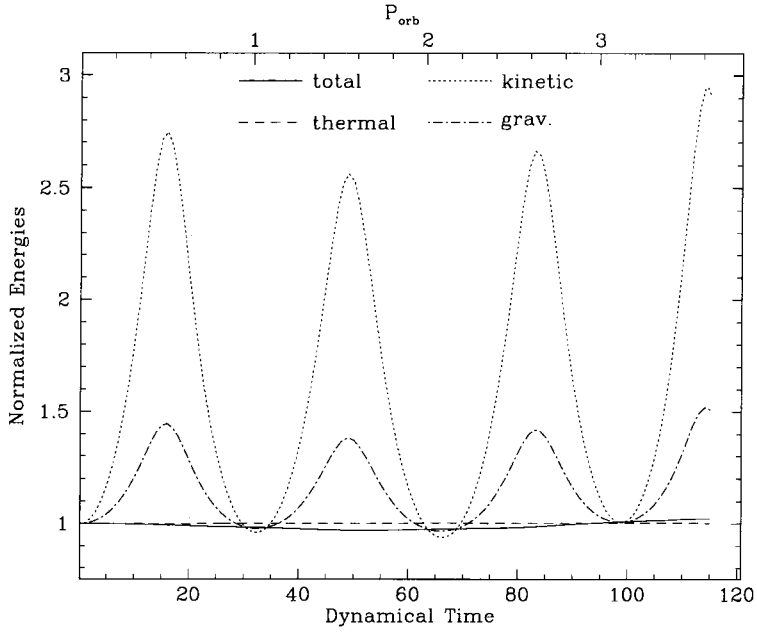

Figure 5.5 Different energies as a function of time for the 0.80+0.48 $M_\odot$ binary with $e = 0.25$.

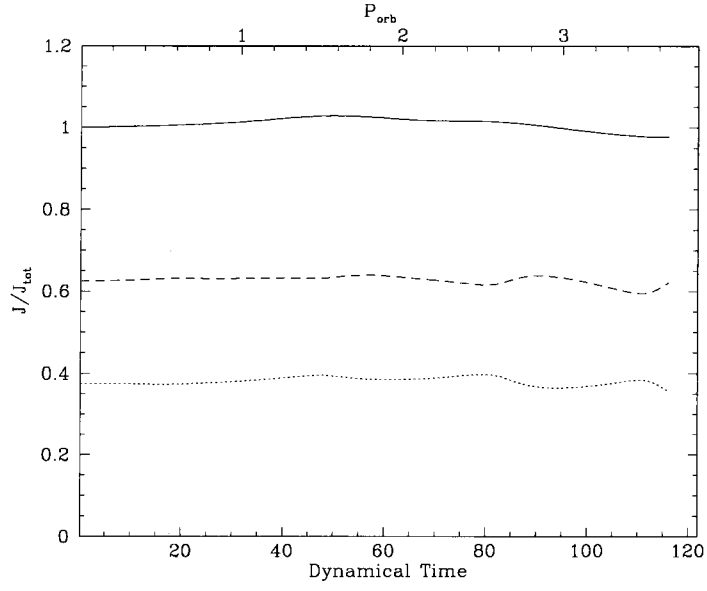

Figure 5.6 Total angular momentum (solid line) normalized to its initial value as a function of time for the $0.80 + 0.48$ $M_\odot$ binary with $e = 0.25$. The dotted (dashed) line corresponds to the primary's (secondary's) angular momentum.

5.2 1.50 $M_\odot$ + 1.40 $M_\odot$

The high-mass binary, on the other hand, is expected to behave differently since the secondary is much larger and its density is of the same magnitude as the primary. Therefore, we expect the infalling material to interact much more dynamically with the envelope of the secondary. To demonstrate the typical behaviours of our high-mass binaries, we show, in Figures 5.7 and 5.8, the logarithm of the density in the XY and XZ planes, respectively, for Model 8 ($e = 0.25$) at different times. Here, each panel is 18 $R_\odot$ by 18 $R_\odot$ and the density scale is much lower than in the low-mass binary case (e.g. Figures 5.1 and 5.2). The interaction between the two stars is much stronger here, as material from both stars is lost, and a clear spiral pattern is observed and most prominent towards the end of each mass transfer episode (i.e. after each periastron passage). At low eccentricity, the mass transfer is rather smooth and has little effect on the secondary. However, for Models 8 and 9, the systems almost come into contact at periastron and material from the secondary is being pushed around the secondary, thus becoming bound to the binary as a whole or to the ejecta. As discussed above, this was expected as the densities and particles masses of the two stars are very similar. Figure 5.8 shows that the material forms a rather sparse envelope around the two stars, unlike the $0.80 + 0.48$-$M_\odot$ binary where the accreted material was found only around the secondary. Similarly, the internal energy of this system follows the density closely, as shown by the spiral patterns in Figures 5.9 and 5.10. The view perpendicular to the orbital plane shows that most of the envelope surrounding both stars is relatively hot and seems to get heated up after the first periastron passage. Also, unlike the low-mass binary, we observe mass

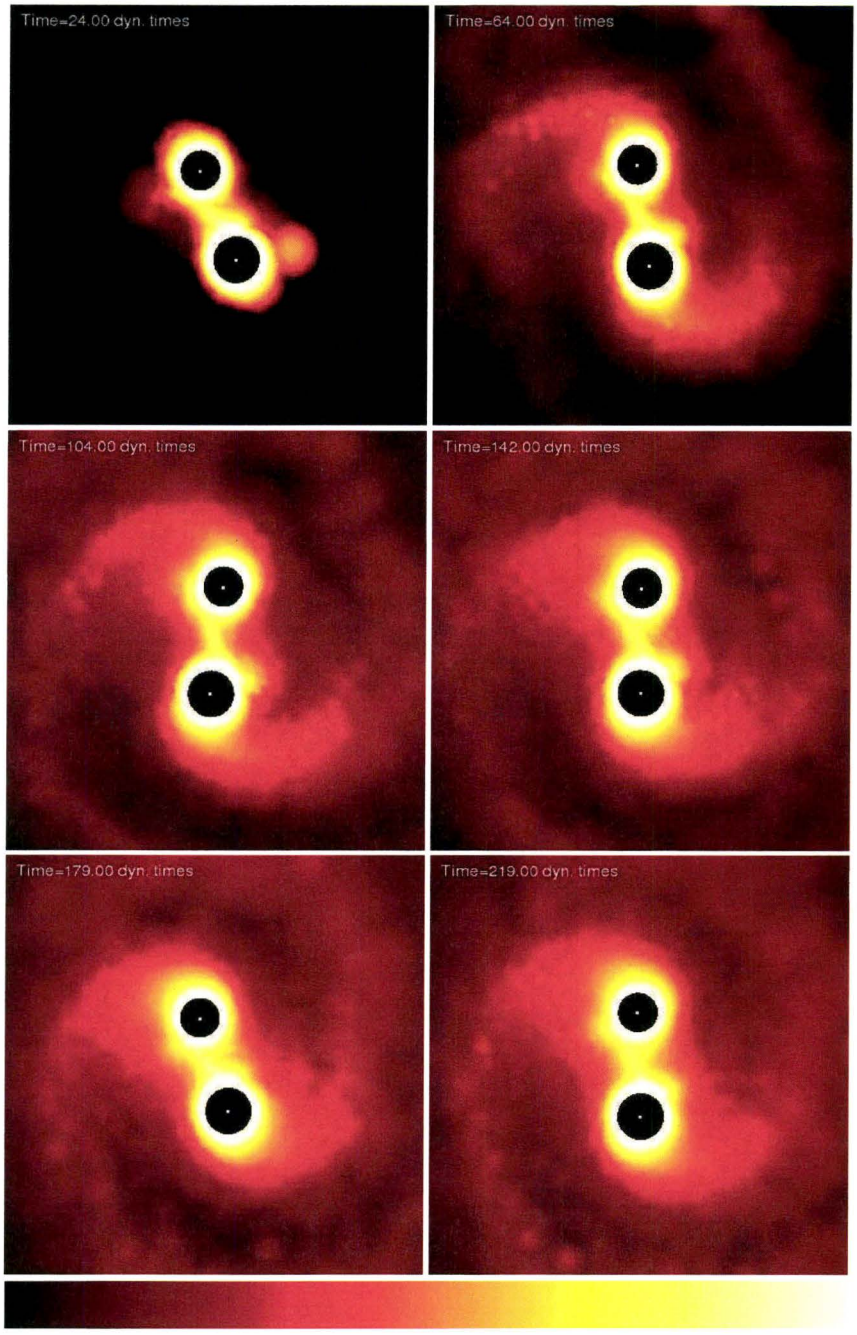

Figure 5.7 Logarithm of the density in the XY-plane for Model 8 ($e = 0.25$). Each image is 18 $R_\odot$ by 18 $R_\odot$ and the density scale ranges from 10^{-10} g cm^{-1} (dark) to 10^{-4} g cm^{-1} (white). Point masses are represented by the solid white dots and the orbital period is 38.80 τ_{dyn} ($\sim$ 17 hours).

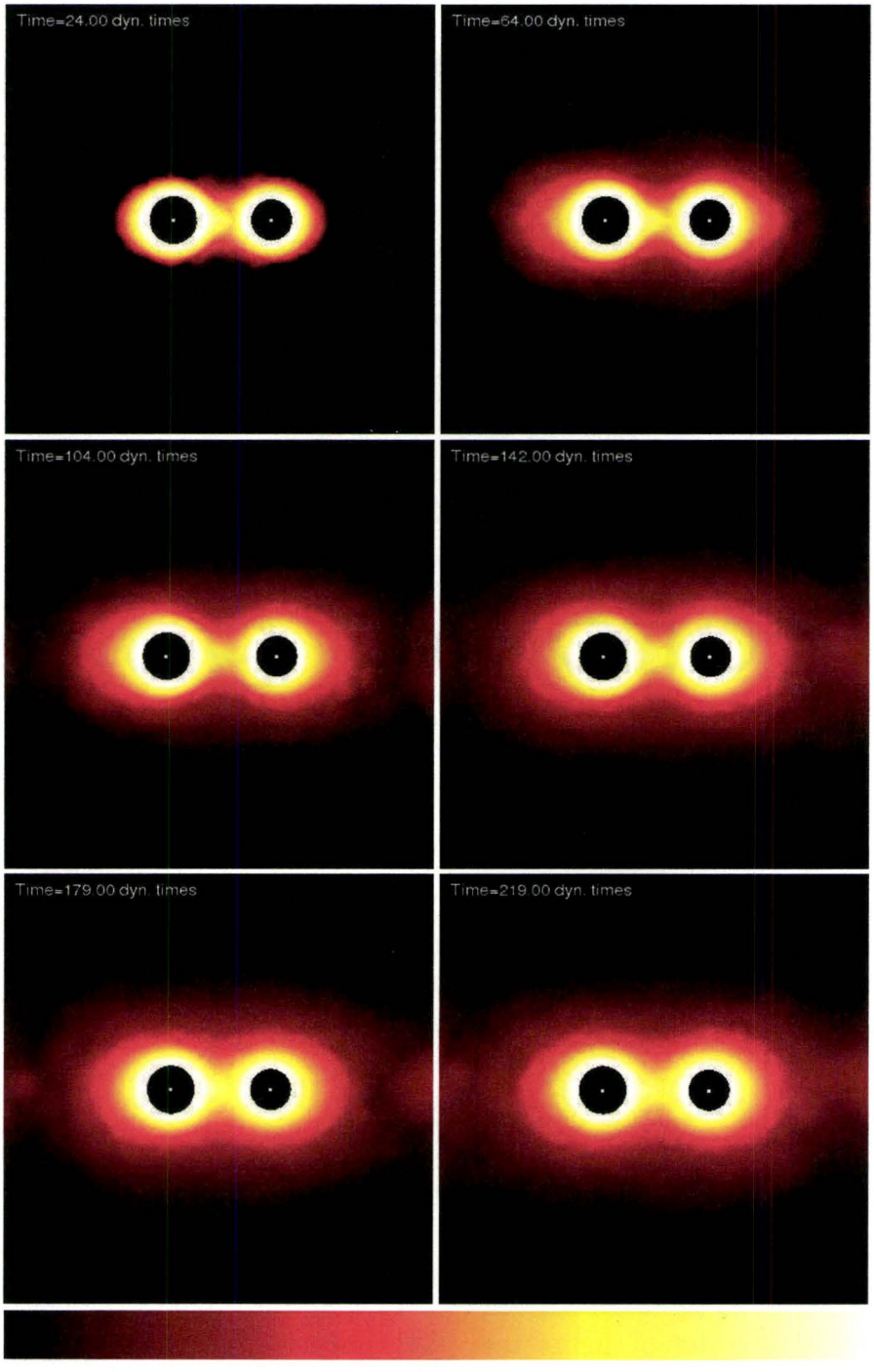

Figure 5.8 Same as Figure 5.7 but in the XZ-plane.

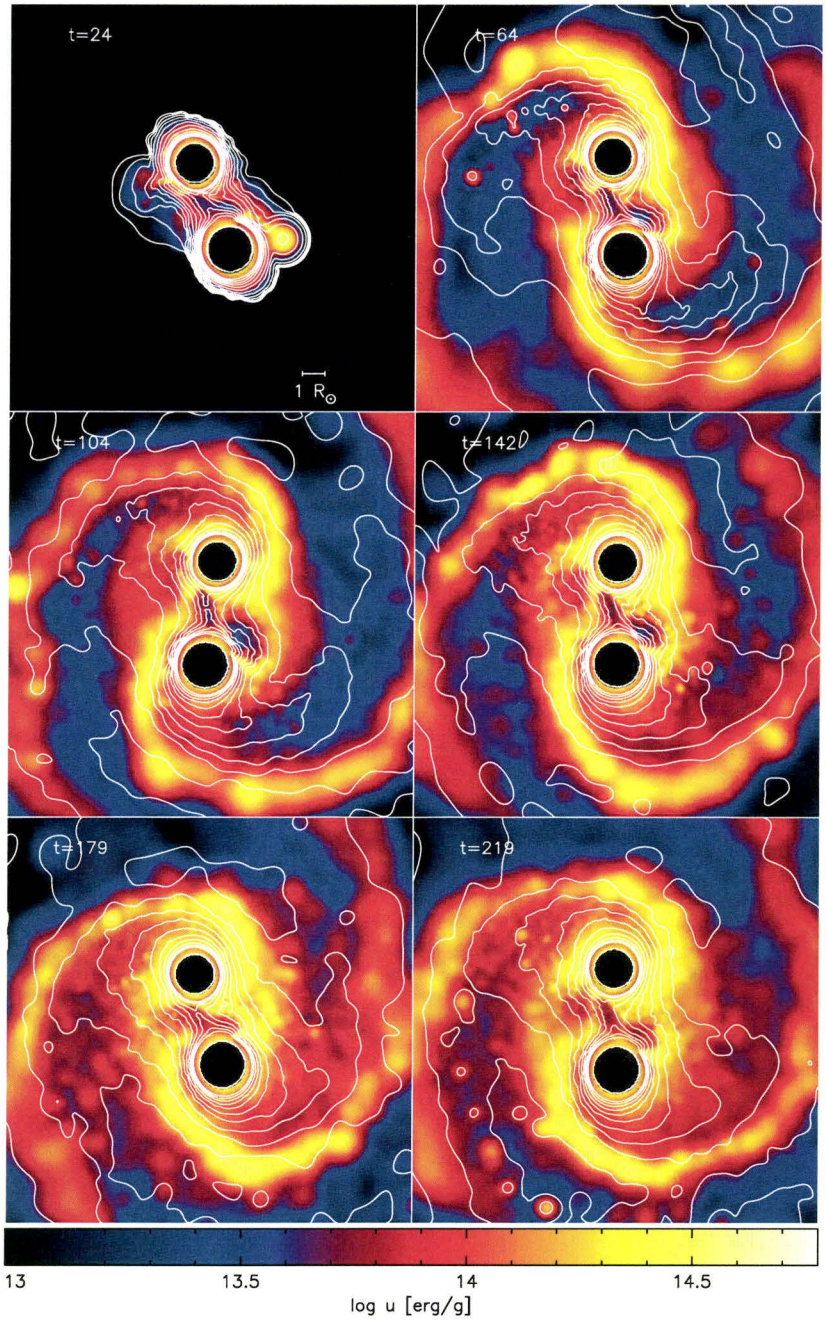

Figure 5.9 Logarithm of the internal energy along with density contours in the XY-plane for Model 8. Again, each panel is 18 $R_\odot$ by 18 $R_\odot$. The orbital period is 31.80 τ_{dyn} ($\sim$ 17 hours).

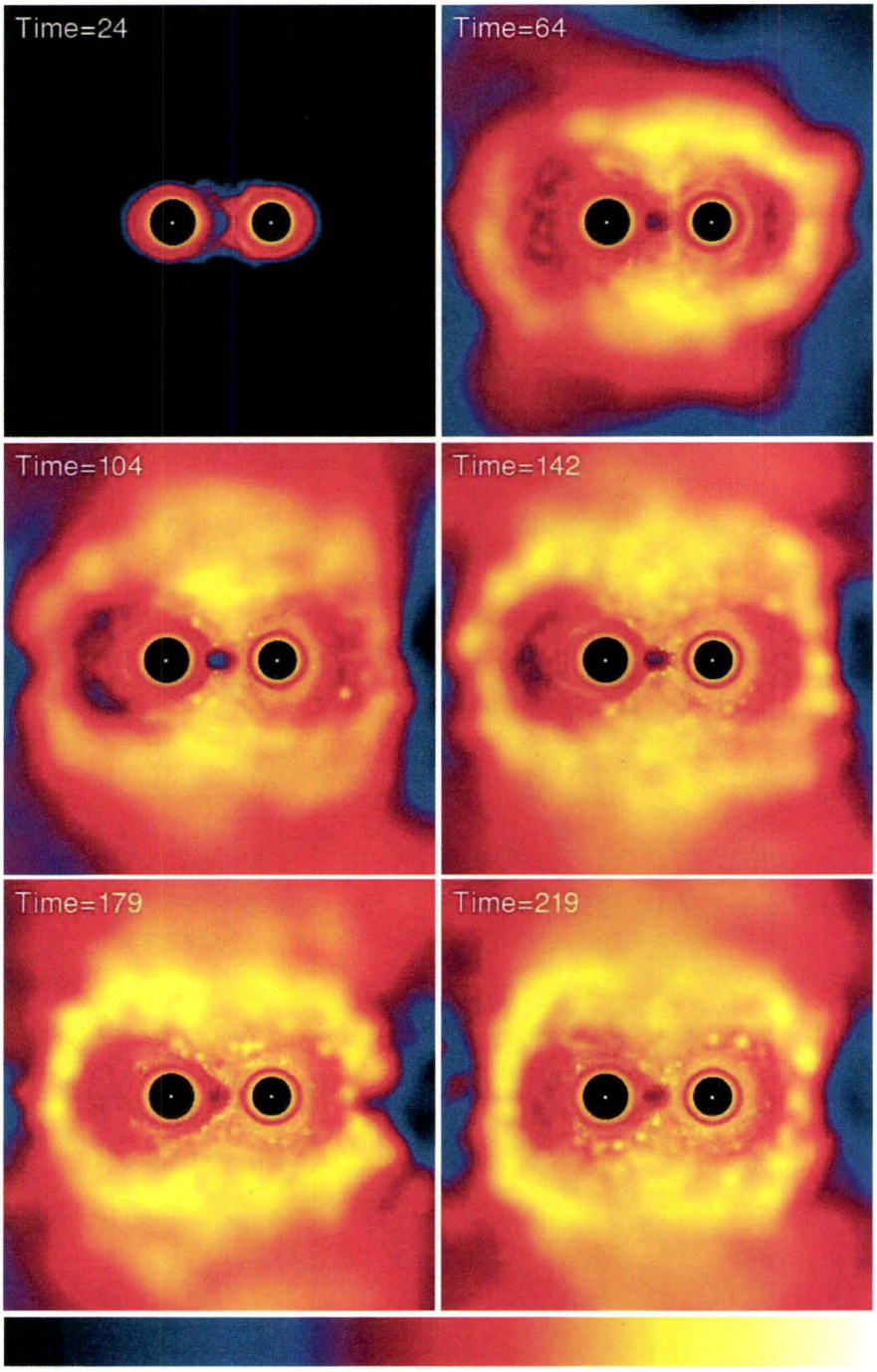

Figure 5.10 Logarithm of the internal energy in the XZ-plane for Model 8 ($e = 0.25$). Each image is 19 $R_\odot$ by 19 $R_\odot$ and the internal energy ranges from 10^{13} erg g^{-1} (dark blue) to 10^{15} erg g^{-1} (white).

loss through both the L_2 and L_3 points, which may be enhanced by the fact that asynchronism is substantial at periastron, thus lowering the potential at the L_3 point, as discussed in Chapter 2.

One particular feature of the simulation presented here is the interaction between the material lost by the stars and the surrounding material. Figure 5.9, which was made using SPLASH, a publicly-available visualization tool for SPH codes (Price, 2007), shows contours of logarithmic density on top of the thermal energy colour rendition. We can see that the density spiral arms lag behind the thermal energy arms, i.e. the hotter material precedes the dense material just lost by the stars. This pre-heating occurs because of the shock between the dense and fast-moving material just lost by the stars and the surrounding material, which is less dense and moving more slowly. This is more obvious in Figure 5.11, where we plot the logarithm of the entropy with the same density contours overlaid on top. In our code, entropy is generated in shocks only, and Figure 5.11 shows that, similarly to the lag between density and thermal energy, entropy is generated in front of the density waves, which suggests that the gas is being heated up by shocks. These shocks are produced by the fast moving material lost by the stars. Note that we do not see such shock heating in the low-mass binary simulations since there is only little mass lost from either stars to shock with the surrounding gas. Also, we see that almost no entropy is generated in the stream of material leaking through the L_1 point. As a matter of fact, our simulations show that this material cools down upon leaving the primary (due to adiabatic expansion; see Figures 5.9 and 5.10)) and no shocks are formed, which suggests that mass transfer is relatively gentle, in this case, despite the material hitting the surface of the secondary.

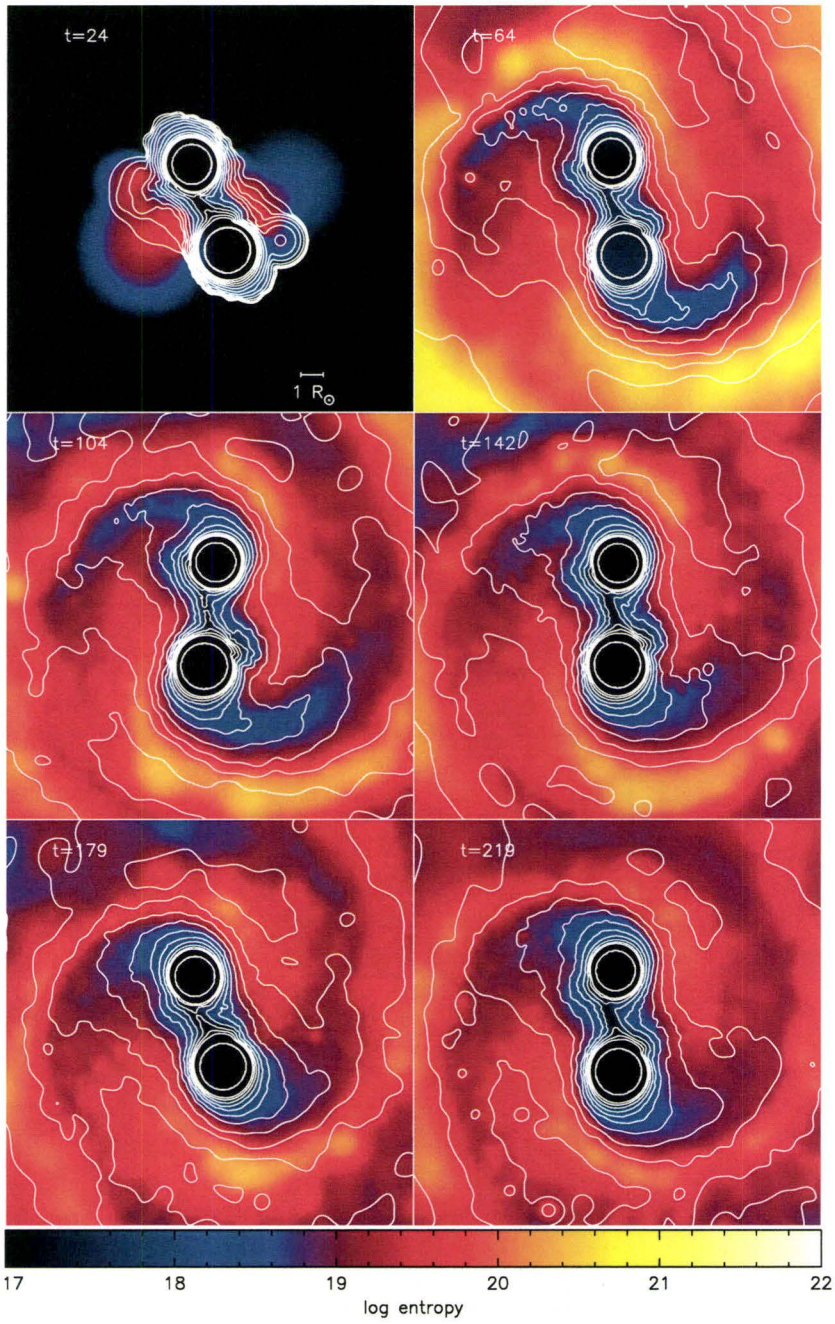

Figure 5.11 Logarithm of the entropy along with density contours in the XY-plane for Model 8 showing that entropy is generated right in front of the density waves, where material is hotter. This is suggestive of the gas being heated by shocks. Again, each panel is 18 $R_\odot$ by 18 $R_\odot$.

Finally, we show the different energies and total angular momentum for Model 8 in Figures 5.12 and 5.13. The different energies oscillate as a function of the orbital position, with the kinetic and gravitational energies reaching extrema at periastron. Remarkably, the kinetic energy always peaks at the same value and comes back to its initial value when at apastron, suggesting that the binary is well relaxed and that it follows the orbit it was initially put on. Also, the total energy changes by no more than $\sim 0.5\%$ over the whole duration of the simulation. We also notice that the total internal energy slowly increases, by 8% at the end of the simulation. This change in thermal energy comes at the expense of gravitational energy, but since 8% seems substantial, we emphasize that the total thermal energy represents roughly only 1 part in 1000 of both the kinetic and gravitational energies. Therefore, it would be hard to observe such a small change in gravitational energy on the scale of Figure 5.12. The total angular momentum of the system and of the two stellar components also remains constant during the entire simulation to a 1% level for the whole duration of the simulation.

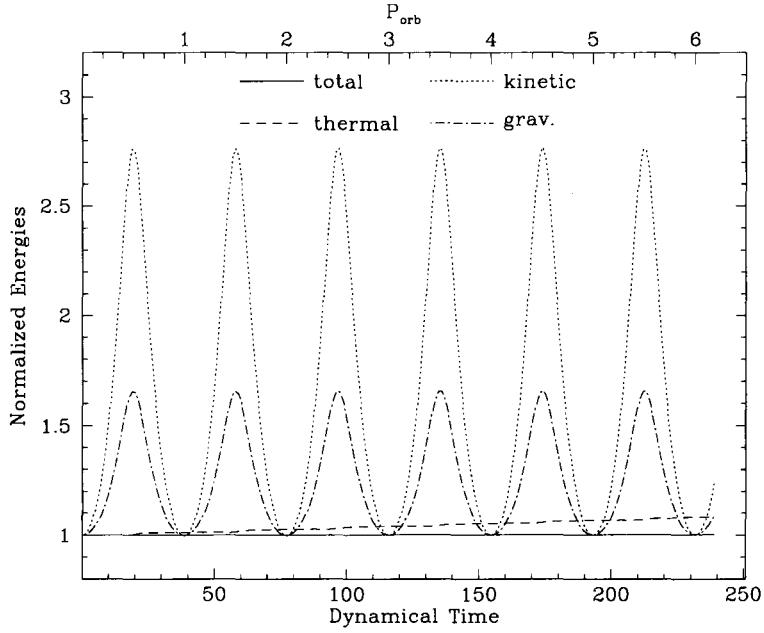

Figure 5.12 Different energies as a function of time for the 1.50+1.40 $M_\odot$ binary with $e = 0.25$.

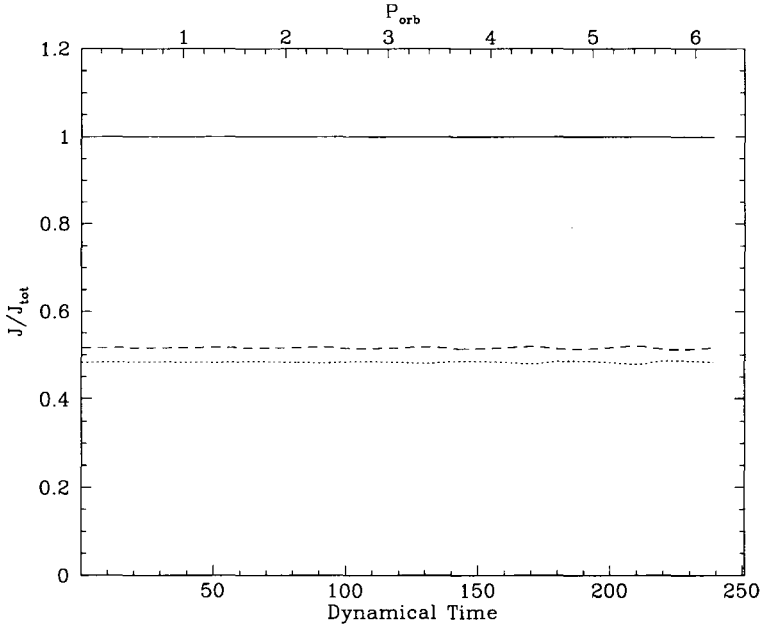

Figure 5.13 Total angular momentum (solid line) normalized to its initial value as a function of time for the $1.50 + 1.40$ $M_\odot$ binary with $e = 0.25$. The dotted (dashed) line corresponds to the primary's (secondary's) angular momentum.

5.3 Mass transfer rates

We now analyze more quantitatively the results of all of our simulations, with particular attention to the onset, duration, and rates of mass transfer. We also compare these rates to the theoretical expectations and estimates presented in Chapter 2.

5.3.1 Determination of bound mass

First, we need to determine the component to which every SPH particle is bound. We do so by using a energy criterion, as presented by Lombardi et al. (2006) and determine whether a particle is bound to the primary, the secondary, or the binary as a whole based its total energy with respect to the component under consideration. In particular, given that most of the mass of the two stars is contained in the point masses, we use the latter as the main components to which particles are bound. For a particle to be bound to any of the components, we require that its total energy relative to that component to be negative. Here, the different components are the primary, the secondary, and the binary as a whole, the latter with a total mass $M_1 + M_2$. The total energy per unit mass of any particle with respect to both the point masses and the binary's centre of mass is defined as

$$E_{ij} = \frac{1}{2}v_{ij}^2 + u_i - \frac{G(M_j - m_i)}{d_{ij}} \tag{5.1}$$

where v_{ij} and d_{ij} refer to the relative velocity and separation, respectively, between particle i and component j. Moreover, we require the separation d_{ij} to be less than the current separation of the two centres of mass of the

stars (in this case, the point masses). For particles that satisfy both of these criteria for both stellar components, we assign them to the stellar component for which the total energy is most negative. If only the energy condition is satisfied for the stellar components, or the energy with respect to the binary is negative, the particle is assigned to the binary component. Finally, if the total relative energy is positive, the particle is unbound and is assigned to the ejecta. A schematic of the criterion on the separation between an SPH particle and the stellar components is shown in Figure 5.14. One caveat of this method is that if a particle just happens to have the same velocity as any of

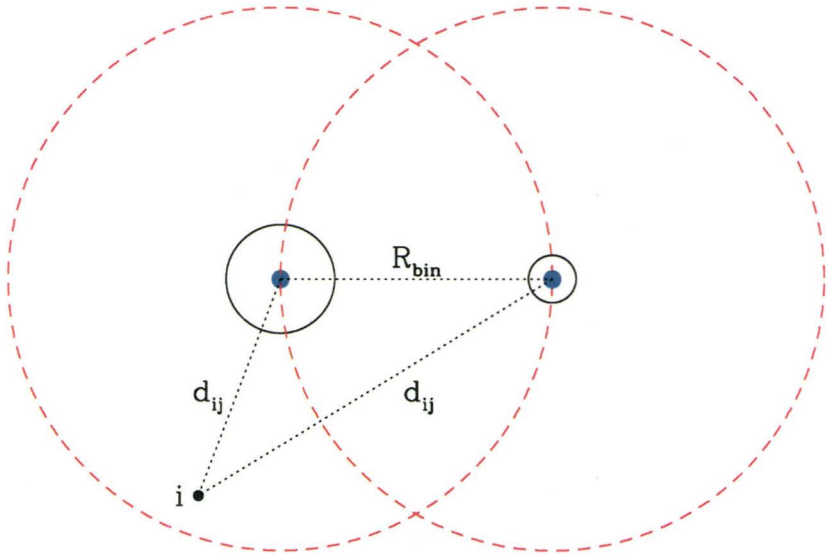

Figure 5.14 Schematic showing how the bound mass of each component is determined based on the separation between the particle and the components. The stars and point masses are represented by the black circles and blue dots and the distance within which particles can be bound to either stellar components are delimitated by the red circles. Here, if the energy of particle i is negative, it would be bound to the larger star because $d_{ij} < R_{bin}$. Therefore, any particle located outside the red circles would not be bound to either stellar components, but could be bound to the binary if its energy is negative.

the components, then its relative kinetic energy is zero and the particle is more likely to be assigned to that component rather than any other. Although this probably happens in our simulations, we do not observe any discrepancies in the assignment of the bound particles as the total number of particles assigned to all the components is constant (see below; Figure 5.15 and 5.16). For lack of a better approach to determine the components' bound mass, we use this method.

Figures 5.15 and 5.16 present snapshots from Models 3 and 8, respectively, showing to which component particles located close to the equatorial plane are bound. The different colours show the particles bound to the primary (red), the secondary (blue), the binary as a whole (green), and the ejecta (black). We see that particles close to either star are bound to the stars themselves, whereas material in the mass transfer stream suddenly becomes bound to the secondary as it is getting closer to it. Material that was already transferred from the primary forms an envelope around the secondary that is bound to the latter. In particular, in the low-mass binary case (Figure 5.15), the accreted mass onto the secondary also remains bound to it whereas in the high-mass binary case (Figure 5.16), the fluffy common envelope surrounds both stars and is mostly bound to both stellar components. In both simulations, however, only a few particles are actually observed to be bound to the binary envelope and/or the ejecta, although Figures 5.15 and 5.16 only show particles located close to the orbital plane. We will discuss the mass loss in §5.5.

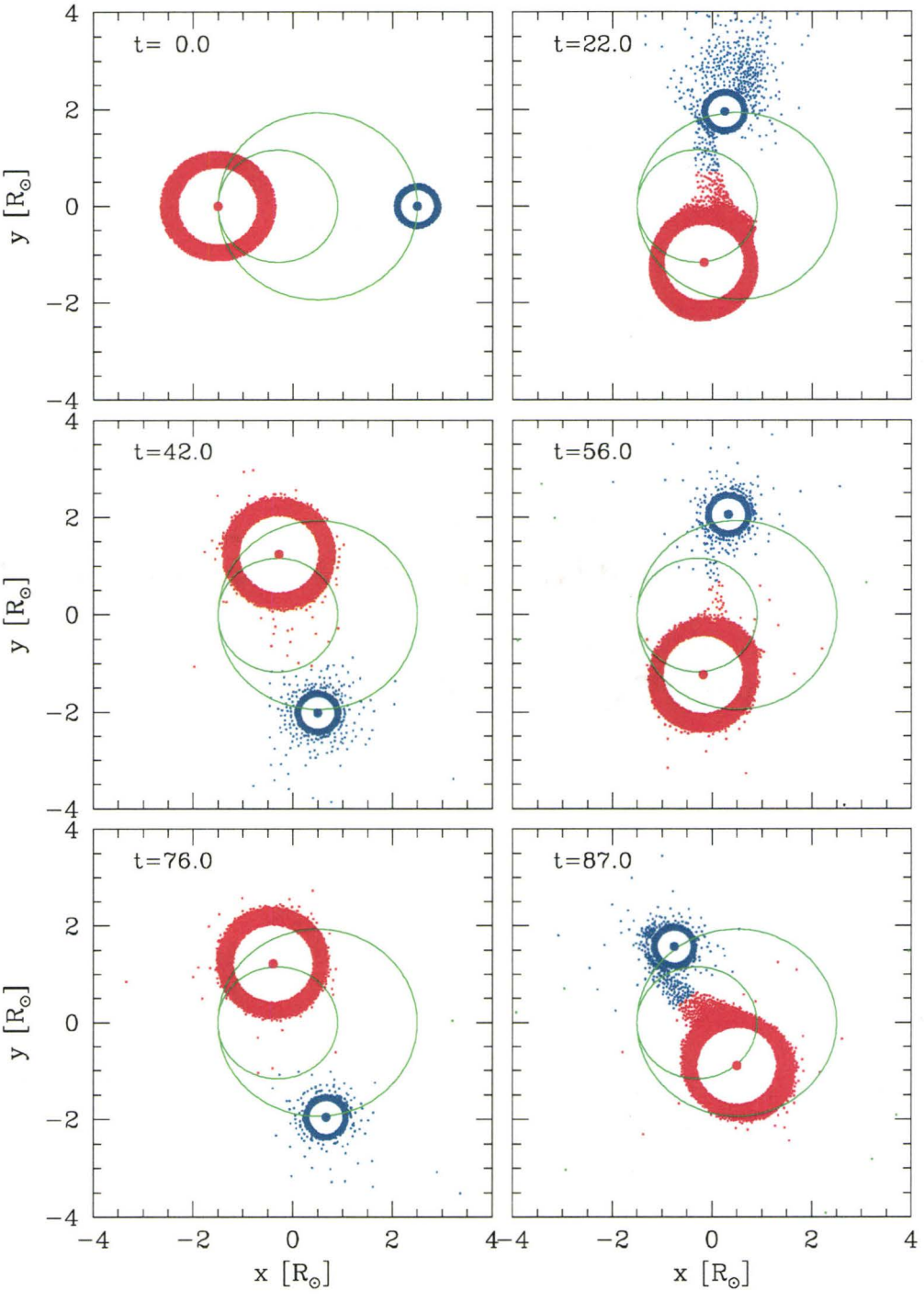

Figure 5.15 Colour-coded plots showing the mass bound to each component of the $0.80 + 0.48$ $M_\odot$ system with $e = 0.25$. Red particles are bound to the primary; blue to the secondary; green to the binary; and black are ejected from the system. The green circles represent the paths of each star along their respective eccentric orbit. The orbital period is $\sim 31.8\ \tau_{dyn}$.

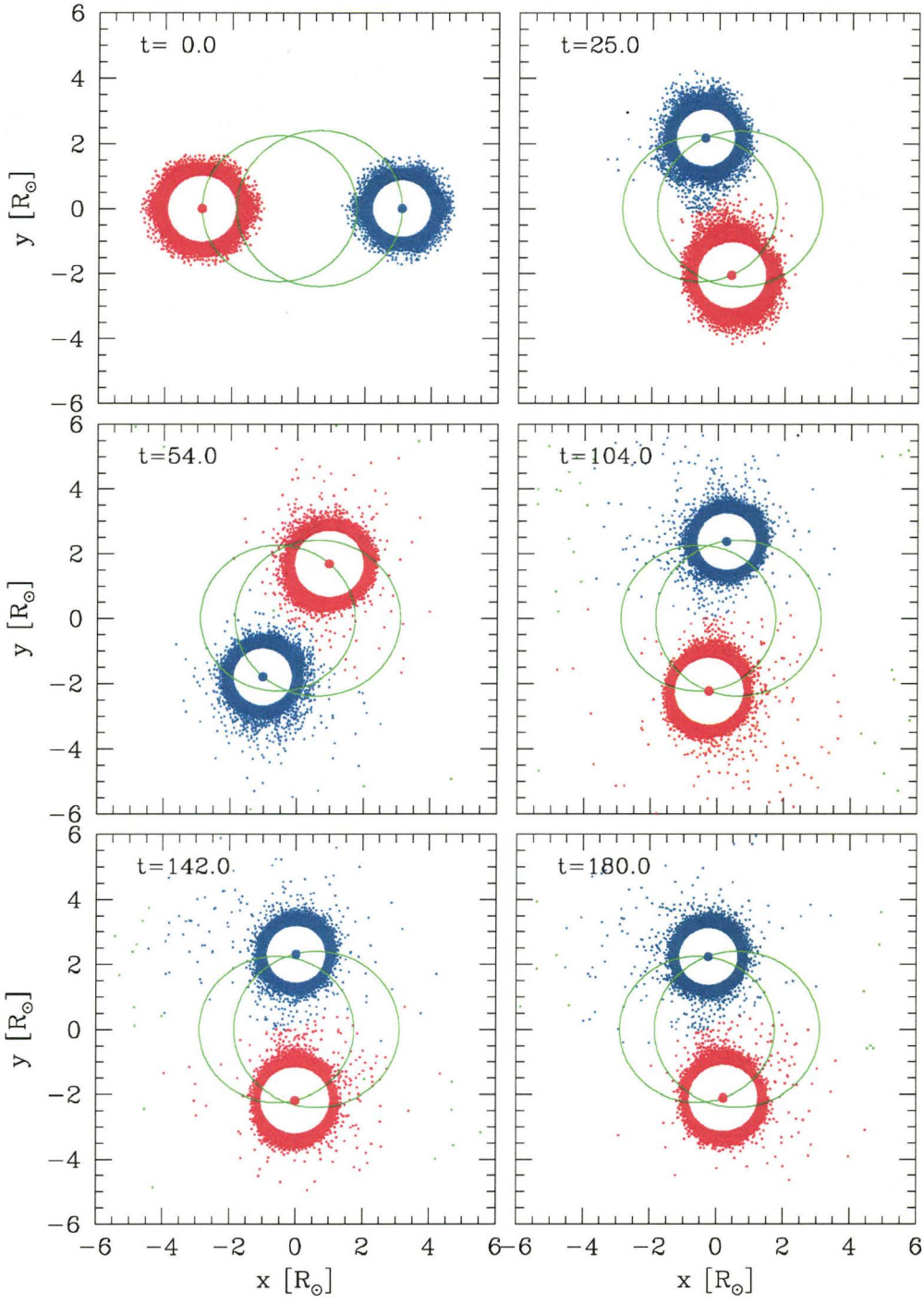

Figure 5.16 Same as Figure 5.15 but for the $1.50 + 1.40$ $M_\odot$ binary with $e = 0.25$. The orbital period is $\sim 38.8\ \tau_{dyn}$.

Based on this method for determining the particles bound to each component, we can calculate the total bound mass as a function of time. This is shown in Figure 5.17 for the low-mass binaries and Figure 5.18 for the high-mass binaries. Each Figure plots the change in bound mass (left column) and the change in the number of bound particles (right column) for all four components of the systems. Again, red is for the primary, blue for the secondary, green for the binary, and magenta for the ejecta. First, in all cases, the total mass and total number of particles remains constant, as shown by the dotted black line. This is indicative that our method for determining to which component a particle belong does not assign any particle to more than one component. Second, clear and distinct episodes or mass transfer (and accretion) can be observed for the primary and secondary. These episodes occur periodically and have a finite duration in time. For cases where mass transfer does occur, the bound mass for the stellar components changes in a stepwise fashion, representative of the episodic mass transfer and accretion. Also, in most cases, the changes in mass of the secondary mirrors that of the primary. Moreover, no matter which binary system we look at, the higher the eccentricity, the more mass is lost from the primary and accreted onto the secondary. The fact that the bound mass seems to increase for the primary after each periastron passage is due to matter falling back on it. This is obvious especially for the low-mass binaries. Similarly, the number of particles usually behaves in the same way as the total mass of the components, i.e. it increase in a stepwise fashion. However, this is not true for the high-mass binaries with $e = 0.25$ and $e = 0.30$, as can be seen in Figure 5.18, where the total mass bound to the secondary increases whereas the total number of particles bound to it remains almost the same. Upon examination of these two simulations,

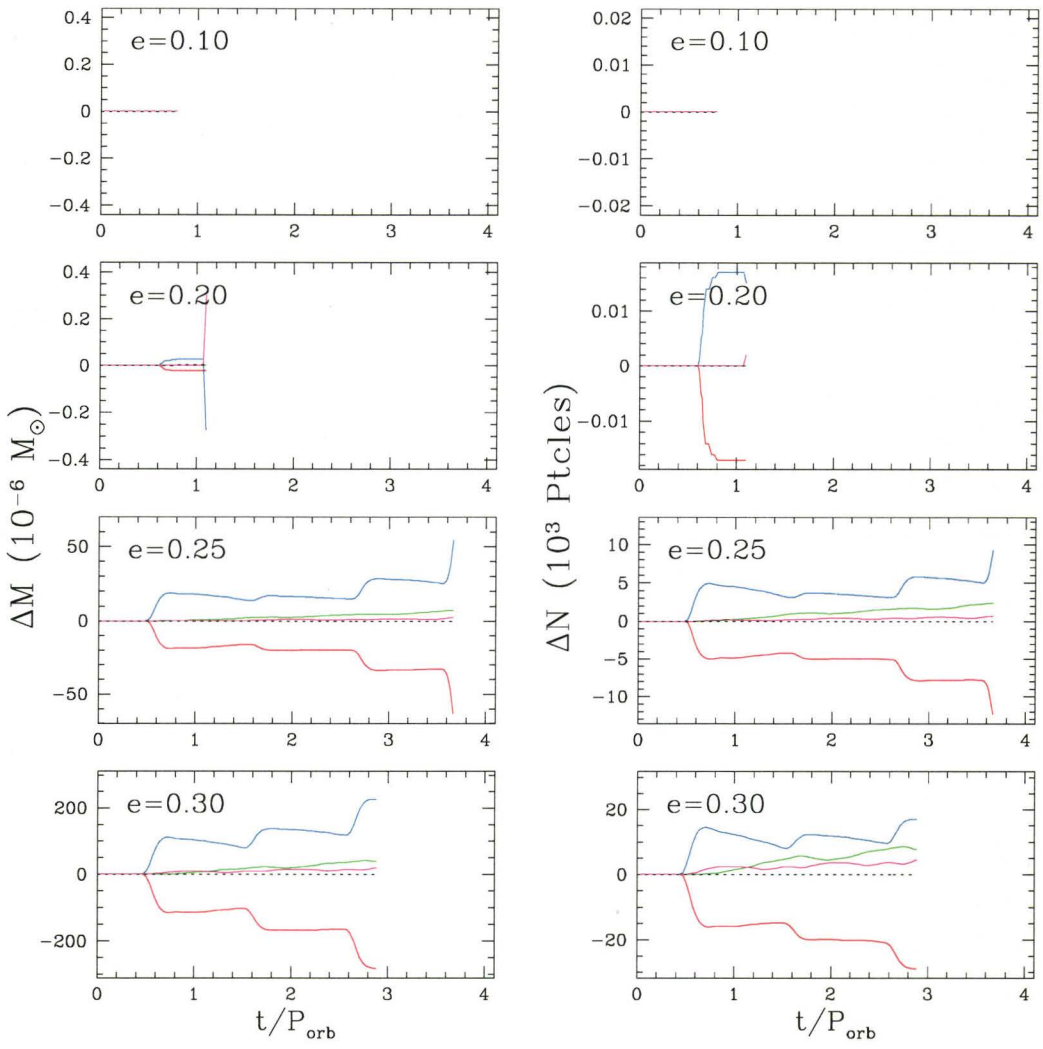

Figure 5.17 Change in bound mass (left) and number of bound particles (right) for the primary (red), secondary (blue), binary (green), and ejecta (green) as a function of time and eccentricity for the $0.80 + 0.48$ $M_\odot$ system. The black dotted line is the sum of all four components and shows that both the total mass and particle number remain constant.

it is observed that the systems come very close to contact at periastron, i.e. the secondary also barely fills its Roche lobe, and particles from the secondary are lost in this process. Also, the abrupt change in the bound masses for the low-mass binary with $e = 0.20$ is due to the fact that only a handful of parti-

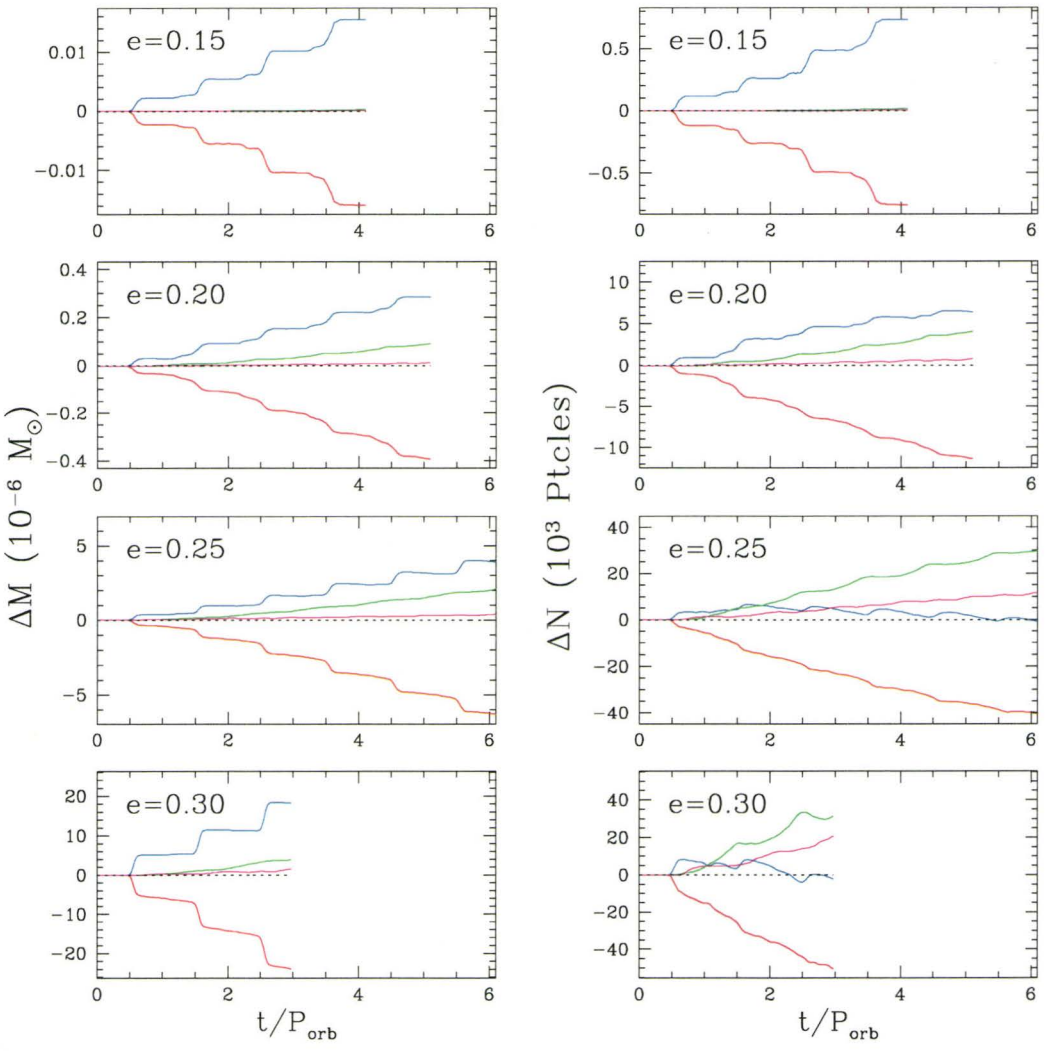

Figure 5.18 Change in bound mass (left) and number of bound particles (right) for the primary (red), secondary (blue), binary (green), and ejecta (green) as a function of time and eccentricity for the $1.50 + 1.40$ $M_\odot$ system. The black dotted line is the sum of all four components and shows that both the total mass and particle number remain constant.

cles are transferred to the secondary and our code can hardly deal with such a situation (see § 6.2). Indeed, Figure 5.19 shows the changes in mass and particle bound to the secondary only, where the contributions from particles initially bound to the primary and to the secondary are plotted in red and

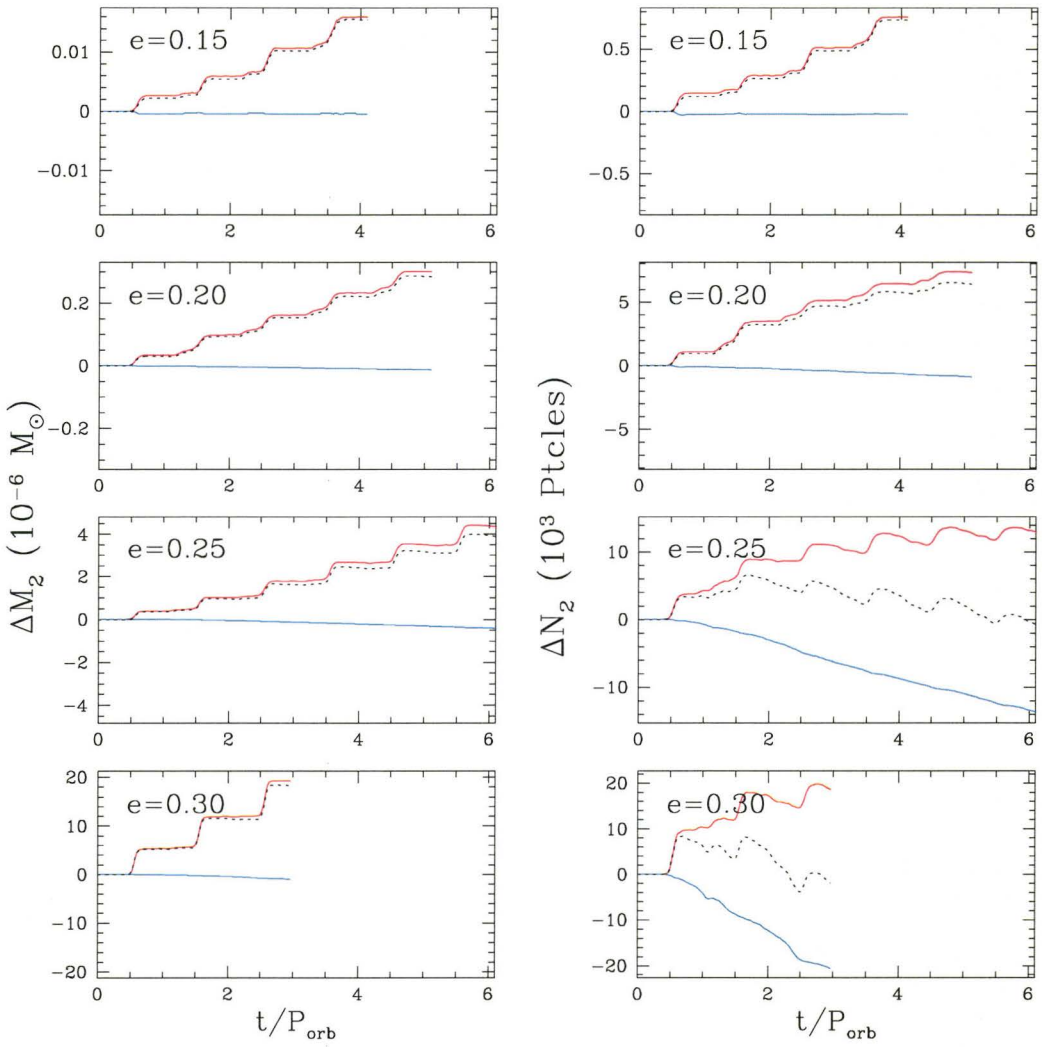

Figure 5.19 Mass and number of particles bound to the secondary as a function of time for the 1.50+1.40 $M_\odot$ system. The blue line represents the contribution from particles initially (and still) bound to the secondary while the red line represents the contribution from particles initially bound to the primary. For the $e = 0.25$ and $e = 0.30$ cases, the secondary loses almost as many of its own particles as it accretes particles from the primary (right panel), but the total mass accreted is much larger than that lost (left panel). The dotted black line represents the net changes in bound mass and particle number.

blue, respectively. The dotted black line is the sum of both contributions and is to be compared with the blue line in Figure 5.18. For cases with low eccentricity (i.e. $e \leq 0.20$), the secondary barely loses any of its own particles and

its change in bound mass is almost solely due to accretion of material from the primary. For higher eccentricity, the secondary loses a substantial number of its own particles. The number of particles lost is actually comparable to the number of particles accreted from the primary, thus making the net change in the number of bound particles almost zero. However, the total mass of these lost particles amounts only to a small fraction of the total mass of the particles coming from the primary, therefore increasing the net total mass bound of the secondary. This result is rather surprising as we did not expect that the material from the secondary could be lost. We do not see this behaviour in the low-mass binaries because the secondary is so far within its Roche lobe and so dense that it is hardly affected by the periastron passage and the infalling material. Since this is observed only at relatively high eccentricities, we suggest that this is due to the fact that the secondary slightly overfills its Roche lobe and to the interaction between the secondary's outer layers and the infalling material from the primary. Finally, we note that the mass in the binary envelope and the ejecta seems to slightly lag behind the changes in mass of the primary and the secondary. This suggests that material does not instantly end up in the envelope or the ejecta, but rather is first transferred to the secondary and then, if the latter can not keep it within its potential well, lost to the outer components.

5.3.2 Rate and duration of mass transfer

Using the previous results on the total bound mass of the stellar components as a function of time, we now determine the mass transfer rates for every system modeled. We use a simple approach to determine the instantaneous

mass transfer rates based on the difference of the total mass bound of each component between two successive timesteps, which we write as

$$\dot{M} = \frac{M_t^i - M_{t-1}^i}{\Delta t}, \tag{5.2}$$

where M refers to the *bound* mass, as determined using the prescription of §5.3.1, and the indices refer to component i and timesteps `t` and `t-1`. Figures 5.20 and 5.21 show the mass transfer and accretion rates as a function of time and eccentricity for the stellar components in the 0.80+0.48 $M_\odot$ and 1.50+1.40 $M_\odot$ systems, respectively. For the primary (red lines), we plot the negative of the mass transfer rates, i.e. $-\dot{M}$, so that we can compare it to the (positive) accretion rate of the secondary. In most cases, the mass transfer rates are well defined and peak right after the periastron passages. For the low-mass binary, mass transfer occurs only for eccentricity greater than ~ 0.20, as also shown in Figure 5.17. In these cases, the mass transferred from the primary is almost totally accreted by the secondary, as shown by the reciprocity of the red and blue lines. We note also that both rates sometime dip in the negative part of the plots, meaning that some material is falling back onto the primary and that the secondary is losing some mass. In particular, the glitch in the panel for $e = 0.25$ in Figure 5.20 is unreal as at this particular moment, particles are penetrating the boundary and the code reacts by re-injecting them in the envelope. In this case, it produces this flare of mass loss from the secondary. For lower eccentricities (e.g. $e = 0.10 - 0.20$), only a few particles are actually transferred and either the mass transfer is insignificant or the code fails to correctly handle the few tens of particles wandering in between the two stars. Finally, we note that the maximum mass transfer rates generally increases

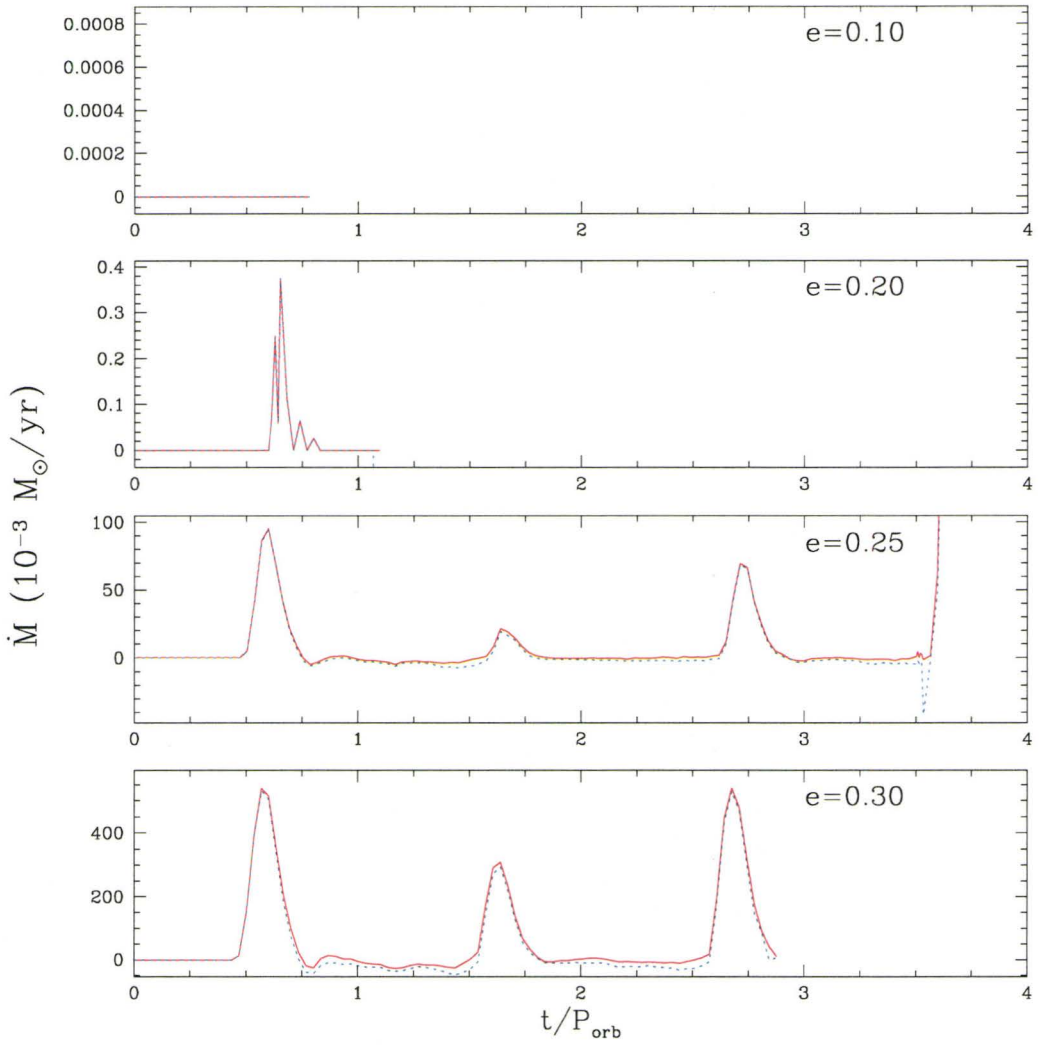

Figure 5.20 Mass transfer rates as a function of orbital period and eccentricity for the $0.80 + 0.48$ $M_\odot$ binary. The red and blue curves represent the mass transfer and accretion rates of the primary and secondary, respectively.

slightly with time, although the need for a larger number of orbits might be necessary to better constrain the behaviour of the maximum mass transfer rate.

The high-mass binary simulations, on the other hand, all display the characteristic episodic mass transfer peaks, with increasingly large mass transfer rates. Interestingly, the maximum mass transfer rates once again all peak

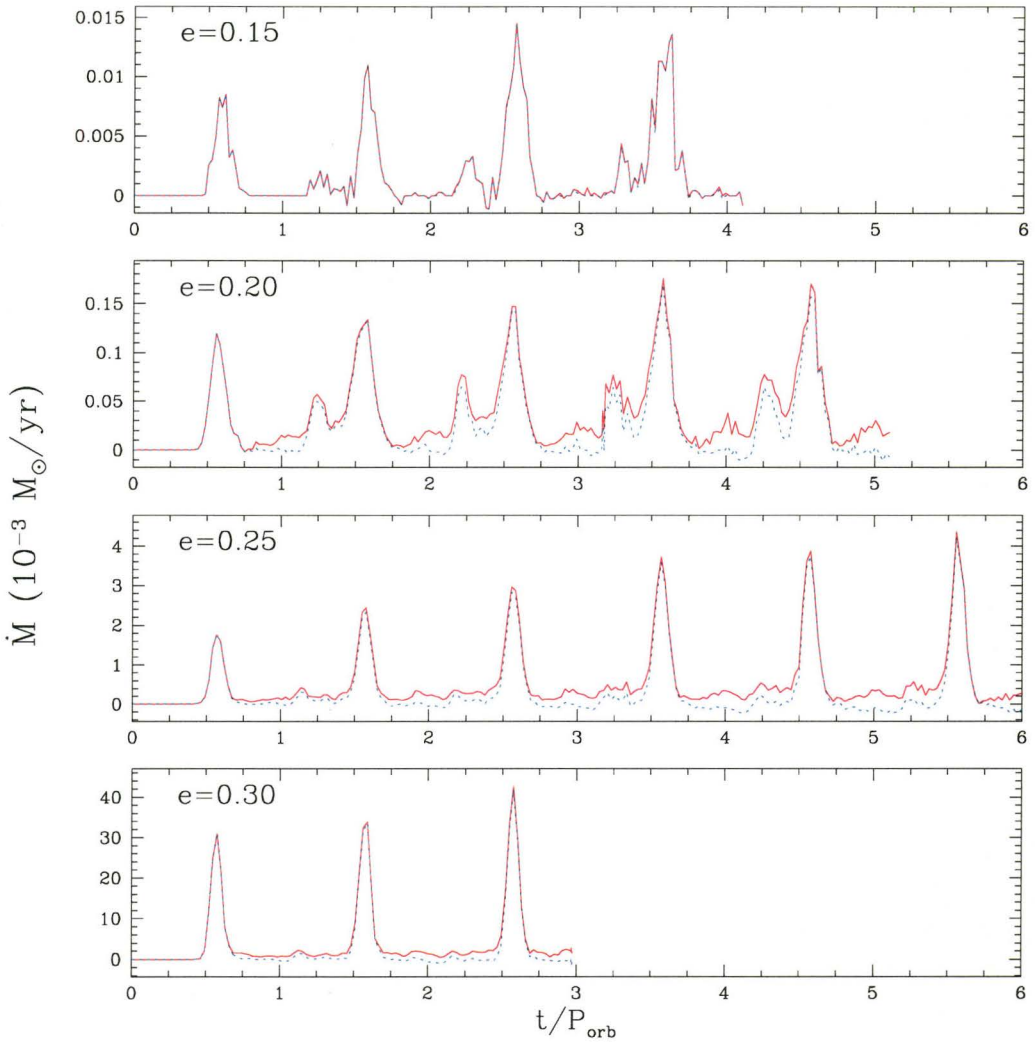

Figure 5.21 Mass transfer rates as a function of orbital period and eccentricity for the 1.50 + 1.40 $M_\odot$ binary. The red and blue curves represent the mass transfer and accretion rates of the primary and secondary, respectively.

shortly after periastron, although the two smallest eccentricities show quite a bit of noise in between these peaks. This noise is due to material falling back onto either or both stellar components in between periastron passages. In most instances, the material lost by the primary is almost all accreted onto the secondary, although the accretion rates of the secondary shows some differences with respect to the mass loss rates of the primary, suggesting that

some mass is lost from the system (see also Figure 5.18). Once again, the maximum mass transfer rate increases with time for any given eccentricity, although we note that such an increase might level off at some later time. The $e = 0.20$ case is rather noisy and there seems to be a significant fraction of the mass transferred that falls back onto the primary and secondary after the main episodes of mass transfer. This seems to be important only in the smaller eccentricity cases. The primary's mass transfer rates rarely becomes negative, unlike the secondary's accretion rates, which is mostly negative in between periastron passages, suggesting that the secondary loses mass. We note however that mass becomes bound to the secondary (and the primary) only temporarily as subsequent episodes of mass transfer may be energetic enough to plow through the surrounding of the secondary and eject some of this material.

Finally, we note the similarity in the position, duration, and shape of the mass transfer rate episodes. In particular, their shape is suggestive of a Gaussian function. We now attempt to fit these peaks with Gaussians in order to further characterize the mass transfer episodes.

5.3.2.1 Gaussian fits to mass transfer episodes

Using the mass transfer rates of Figure 5.20 and 5.21, we now try to fit a Gaussian function to each mass transfer episode. The general Gaussian functions we use has the following form:

$$\dot{M}(t) = A \exp\left(-\frac{(t-\mu)^2}{2\sigma^2}\right) + D \tag{5.3}$$

where A is the maximum amplitude, μ is the centre of the Gaussian, σ is proportional to the width of the Gaussian and D is the background (or continuum) mass transfer rate. The latter parameter is used to measure the background noise as, in some cases, the mass transfer rates do not fall back to zero in between mass transfer episodes. All the free parameters are fitted using the nonlinear least-squares method of Levenberg-Marquardt (Press et al., 1992). Here, the χ^2 is defined as

$$\chi^2(\mathbf{a}) = \sum_{i=1}^{N} \left[\frac{y_i(x_i) - y(x_i; \mathbf{a})}{\sigma_i} \right]^2, \tag{5.4}$$

where $\mathbf{a}$ are the free parameters, $y_i(x_i)$ the data point at x_i, $y(x_i; \mathbf{a})$ the model value at x_i with the (actual) values of $\mathbf{a}$, and σ_i the individual standard deviation of the data points. Starting with an oriented guess for each parameter, which we get from observations of our data points, the Levenberg-Marquardt technique minimizes the value of the χ^2 by iteratively adjusting all free parameters. Note that here, we use only the data points for one period at a time to determine the four parameters of any mass transfer episode. Typically, our minimization technique usually converges in $10 - 15$ iterations. We fit the height of the Gaussian extended wings so that the width of the Gaussian matches more closely the data points. However, in cases where matter falls back onto either or both stars between periastron passages, the fitting procedure is to be taken with care. The Gaussian fits to the mass transfer episodes are shown in Figures 5.22 to 5.25 for all simulations where this is possible. The parameters obtained from the fitting procedure are also provided on each plot. Open dots are data points to which we assign a relatively large error, and hence do not contribute to the fitting procedure, since they are part of

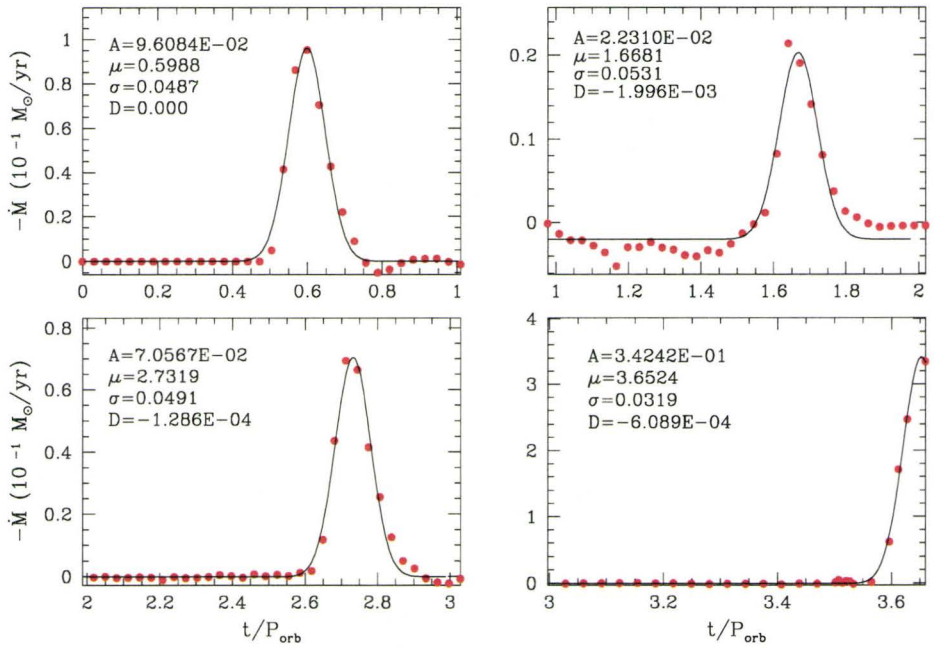

Figure 5.22 Gaussian fits to the primary's mass transfer episodes for the 0.80+0.48 $M_\odot$ binary with $e = 0.25$. See text for more details.

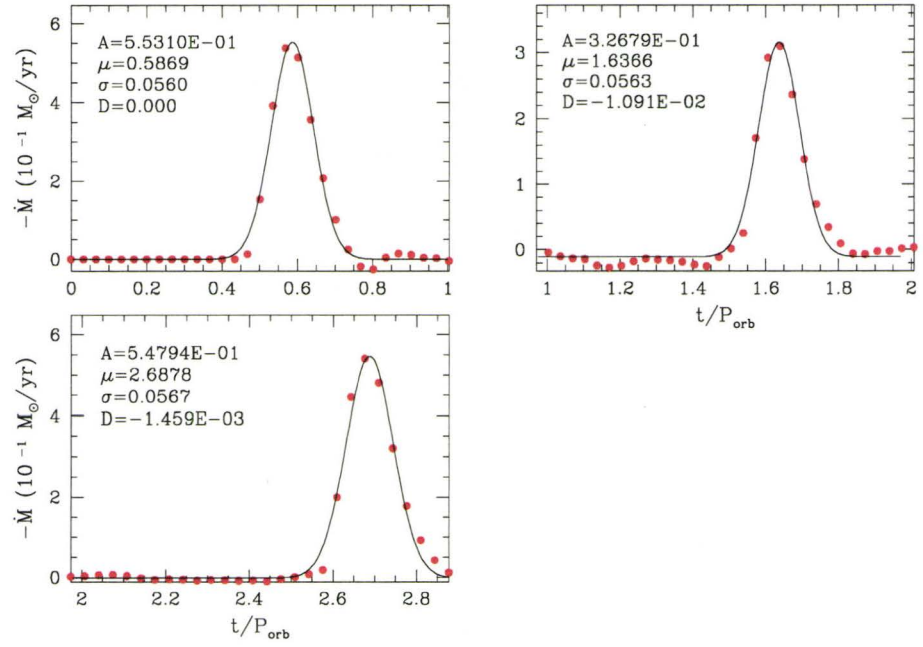

Figure 5.23 Same as Fig. 5.22 but for the $e = 0.30$ case.

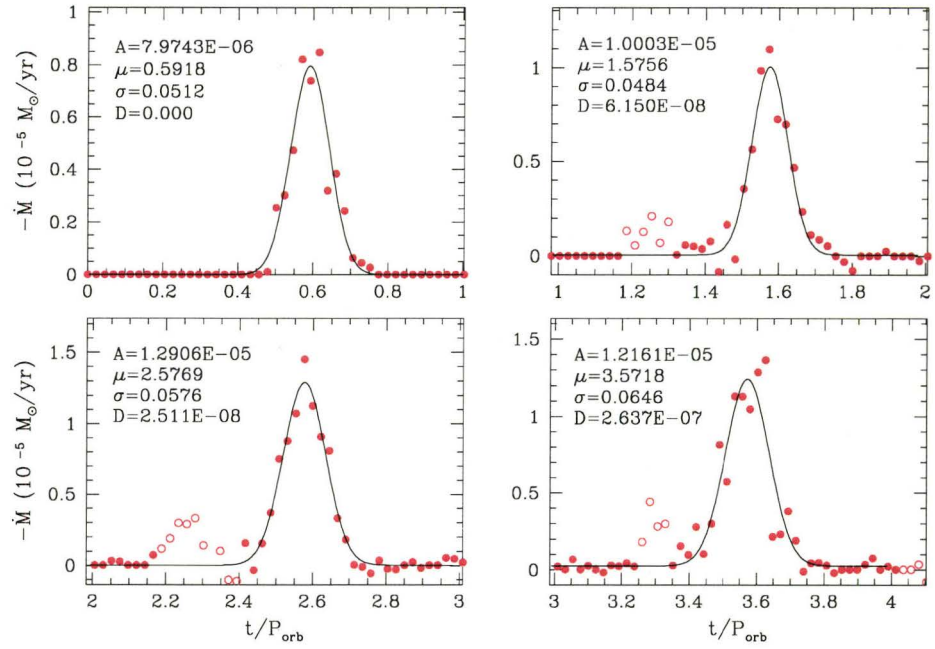

Figure 5.24 Gaussian fits to the primary's mass transfer episodes for the 1.50+1.40 $M_\odot$ binary with $e = 0.15$. Open circles are data points which are not taken into account when fitting the free parameters.

the pre-periastron mass transfer episodes and do not contribute to the main episode of mass transfer. Note that doing so does not significantly change the values of both μ and σ. Moreover, for every first episode of mass transfer, we do not fit the continuum (parameter D) as we expect the value of the mass transfer rate prior to the first periastron passage to be identically zero. We do fit this parameter for any subsequent peak however, as noted in each panel.

For most of our simulations, it is quite remarkable how well a Gaussian can fit the data points. In most cases, the amplitude, centre, and width all match closely the data points. Again, for cases where matter is observed to fall back onto the stars (see, e.g., Figures 5.17 and 5.18), the fits to the height of the extended wings is obviously not as reliable. In particular, the Gaussian fit for the low-mass binary with an eccentricity $e = 0.20$ is not reliable as the

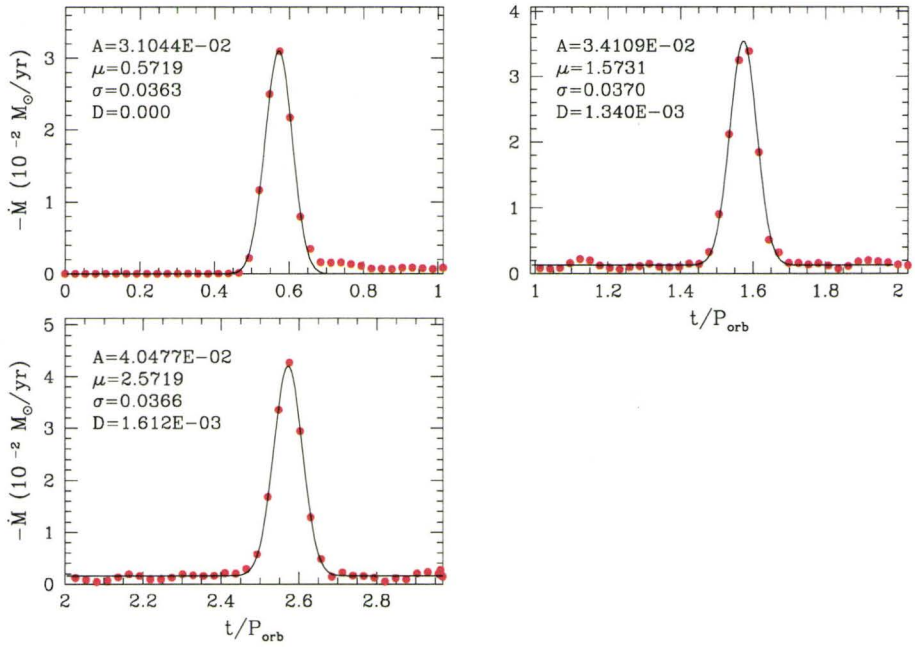

Figure 5.25 Same as Figure 5.24 but for the $e = 0.30$ case.

mass transfer curve of Figure 5.20 is too noisy. For all other cases, the fits we get are significantly reliable. However, an important source of uncertainty on these fitted parameters, especially A and D, is probably the noise on either side of the peaks seen in the data. On the other hand, the width and amplitude of most (if not all) of the mass transfer episodes are well fitted with a Gaussian.

We plot, in Figure 5.28, the amplitude, centre, and width of all the Gaussians we fitted as a function of eccentricity. Many trends can be seen in this Figure. First, the maximum mass transfer rate increases with the eccentricity. This is expected since as the eccentricity increases, the periastron distance gets smaller and the two stars get closer to each other, thus facilitating mass transfer. Our results also suggest that the maximum mass transfer rate increase linearly with the eccentricity, although we also expect a cut-off at

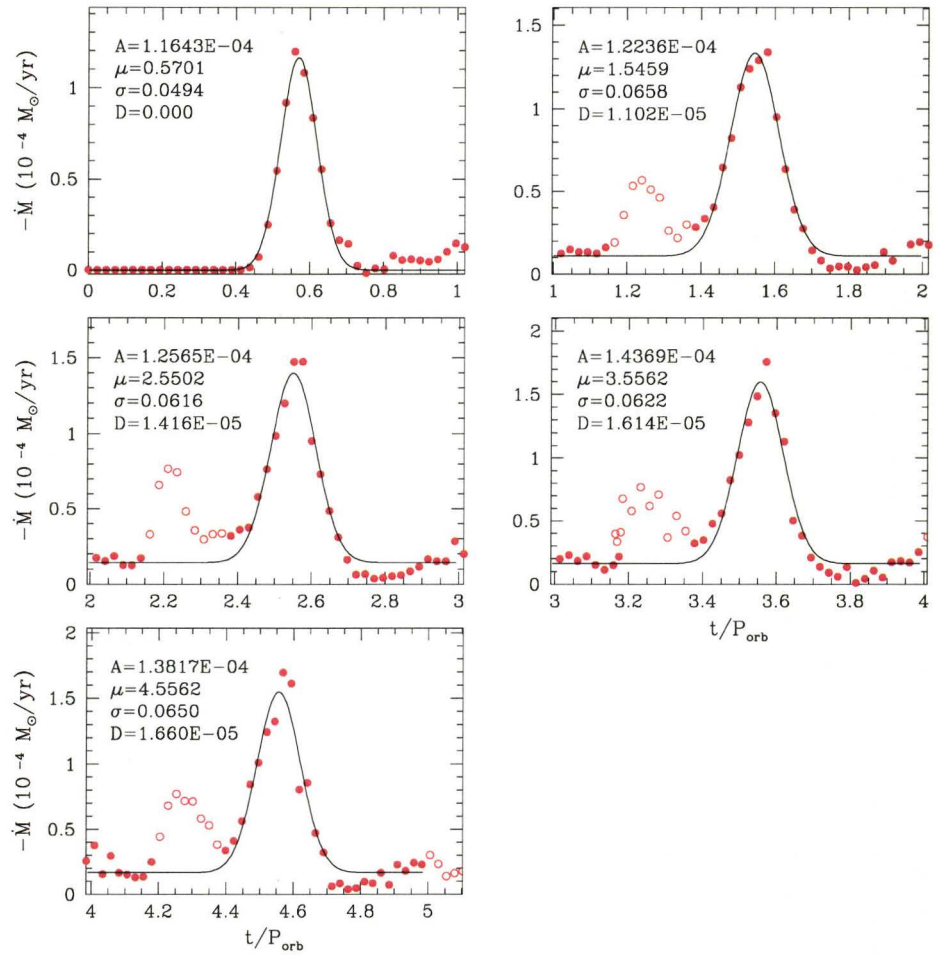

Figure 5.26 Same as Figure 5.24 but for the $e = 0.20$ case. Open circles are data points which are not taken into account when fitting the free parameters.

low eccentricity where the primary will not fill its Roche lobe even when at periastron. Also, although we only have two data points from our low-mass binary simulations, these two simulations suggest a similar linear trend. As for the position where the maximum mass transfer rate occurs, the results from our high-mass binary simulations clearly show that mass transfer rates peak at an orbital phase slightly larger than periastron, around $0.55 - 0.57$. Although mass transfer starts around periastron, it only peaks later when the two stars have already started getting further away from each other. This

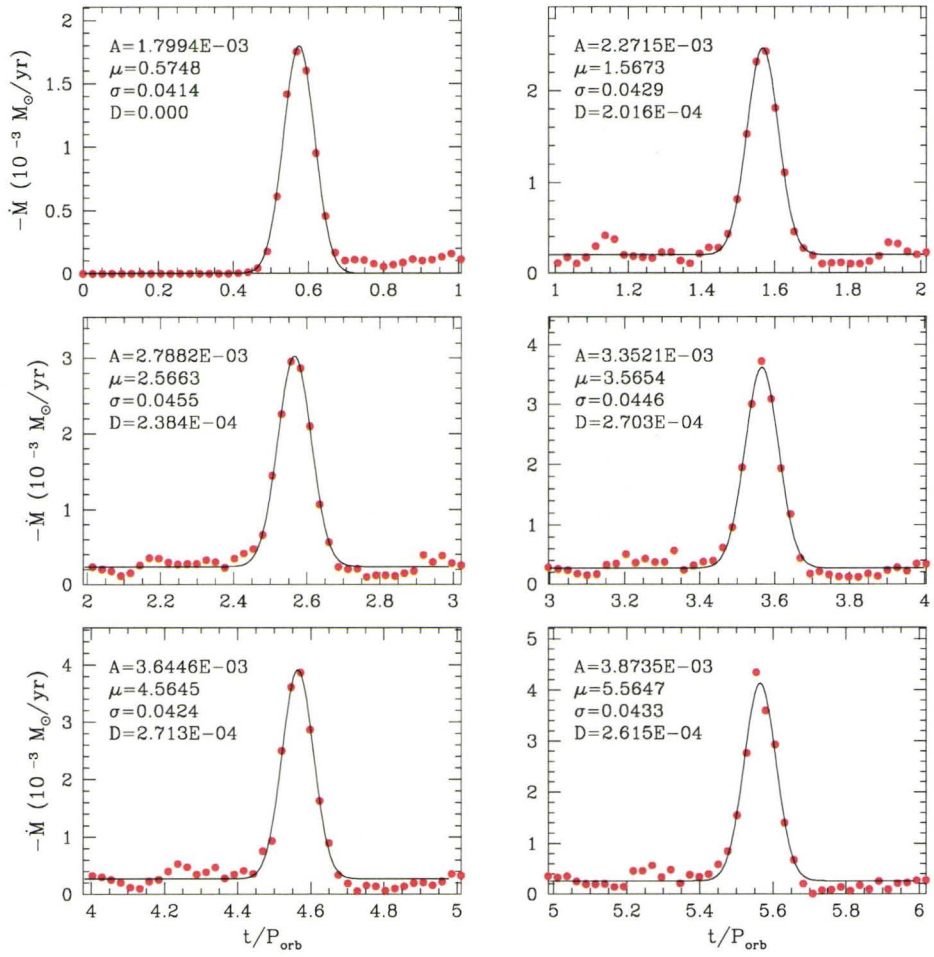

Figure 5.27 Same as Figure 5.24 but for the $e = 0.25$ case.

is in contrast with one of the basic assumptions of SWKR07 and SWKR09, who assumed that mass transfer occurred exactly at periastron. Although the results from our low-mass binary simulations are less suggestive however, the trend observed in the position of the maximum mass transfer rate suggest that since mass transfer occurs later than at periastron, the degree of overflow is also less than expected, thus making the mass transfer smaller. We also observe, from both sets of simulations, that the width (or duration) of the mass transfer episode is finite in time and arguably independent of the eccentricity.

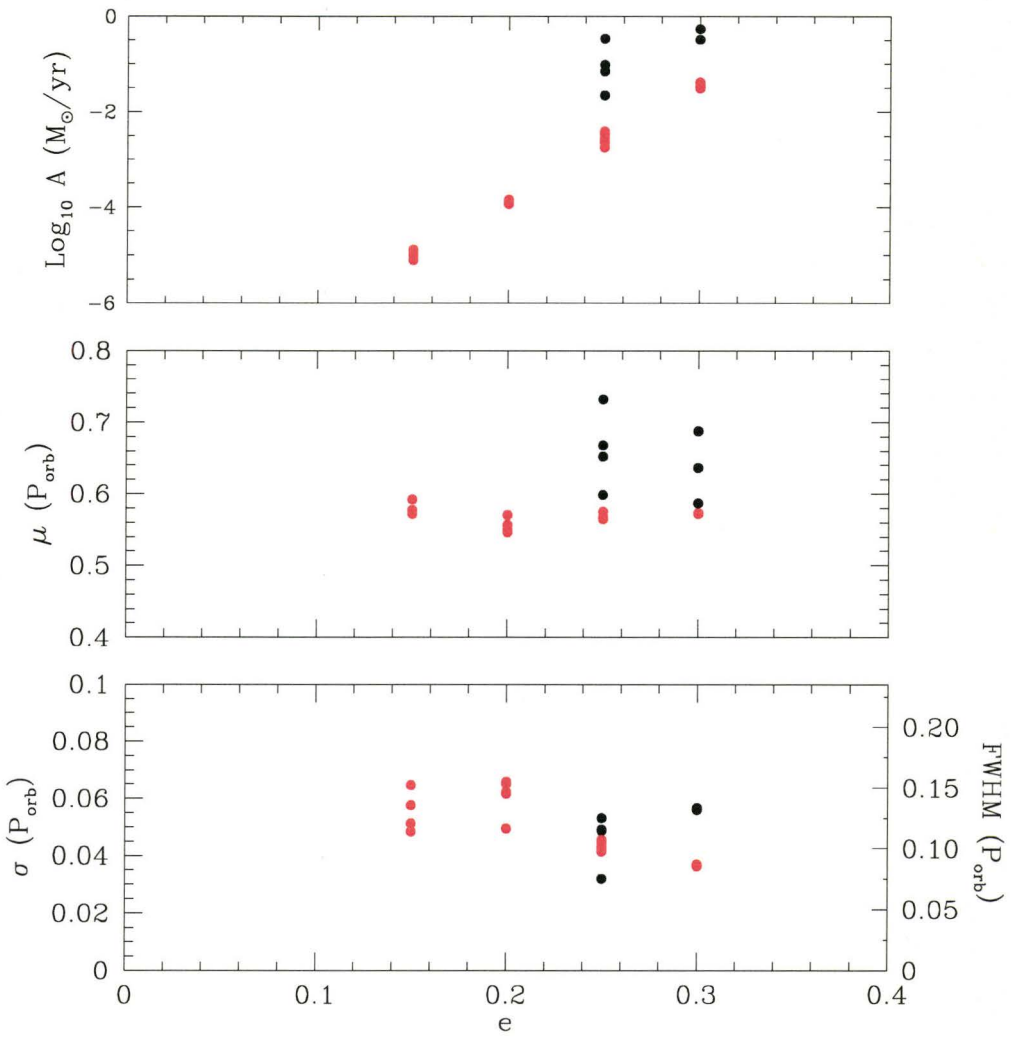

Figure 5.28 Amplitude, position, and width of the Gaussian fits to the mass transfer episode for the primary as a function of eccentricity for both binary systems. Black dots are for the $0.80 + 0.48$ $M_\odot$ binary while red dots are for the $1.50 + 1.40$ $M_\odot$ binary.

Our results suggest that the full width at half maximum (FWHM $\approx \sqrt{8 \ln 2}\sigma$) is approximately $0.10 - 0.13$ P_{orb}. One could argue that there is a small negative slope suggesting that the higher the eccentricity, the faster the mass transfer occurs, which would also make sense since stars on high eccentric orbits spend less time around periastron compared to star on low eccentric

orbits. No matter the trend here, this small difference in value of the width of the mass transfer rates is also in contrast with another basic assumption used by SWKR07 and SWKR09, who further assumed that the mass transfer rate was a delta function (peaked at periastron). Our results clearly show that this is not the case and the mass transfer rather occurs over an extended but finite period of time. From these results, we note that the work of SWKR07 and SWKR09 could be extended by incorporating delayed Gaussian mass transfer rates.

Finally, we note that the mass transfer rates observed in our simulations are substantial and that a binary system undergoing such large mass transfer rates is most likely going to merge, following a dynamical instability (e.g. D'Souza et al. 2006), or evolve onto a larger orbit and cease to transfer mass. It is therefore unlikely that such transient phenomena could be observed (Morton 1960), although the remnants of such past episodes of mass transfer might still be identifiable.

5.4 Accretion onto the secondary

Most of the mass lost by the primary eventually becomes bound to the secondary, as shown in Figures 5.17 and 5.18 where the accretion history of the secondary almost mirrors the mass transfer history of the primary. Another way to look at the accretion is to look at the origin of the particles making up each component. This is shown in Figures 5.29 and 5.31 where we plot the origin of the particles in the orbital plane and where red and blue dots are particles that were initially bound to the primary and to the secondary, respectively. This colour-coded representation allows us to track the particles

as they are shuffled around and become bound to any component of the system (i.e. the secondary, the binary envelope, or the ejecta). In the case of the low-mass binary, we see that the secondary is not strongly affected by the infalling material as none of its own particles are being mixed up with the material from the primary. As a matter of fact, the secondary is so dense that it is not perturbed at all by the mass transfer episodes and its accreted material simply forms an envelope around it. This can also be observed in Figure 5.30, where we used `SPLASH` to obtain a three-dimensional surface rendition of the $0.80 + 0.48$ $M_\odot$ system with $e = 0.25$. The surfaces are rendered by defining a critical surface through which we can not see, similar to what is known as the optical depth (τ). The larger the optical depth, the deeper we can peer through the stars' envelope. Choosing a very small optical depth renders the systems totally engulfed in very low density material and the stars are barely visible. Thus, in order to compare the densities involved, we choose an optical depth that allows us to see the initial surface of the primary. For comparison, we use optical depths of $\tau = 0.08$ for the low-mass binary and $\tau = 25.0$ for the high-mass binary. This large difference between the optical depths means that, in order to see the "surface" of the stars, we must peer through much more material in the high-mass binary case. Also, this three-dimensional rendition allows us to visualize the whole system at once, which is more insightful than using cross-section in the orbital plane. For example, Figure 5.30 shows that the material transferred from the primary initially forms a thick torus-like cloud around the secondary, and subsequent episodes of mass transfer eventually form an envelope that rather engulfs the secondary. Moreover, the primary also becomes engulfed by a rather thin envelope. Since the secondary does not lose any mass, this envelope around the primary is made up of its own

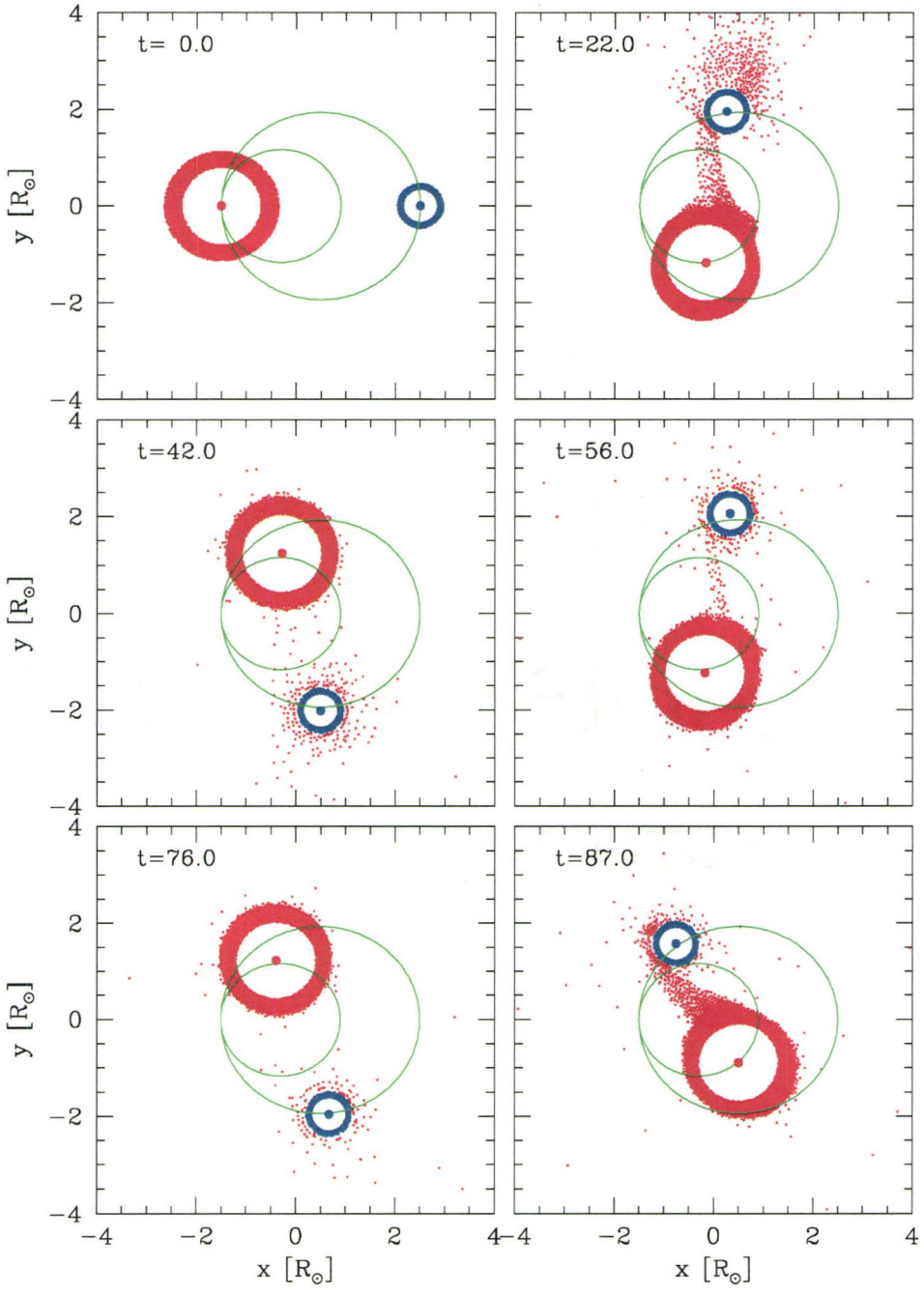

Figure 5.29 Origin of particles in the orbital plane for the 0.80+0.48 $M_\odot$ binary with $e = 0.25$. Red and blue dots are particles that initially come from the primary and secondary, respectively. In this case, the secondary is not affected by the infalling material.

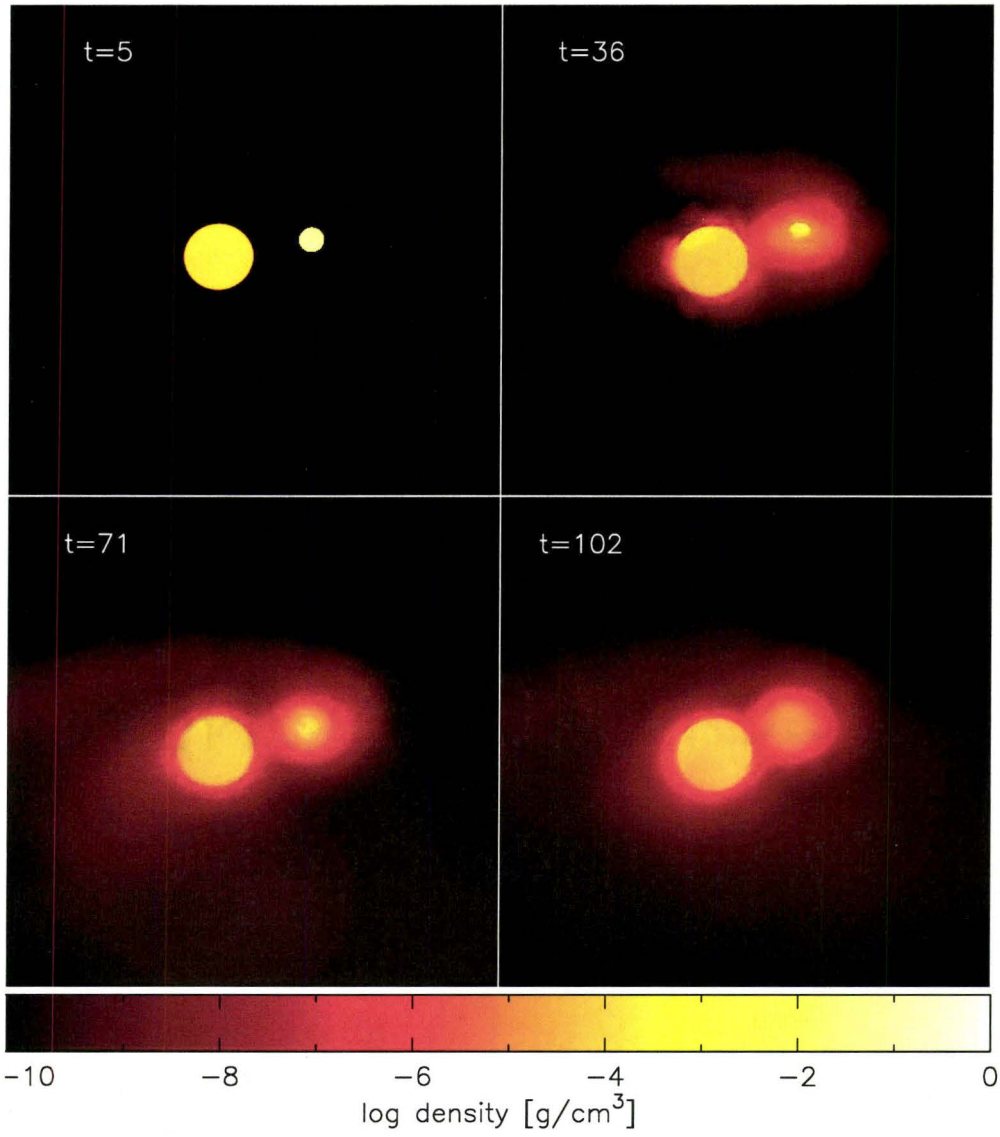

Figure 5.30 Surface rendition (with $\tau = 0.08$) of the density for the 0.80+0.48 $M_\odot$ binary with $e = 0.25$ showing the accretion around the secondary. Initially, a thick disk forms around the secondary, but later engulfs it almost completely. Mass loss occurs also primarily from the secondary's far side, at the L_2 point.

material. Actually, all of the material making up the accreted material around the secondary, the binary envelope, and the ejecta comes from the primary.

In the case of the high-mass binary, the similar densities of the two stars allows for the material being transferred to interact much more strongly

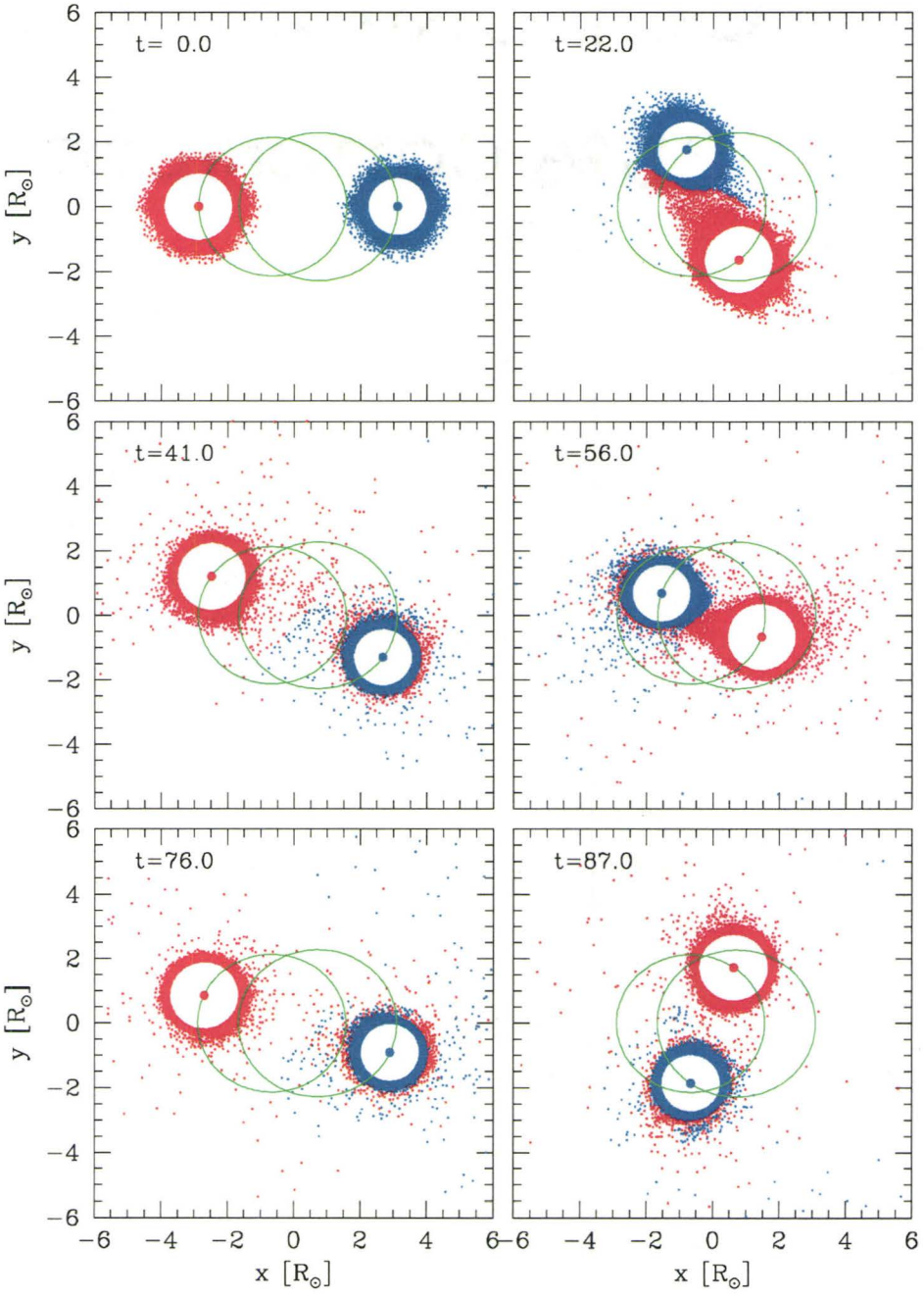

Figure 5.31 Origin of particles in the orbital plane for the 1.50+1.40 $M_\odot$ binary with $e = 0.30$. Red and blue dots are particles that initially come from the primary and secondary, respectively. In this case, the secondary loses material because of partial Roche lobe overflow and the interaction of the infalling material with its envelope.

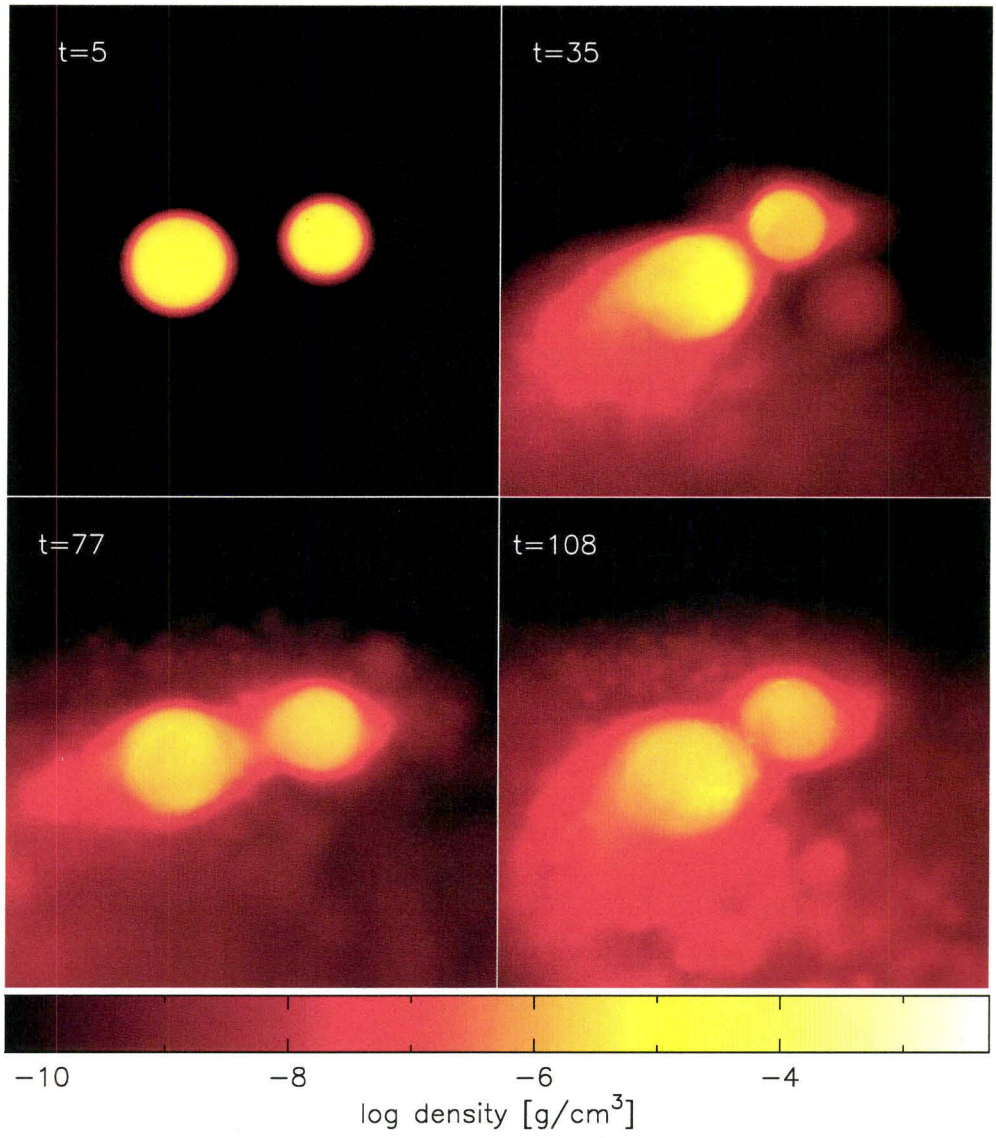

Figure 5.32 Surface rendition (with $\tau = 25.0$) of the density for the 1.50+1.40 $M_\odot$ binary with $e = 0.30$ showing the accretion around the secondary. In this case, an envelope engulfs both star and mass loss occurs also from both stars' far sides, at the L_2 and L_3 points

with he secondary's envelope, as shown in Figure 5.31 (for $e = 0.30$). Indeed, as shown by the red and blue dots, particles from the outermost layers of the secondary, as well as from the primary, are lost from both stars and scattered everywhere in the orbital plane. Although the secondary loses almost as many

particles than the primary, as previously shown in Figure 5.19, the total mass lost by the secondary actually remains relatively small ($\sim 5\%$ for the $e = 0.30$ and $\sim 10\%$ for the $e = 0.25$ case). Again, we emphasize that the fact that the secondary loses some mass is the result of both the secondary slightly overfilling its Roche lobe (see upper right panel of Figure 5.31 for example) and the interaction of the infalling material plowing through the envelope of the secondary. This is more analogous to a so-called "direct impact" where the secondary fills most of its Roche lobe and therefore is hit almost right after the transferred material passes the L_1 point. Interestingly, we do not observe such a mass loss from the secondary for smaller eccentricities (e.g. $e = 0.15$ and $e = 0.20$; see Figure 5.19), which agrees with the fact that only at (relatively) high eccentricity does the system come close to a contact configuration. As can be also seen in Figure 5.32, all of the material being lost from both stars eventually engulfs the whole system rather than forming an envelope around the secondary only. This envelope is substantially denser and thicker than in the low-mass binary case as the surface rendition of Figure 5.32 uses a much larger optical depth in order to peer through the envelope and see the surface of the stars. We observe the formation of such an envelope in all of our simulations for this binary, although the envelope for the $e = 015 - 0.20$ cases is thinner as less material is lost from either star.

As in the case of the mass transfer episodes, the accretion episodes also display similar positions and duration and characteristic shapes of Gaussian functions. Using the same approach as in §5.3.2.1, we show the Gaussian fits to the accretion episodes of the secondary for all of our simulations in Figures 5.33 to 5.38. Again, we use the same four parameters, namely the maximum accretion rate and its position, the width and the continuum level, and data

points represented with open circles are omitted from the fitting procedure to ensure that we are fitting correctly the accretion rates at periastron. First, Figures 5.33 to 5.38 clearly show that the mass accretion episodes can also be described accurately by Gaussian functions. Second, we note that the accretion history of the secondary is not as noisy as the primary's mass transfer episodes, especially after every periastron passage. Indeed, in all cases, the fit to the continuum of each Gaussian (D) is very close to zero, suggestive of an accretion that practically stops after every periastron passage (when neglecting data points obviously not representative of a Gaussian). These smoother profiles suggest the secondary does not accrete any mass either from the primary or the envelope. Third, we note that the position of the peaks and the width of the Gaussian are similar to the mass transfer episodes of the primary. We

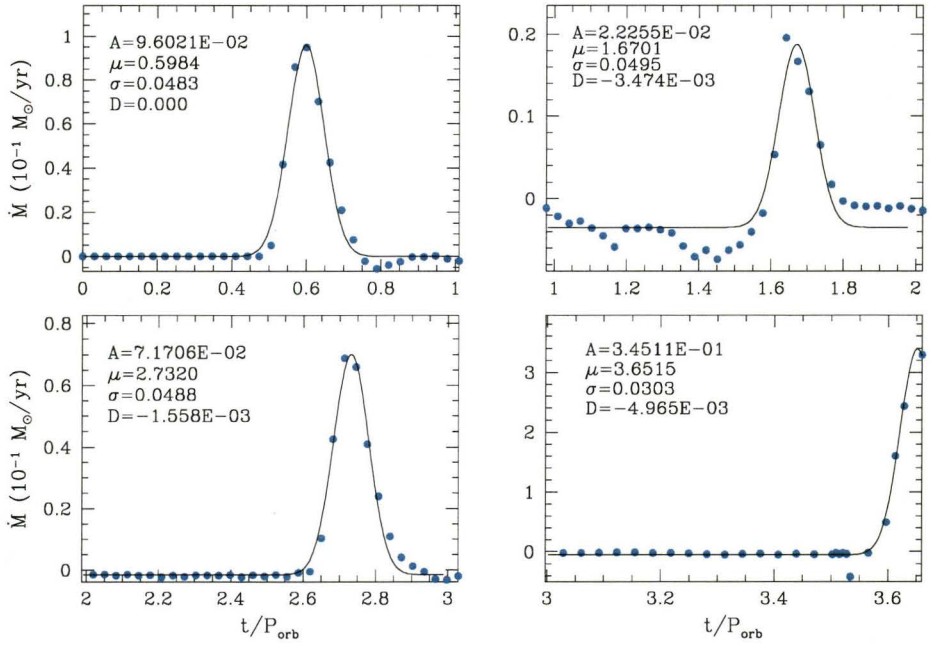

Figure 5.33 Gaussian fits to the secondary's mass accretion episodes for the 0.80+0.48 $M_\odot$ binary with $e = 0.25$.

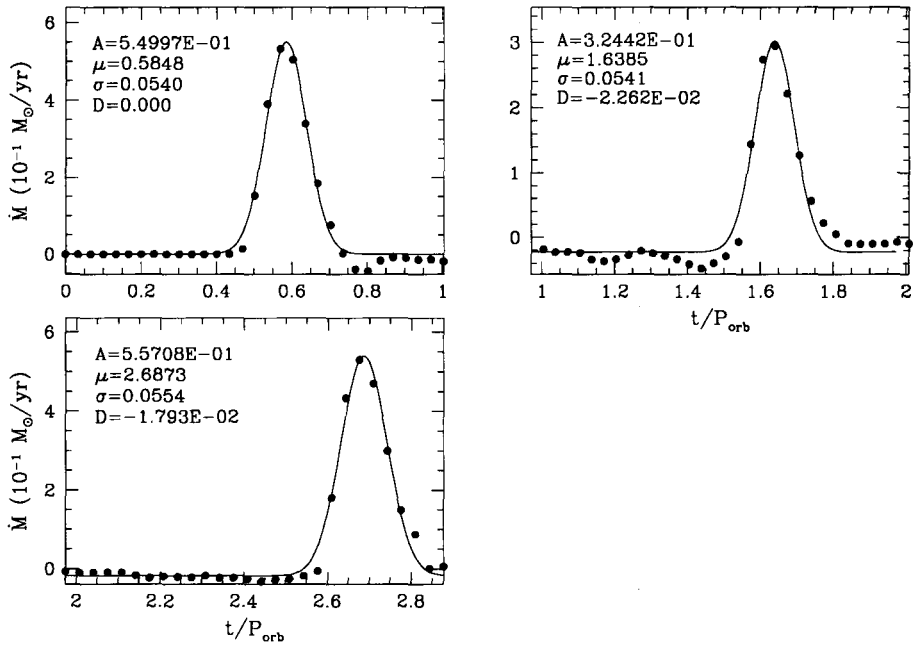

Figure 5.34 Same as Figure 5.33 but for the $e = 0.30$ case.

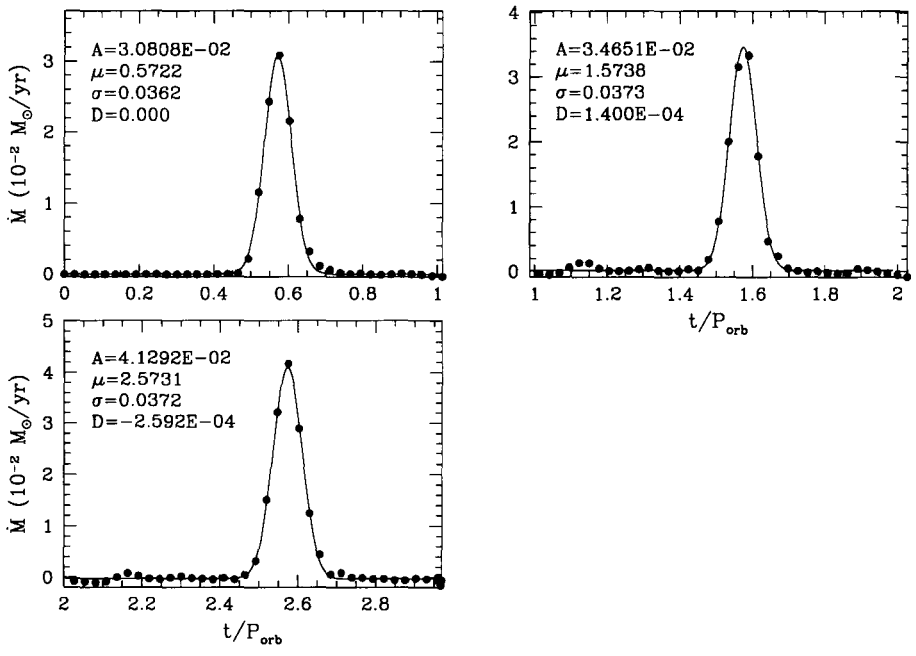

Figure 5.35 Gaussian fits to the secondary's mass accretion episodes for the 1.50+1.40 $M_\odot$ binary with $e = 0.30$.

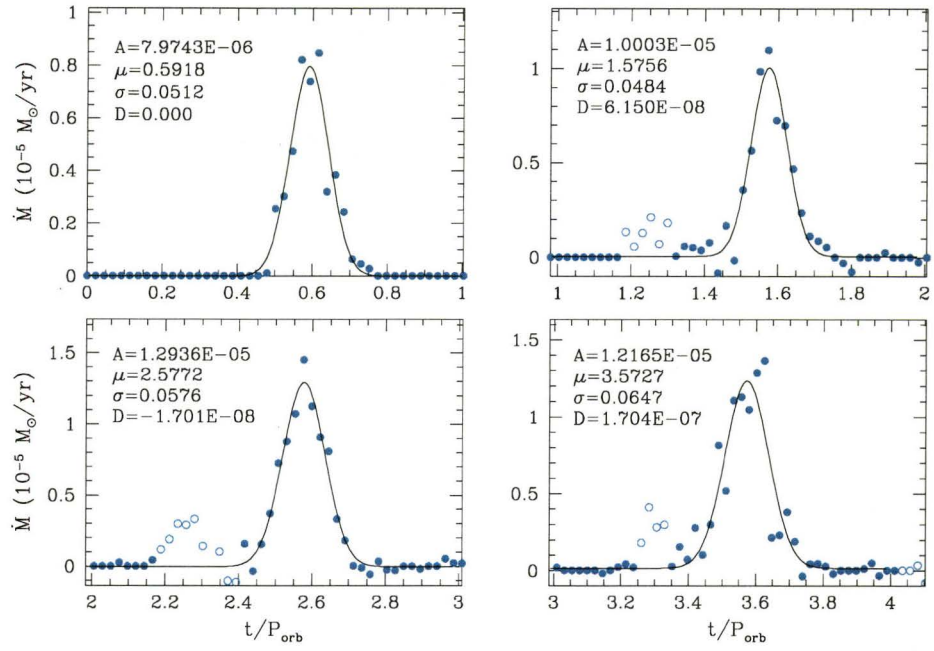

Figure 5.36 Same as Figure 5.35 but for the $e = 0.15$ case. Open circles are data points which are not taken into account when fitting the free parameters.

gather the results of our fits for all the orbits of all of our simulations in Figure 5.39. We find that the parameters follow the same trends as shown in Figure 5.28 for the primary's mass transfer rates, with only minor difference in the width of the Gaussians (σ). Indeed, we only notice a slightly larger spread in σ for the accretion rate when compared with the mass transfer rates. For further comparison, the parameters of the Gaussian fits for both the primary's mass transfer episodes and the secondary's accretion episodes for all our simulations are gathered in Table 5.1. Although we could expect the maximum mass transfer rate (A_1) to be larger than the maximum accretion rate (A_2), we see that it is not always the case. The reason is simply that the values of the continuum (parameter D) are different for the primary and the secondary, thus yielding a different zero level from which the peak values are

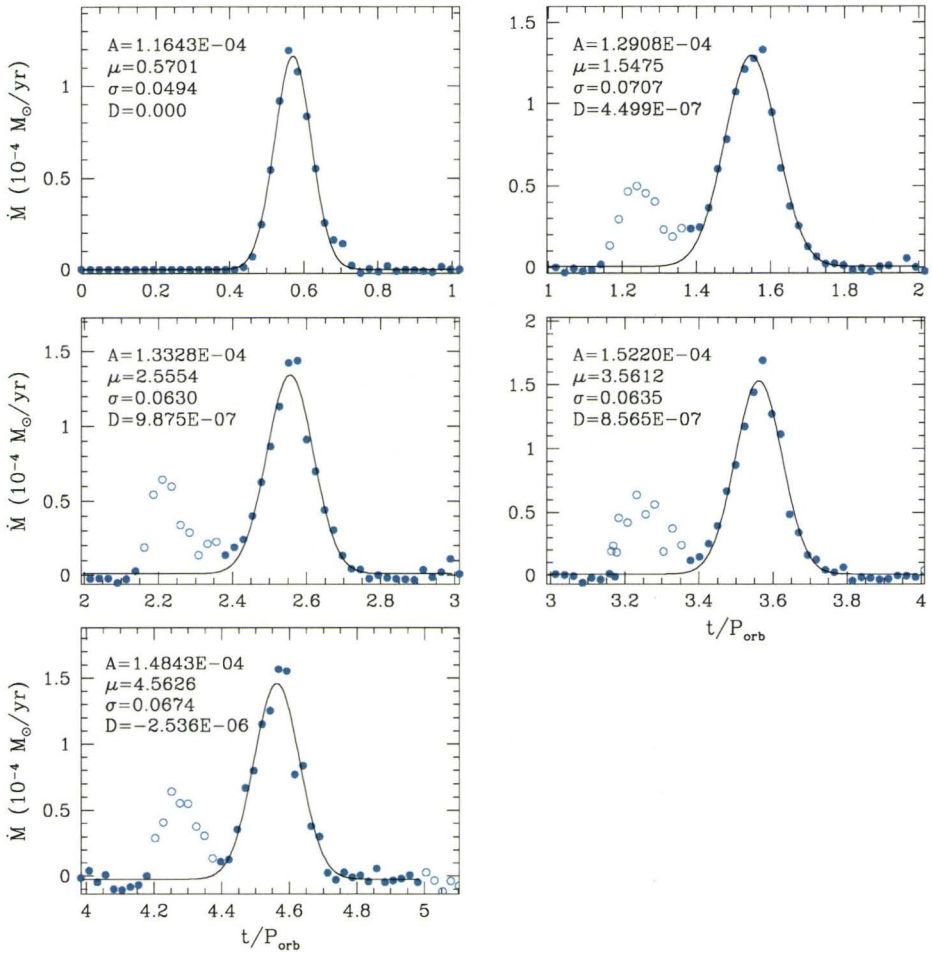

Figure 5.37 Same as Figure 5.36 but for the $e = 0.20$ case. Open circles are data points which are not taken into account when fitting the free parameters.

measured. In any case however, the total mass accreted by the secondary is always less (or equal) to the mass lost by the primary. The remaining mass is obviously lost to the binary as a whole or to the ejecta (see §5.5).

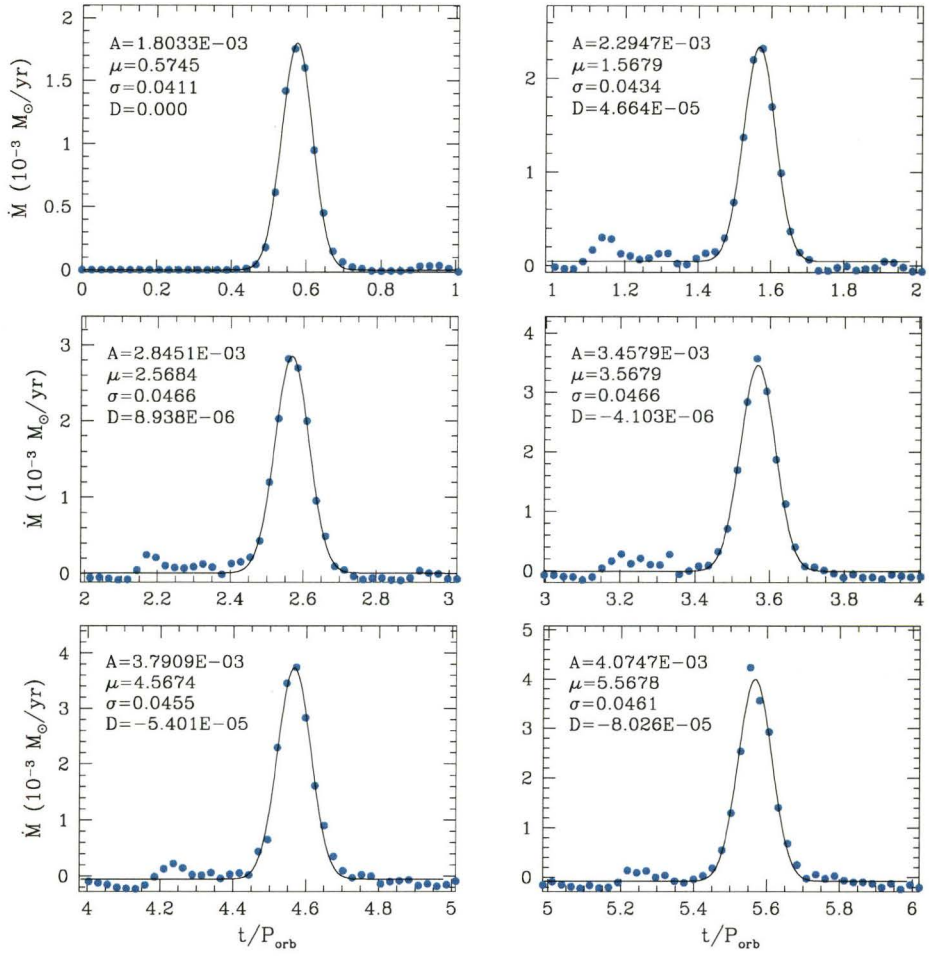

Figure 5.38 Same as Figure 5.36 but for the $e = 0.25$ case.

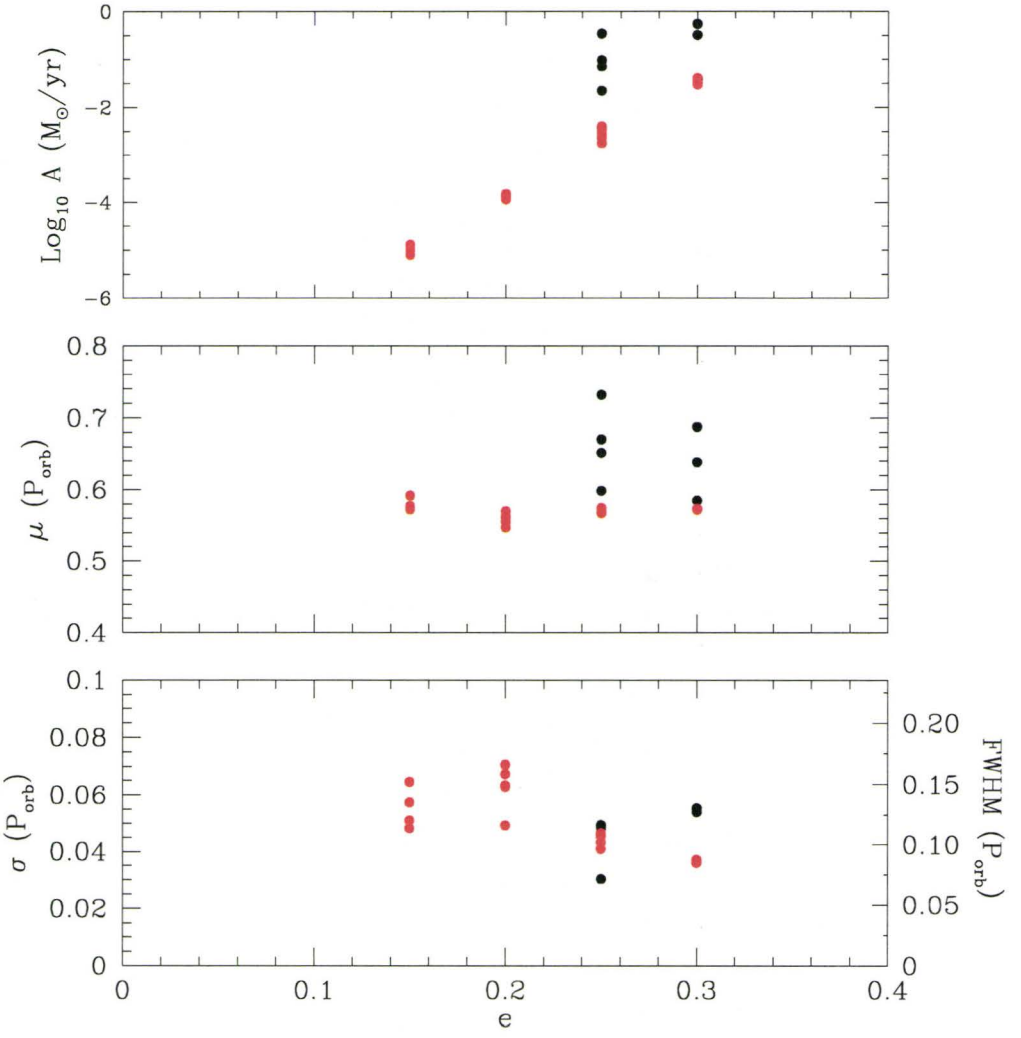

Figure 5.39 Amplitude, position, and width of the Gaussian fits to the mass accretion episode for the secondary as a function of eccentricity for both binary systems. Black dots are for the $0.80 + 0.48$ $M_\odot$ binary while red dots are for the $1.50 + 1.40$ $M_\odot$ binary.

Table 5.1. Summary of all Gaussian parameters for the primary's and secondary's mass transfer and accretion episodes

System	Ecc.	A_1 ($M_\odot$/yr)	A_2 ($M_\odot$/yr)	μ_1 (P_{orb})	μ_2 (P_{orb})	σ_1 (P_{orb})	σ_2 (P_{orb})
$0.80 + 0.48\ M_\odot$	0.25	9.61E-02	9.60E-02	0.60	0.60	0.049	0.048
		2.23E-02	2.23E-02	1.67	1.67	0.053	0.049
		7.06E-02	7.17E-02	2.73	2.73	0.049	0.049
		3.42E-01	3.45E-01	3.65	3.65	0.032	0.030
	0.30	5.53E-01	5.50E-01	0.59	0.58	0.056	0.054
		3.27E-01	3.24E-01	1.64	1.64	0.056	0.054
		5.48E-01	5.57E-01	2.69	2.69	0.057	0.055
$1.50 + 1.40\ M_\odot$	0.15	7.97E-06	7.97E-06	0.59	0.59	0.051	0.051
		1.00E-05	1.00E-05	1.58	1.58	0.048	0.048
		1.29E-05	1.29E-05	2.58	2.58	0.058	0.058
		1.22E-05	1.22E-05	3.57	3.57	0.065	0.065
	0.20	1.16E-04	1.16E-04	0.57	0.57	0.049	0.049
		1.22E-04	1.29E-04	1.55	1.55	0.066	0.071
		1.26E-04	1.33E-04	2.55	2.56	0.062	0.063
		1.44E-04	1.52E-04	3.56	3.56	0.062	0.064
		1.38E-04	1.48E-04	4.56	4.56	0.065	0.067
	0.25	1.80E-03	1.80E-03	0.57	0.57	0.041	0.041
		2.27E-03	2.29E-03	1.57	1.57	0.043	0.043
		2.79E-03	2.85E-03	2.57	2.57	0.045	0.047
		3.35E-03	3.46E-03	3.57	3.57	0.045	0.047
		3.64E-03	3.79E-03	4.56	4.57	0.042	0.045
		3.87E-03	4.07E-03	5.56	5.57	0.043	0.046
	0.30	3.10E-02	3.08E-02	0.57	0.57	0.036	0.036
		3.41E-02	3.47E-02	1.57	1.57	0.037	0.037
		4.05E-02	4.13E-02	2.57	2.57	0.037	0.037

5.5 Mass loss

In this section, we focus on the mass lost from the system, namely either to the binary envelope or the ejecta. As described above, particles are assigned to either of these two components if they are far enough from either stellar components and/or their total (relative) energy is positive. First, we discuss escaping particles and how the codes treats them, and then discuss some trends observed in our simulations.

5.5.1 Escaping particles

Escaping particles are particles that are found far (i.e. many smoothing lengths) from the bulk of the particles. By design, the code, and more specifically the tree building and the neighbours search, run into some problems when particles escape and/or are found in between the two stars, with only a few other close particles. Indeed, when particles are ejected from the system, the search for the required number of neighbours become lengthy and sometimes unsuccessful. To circumvent this issue, we set a maximum smoothing length ($\sim$5 $R_\odot$) such that the code does not spend too much time on adjusting the smoothing length of a small set of particles. These escaping particles lack sufficient neighbours, therefore breaking one of the SPH basic rules, but, as we shall show in §5.5.2, their low numbers and total mass are small and mostly likely do not affect the (hydro)dynamics of the mass transfer process itself. Likewise, for cases where only a handful of particles are found in between the two stars, the neighbours search can be problematic as increasing the smoothing length can encompass the surface of one of the stars and suddenly increase the number of neighbours to a (very) large number. In such cases, we force the smoothing

length to smaller values such that the number of neighbours is not too large. However, for simulations (e.g. Models 2 and 3) where only a few particles are transferred, these fixes can make the hydrodynamics less accurate, making the treatment more like a gravitational free-fall.

5.5.2 Binary envelope and ejecta

As discussed in Chapter 2, non-conservative mass transfer, although generally believed to be the norm, is difficult to constrain. In order to further assess the degree of mass loss from the mass transfer episodes in our simulations, we show, in Figure 5.40, the total mass bound to the binary envelope (green) and ejecta (magenta) for only the successful runs from both sets of simulations (this is a close-up view of Figures 5.17 and 5.18). The upper two panels are for the low-mass binaries whereas the lower four panels are for the high-mass binaries. The dotted line is the sum of both of these components. In all cases, the mass contained in the binary envelope is greater than that in the ejecta, by a factor of at least two. Both components grow as a function of time, and although no clear episodes of mass growth is observed for the ejecta, we find again a somewhat similar stepwise increase in the binary envelope bound mass. The total mass in each component ranges from a few 10^{-7} $M_{\odot}$ for the high-mass binary to $\sim 6\ 10^{-5}$ $M_{\odot}$ for the low-mass binary. This amounts to $\sim 0.1 - 1\%$ of the total initial mass (in SPH particles) of the primary. In all cases, the binary envelope and the ejecta are composed of at most $\sim 50,000$ particles, down to only a few tens of particles for the lowest eccentricity case (for the high-mass binary). This low number limits the ability to accurately model the hydrodynamics of this material, as discussed in the last section.

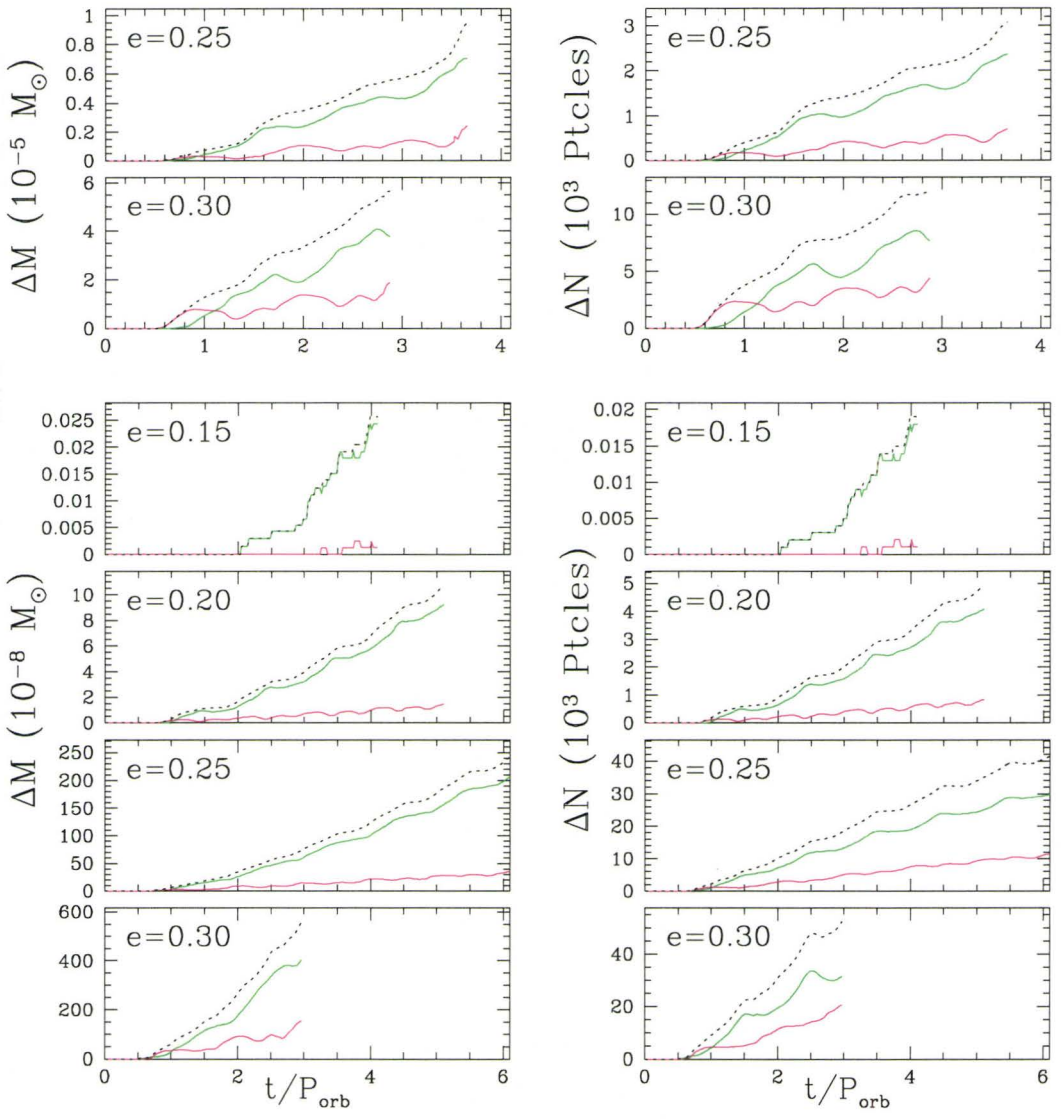

Figure 5.40 Mass (left) and particle (right) loss as a function of time and eccentricity for both the $0.80+0.48$ $M_\odot$ (upper two panels) and the $1.50+1.40$ $M_\odot$ (lower four panels) binaries . The green line shows the mass bound to the binary as a whole and the magenta line is the ejecta.

Figure 5.41 shows the change in bound mass of the binary envelope and the ejecta normalized by the change in mass of the primary. Essentially, this shows the fraction of mass lost by the primary that ends up in the binary envelope or the ejecta. Interestingly, the fraction of mass bound to the binary

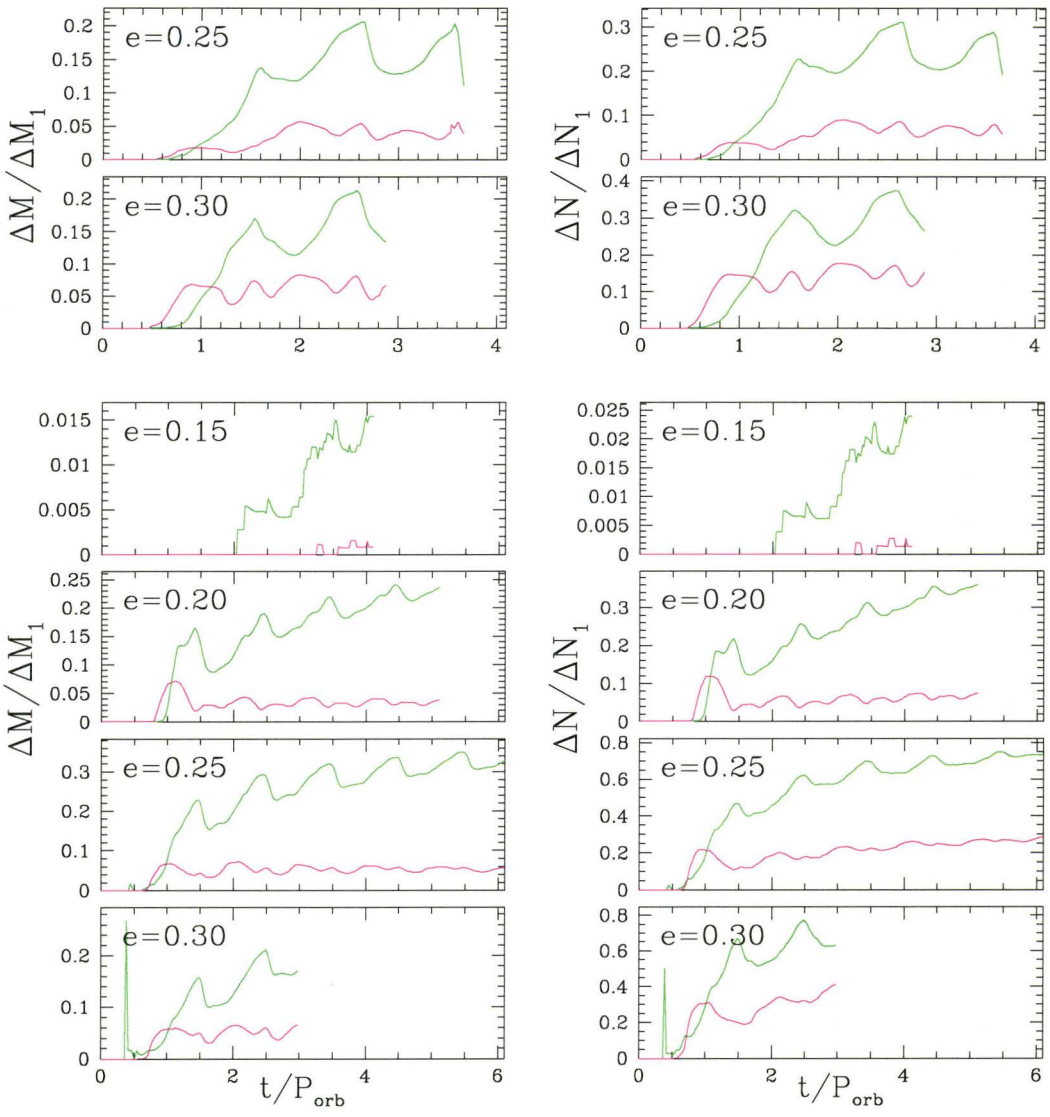

Figure 5.41 Changes in mass in the common envelope and ejecta normalized by the change in mass of the primary for both the $0.80 + 0.48$ $M_\odot$ (upper two panels) and the $1.50 + 1.40$ $M_\odot$ (lower four panels) binaries.

envelope shows some periodic behaviour, peaking shortly *before* periastron, where the stars are at their closest separation along the orbit. This lag comes from the fact that (some of the) infalling material only temporarily becomes bound to the secondary before becoming bound to the envelope or the ejecta. By the end of our simulations, around 20% of the mass lost by the primary

end up in the binary envelope, and our results suggest that this fraction slowly increases as a function of time.

The mass in the ejecta, on the other hand, is roughly constant around 5% for all of our simulations. This is an unexpected result, given that we observe this trend in all of our simulations, no matter the mass of the stars or the eccentricity. Moreover, given that the degree of mass loss in binary evolution is rather unconstrained (e.g. SWKR09), this result is suggestive of a rather uniform mass loss over different binary masses. Although conservative mass transfer is usually accepted to be an idealized case, the constant and small fraction of mass lost from the system suggests that mass transfer is indeed non-conservative but only to a small degree. This is also interesting in the context of two (slightly) different accretion scenarios, where accretion occurs via an accretion disk or through a direct impact. In the latter case, when the secondary fills a significant fraction of its Roche lobe, the matter falling in from the L_1 point hits the accretor almost directly, whereas in the former case, material falls deep in the potential well of the secondary and forms a disk. Although the direct impact scenario is more representative of our high-mass binary rather than the low-mass binary, and whether or not the infalling material interacts with the secondary's envelope, we still get that roughly 5% of the mass lost by the primary ends up in the ejecta. Note, however, that our simulations do not allow us to assess the fate of the binary envelope. i.e. whether it is going to be expelled from the system and become part of the ejecta or be accreted by either stars. This result may have implications for binary population synthesis studies as well as N-body calculations of binary populations.

5.6 Comparisons with previous work

In light of the results presented in §§5.3, 5.4, and 5.5, we can now compare our work to previous work and discuss the improvements made in the understanding of episodic mass transfer in eccentric binaries. First, similarly to Church et al. (2009), our results show that the closer the stars are at periastron, the larger the mass transfer rates. Moreover, we have also showed that the mass transfer episodes occur not exactly at periastron and last for a small fraction of the orbital period. In particular, our work shows that these episodes of mass transfer all last for a constant fraction of the orbital period, independent of the eccentricity. However, unlike Church et al. (2009), our mass resolution does not allow us to resolve mass transfer rates as low as $\sim 10^{-10} - 10^{-9}$ $M_{\odot}$ yr^{-1}. For low-eccentricity binaries, this would most likely increase the number of particles in the stream of material and better model the flow, but we do not think that this would drastically change our conclusions.

Our binaries are set up such that they are in corotation at apastron, therefore making them subsynchronous at periastron as the orbital velocity at periastron is larger than at apastron. In both of our sets of simulations, the ratio of the angular velocity, which is fixed for the whole duration of the simulations, to the orbital velocity at periastron ranges from around 0.30 to 0.60. Thus, according to Sepinsky et al. (2007a) (see also Figure 2.6), this has the effect of slightly increasing the Roche lobe radius, by $\sim 5\%$, when compared to the instantaneous Roche lobe radius at periastron. An increase in the Roche lobe radius would therefore effectively decrease the degree of overflow and, consequently, the mass transfer rate. Comparing the magnitude of the mass transfer rate observed in our simulations with theoretical expectations is

difficult because estimating the actual radius of the primary is rather uncertain. However, using equation 2.10 (see also Paczyński & Sienkiewicz 1972 and Edwards & Pringle 1987; note that these rates are for an $n = 3/2$ polytrope), we build a simple model for the mass transfer rate using the instantaneous Roche lobe radius, which is a generalization of equation 2.4:

$$R_L^{inst.} = D(t)\frac{0.49q_1^{2/3}}{0.6q_1^{2/3} + \ln(1 + q_1^{1/3})}, \tag{5.5}$$

$D(t)$ is the instantaneous separation of the two stars. Thus, assuming a radius for the primary star, which should not change much over the course of our simulations since the total mass involved is small, we can calculate an instantaneous degree of overflow, $\Delta R = (R - R_L^{inst.})$, based on the instantaneous separation of the stars, and a mass transfer rate. This is shown in Figure 5.42 for the high-mass binary with $e = 0.25$, along with the functional dependence of the mass transfer rate on the degree of overflow. The latter shows that the mass transfer rate increases rapidly over small changes in the degree of overflow and that it is identically zero when the primary is within its Roche lobe, as expected. Also, note that we have arbitrarily set the canonical mass transfer rate ($\dot{M}_0$; see Equation 2.10) such that the first peak of mass transfer matches that from our simulation. Moreover, to mimic the slightly expanding envelope of the primary, as can be observed in our simulations, we assume that the radius of the star increases at each orbit, by increments of 0.05 $R_\odot$. This large change in radius is arbitrarily chosen to better match the gradually increasing peak mass transfer rates over time and may not be adequate. We note that determining the radius of the primary at this point is difficult as it is surrounded by an envelope and that some of this envelope

is transferred during periastron passages. However, our results show that the peak mass transfer does not keep increasing steadily. The surface of the star is poorly defined from our simulations, but given the relatively small amount of mass transferred in our simulations, we do not expect a large change in radius over the course of our simulations. The difficulty in doing such a comparison *with eccentric orbits* lies in the fact that (1) we are using the instantaneous Roche lobe radius derived for circular and synchronous binaries and (2) the theoretical mass transfer rate used here was derived for polytropes of constant n. Although this simple model agrees qualitatively well with our simulations (e.g. Gaussian-like episodes of mass transfer), we emphasize that we arbitrarily fixed the canonical mass transfer rate so that the peaks match. However, independent of the assumed canonical mass transfer rate, we observe that the position and width of the mass transfer episode strikingly differ from the theoretical expectation. The width of the peak depends on the star's radius, since decreasing it will only delay the start of mass transfer, although doing so not only delays the onset of mass transfer but also decrease the degree of overflow. Therefore, mass transfer is less, as expected, and the match with the results from our simulations is not as good. Therefore, it is hard the change the width of the mass transfer episodes while keeping the same peak value. On the other hand, there is no parameter that could account for the position of the maximum rates as, by construction, the largest degree of overflow occurs when the stars are closest to each other, i.e. at periastron.

The fact that the mass transfer (and accretion) rate in eccentric binaries has a functional form well fitted by a Gaussian is one major finding that could be used to extend the work of SWKR07 and SWKR09. In addition, although the delayed onset of mass transfer has been recognized and discussed by Regös

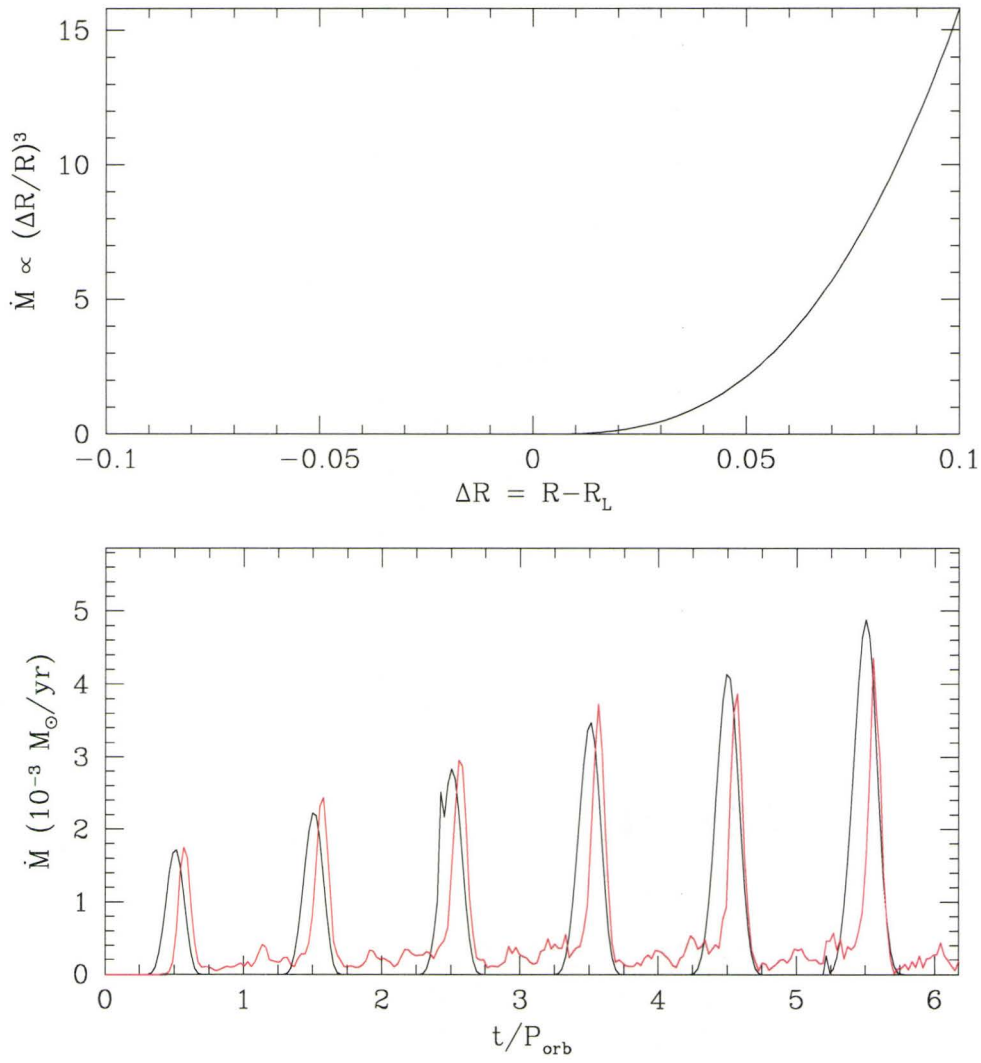

Figure 5.42 *Top*: Functional dependence of the mass transfer rate on the degree of overflow of equation 2.10. The units are arbitrary. *Bottom*: Comparison between the instantaneous mass transfer rate of equation 2.10 (black) and our results (red) for the the $1.50 + 1.40$ $M_\odot$ binary with $e = 0.25$. Note that we have arbitrarily fixed the canonical mass transfer rate ($\dot{M}_0$) so that the first mass transfer peaks coincide and that the radius of the primary is increased during each orbit by increments of 0.05 $R_\odot$ such that after 6 orbits, the radius is 2.10 $R_\odot$.

et al. (2005) and Church et al. (2009), our work has allowed us to quantify this lag. Our results allow us to further constrain the shape of the Gaussian to a

typical FWHM of $\sim 0.10 - 0.15$, starting right after periastron. SWKR07 and SWKR09 also assumed a constant mass transfer rate, but our simulations show that the maximum mass transfer rate seems to increase with time, although we do not have a large number of orbits to verify the longer-term behaviour. Finally, we have shown that mass loss does occur, as usually assumed, and have been able to show that it is relatively small, although the long-term fate of the binary envelope is uncertain.

5.7 Limitations of our method

The hydrodynamical modeling of mass transfer in binaries is a hard task for many reasons, some numerical and some physical (see Chapter 2). In this thesis, we introduced a new technique using boundary conditions to circumvent some of them and showed that by doing so, we can get better insight into the physics of mass transfer. The physicality of our simulations of course depends on the physical ingredients we put in. As such, we do not include effects such as radiation pressure or energy transport mechanisms by radiation or convection. These effects may have significance especially when studying the long-term evolution of the thin envelope, where radiative cooling might be most efficient, but we do not think that our results for the episodes of mass transfer would be affected by their inclusion. Likewise, as noted in the last column of Tables 4.1 and 4.2, the code and/or the boundary conditions fail to correctly model mass transfer under extreme circumstances. We now discuss some of these limitations in more details.

5.7.1 Solid boundary

The main limitation of our method is the boundary treatment. First, the boundary is "solid", and its structure does not change if the gravitational potential changes. Although the work of Deupree & Karakas (2005) showed that only the outer parts of the stars are affected by the presence of a companion, the fact that the tidal force changes along an eccentric orbit should modify (slightly) the inner structure. To do so would require that we calculate the net force on the ghosts and evolve them in time, which would use more CPU time. Second, the boundary is "impermeable", i.e. that particles are not allowed to go through the boundary. Some of our simulations show that this does in fact occur when the mass transfer rates are large and the code is not built to deal with particles wandering inside the boundary, around the central point mass. This limits our ability to adequately follow some systems for many more orbits. On the other hand, when the mass transfer rates are very large, particles rush onto the secondary and, despite all the precautions taken to prevent penetration of the boundary, move right through the boundary and wander around the central point mass. At this point, the code can not correctly build the tree and find neighbours, and we have to stop the code. The runs for which either of these problems occurred are also noted in Tables 4.1 and 4.2.

5.7.2 Mass resolution

For cases where only a few particle are transferred from one star to the other, the code can not find enough neighbours. Indeed, the code searches for neighbours by iteratively increasing (or decreasing) the smoothing lengths until the particle's volume encloses a number of neighbours that is within a fixed range.

However, when the volume of the particle gets large enough to enclose part of the surface of either stars, the number of neighbours becomes large very quickly. When this occurs, the code thus reacts by decreasing the smoothing length, but then the number of neighbours becomes too small again, and the code enters an (almost) infinite loop. At this point, we have to stop our code. This characteristic of our code therefore limits the minimum mass transfer rate that can be resolved given the particle masses. Simulations during which our code ran into infinite loops because of a low number of particles are noted in Tables 4.1 and 4.2.

As discussed in §5.6, the mass resolution in our simulations is a few orders of magnitude larger than the work presented in Regös et al. (2005), although not quite as high as that of Church et al. (2009). Having particles of lower mass allows for a better description of low mass transfer rates as more particles will be transferred from one star to the other. This could resolve the problem we encountered in our low-eccentricity cases (i.e. e=0.10−0.20) where only a handful of particles were transferred. On the other hand, the caveat of increasing the mass resolution is that the number of particles gets very large and the CPU time increases accordingly. Therefore, one must compromise on the mass resolution and CPU time.

5.7.3 Equation of state

The equation of state we used in this work is that of a perfect gas. Such an equation of state does not reproduce the different behaviours of stars of different mass upon mass transfer, as discussed in 2. Indeed, stars less massive than $\sim 0.8-0.9$ $M_\odot$ have convective envelope that expand upon mass transfer

whereas more massive stars have radiative envelope that shrink upon mass transfer, and our equation of state can not reproduce these behaviours. Moreover, the presence of a solid boundary also limits the ability of the stars to readjust their structure (and radius) consistently across the whole star. However, given that the total mass in SPH particles is less than $\sim 1\%$ of the total mass of every star we model in this thesis, we do not expect a large (positive or negative) change in the star's radius. Therefore, we do not think that using a different equation of state would change our results and conclusion drastically.

5.8 Summary

In this chapter, we presented the results of our SPH simulations on mass transfer in binary systems of different masses and eccentricity. In particular, the relatively high spatial and mass resolutions achieved with our new technique allowed us to characterize the mass transfer process. We found that mass transfer episodes, as well as accretion episodes, are well represented by Gaussian functions with a FWHM of $\sim 0.12 - 0.13$ P_{orb} centered at an orbital phase of ~ 0.55. These findings apply to all our binaries, independent of the eccentricity, and represent a major improvement upon previous hydrodynamical simulations of similar systems. We also suggested that our results could be used in analytical work, such as that of SWKR07 and SWKR09, and binary population synthesis studies to better and further constrain the evolution of eccentric binaries.

Chapter 6

Conclusion

In this last chapter, we summarize the work presented in this thesis and discuss its implications and future potential. This work was motivated by the need for a better understanding of the onset and features of mass transfer in eccentric binaries for which no full theoretical prescriptions have yet been derived.

6.1 Summary

The evolution of binary stars has grown into an intense field of study since it has become clear that many populations of stars have to form through interactions with close stellar companions. Although the main phases of binary evolution are nowadays well understood, these evolutionary paths usually rely on the (idealized) formalism derived for *circular* and *synchronized* orbits. This so-called Roche lobe formalism does not apply for close and interacting *eccentric* binaries in which the rotation is asynchronous and the gravitational potential time-dependent. Given the relatively large number of binary stars,

and in particular, of binary stars with eccentric orbits, it is imperative to better understand the interactions of these systems in order to further constrain the different galactic populations of exotic stars. Recent breakthroughs by Sepinsky et al. (2007a), SWKR07 and SWKR09, in particular, have allowed us to extend our knowledge of the long-term evolution of eccentric binaries. Their analytical work has shown that the Roche lobe radius of eccentric binaries can differ significantly from the usually assumed circular case and that tidal interactions do not always lead to rapid circularization and synchronization. Although the results of Sepinsky et al. (2007a), SWKR07 and SWKR09 clearly show that eccentric binaries behave differently from circular ones, their conclusions are based on a number of assumptions. For example, since the Roche formalism does not apply for eccentric binaries, it is difficult to determine the mass transfer rate since it depends on the Roche lobe radius. We therefore need to rely on a different technique to relax these assumptions and this is the task we have undertaken in this thesis.

Analytical approaches for the evolution of binaries usually rely on prescriptions or approximations when dealing with mass transfer. To physically model mass transfer in detail, we have to use a different technique. In Chapter 3, we introduced our Smoothed Particle Hydrodynamics code along with some improvements that we have performed on it to specifically model mass transfer in binary stars. In particular, since the presence of a companion only affects the outermost layers of a star (e.g. Deupree & Karakas 2005), we introduced a novel way of implementing boundary conditions that allows us to model only the outer envelope of stars with high spatial and mass resolutions. Our new technique was shown to conserve energy, to be well suited for the modeling of stars, and to be up to $\sim 50\%$ faster than a fully modeled stars simulation (for

a given spatial resolution). Although our SPH code does not allow us to follow stars over long timescales (i.e. for longer than $\sim 10^3 - 10^4$ years), it allows us to better understand the physics of dynamical mass transfer and this is what we intended to use our new method for.

But first, we devoted Chapter 4 to the setup of proper initial conditions for modeling binary stars. The fine balance between the gravitational and hydrodynamical forces in binary stars requires that great care be taken when preparing the stars. Our binary relaxation procedure makes use of a non-inertial rotating reference frame to properly account for the tidal pull on each star from their companion, along with the centrifugal acceleration. We demonstrated that our initial conditions are consistently implemented in our relaxation procedure and that they allow us to evolve for many orbits detached circular binaries and maintain their orbital separation to within $1 - 2\%$. It was also shown that our boundary conditions behave well under such test simulations. Finally, we discussed the two particular binary systems that we use for our full-scale simulations presented in Chapter 5.

The results of our large-scale simulations are interesting both for the performances of our novel approach and for the characterization of the mass transfer episodes. First, we showed that our boundary conditions can effectively handle intermediate mass transfer rates ($\sim 10^{-6} - 10^{-4}$ $M_\odot$ yr^{-1}). Indeed, on the one hand, penetration of the boundary by particles occurs when the rates become too large; the infalling material simply rushes through the boundary and the code can not recover. On the other hand, our code, by design, does not handle cases where only a handful of particles are transferred. Second, for our successful simulations where mass transfer was resolved and followed for a number of orbits, the mass transfer episodes show clear trends.

In particular, we show that these episodes can be described by Gaussians with a FWMH of $\sim 0.12 - 0.15$ P_{orb}, and the peak mass transfer rates occur after periastron, around an orbital phase of $\sim 0.55 - 0.56$. It is interesting to note that these results apply for both binary systems modeled and for any eccentricity. These results represent a major improvement upon previous work as our new technique allows us to resolve and characterize the mass transfer episodes. For example, the early simulations of Edwards & Pringle (1987) modeled only a small volume around the L_1 point and did not encompass the whole process of mass transfer and accretion, whereas Regös et al. (2005) and Church et al. (2009) used a relatively low number of particles to study the onset of mass transfer in eccentric binaries. Interestingly, the technique of Church et al. (2009) allows for the resolution of mass transfer rates of the order of $\sim 10^{-8} - 10^{-9}$ $M_\odot$ yr^{-1}, a few orders of magnitude lower than our mass resolution, which they successfully applied to the modeling of cataclysmic variables. We also note that the results presented in this thesis could be implemented in analytical work such as that of SWKR07 and SWKR09 to further constrain the evolution of eccentric binaries. We also discussed the accretion onto the secondary and showed that it is also well characterized by similar Gaussians. The accreted material is observed to form a rather sparse envelope around the secondary, in the low-mass binary, and around both stars, in the high-mass binary. Although the fate of this envelope is not determined using our method (i.e. whether it is going to be accreted by either stars or ejected from the system), we showed that a constant fraction of the material lost by the primary is ejected from the systems. The concept of non-conservative mass transfer is generally accepted nowadays. However, it is poorly constrained and our results may help putting further constraints on the degree of mass

conservation in binary evolution.

6.2 Future work

The parameter space for the simulation of mass transfer in binary systems is rather large and in order to get a better picture of the mass transfer process in eccentric binaries, it is necessary to cover more of this parameter space. Moreover, in order to better model binary systems for a larger number of orbits (so that we eventually reach a steady-state regime) improvements remain to be done on our code, in particular on our treatment of boundary conditions.

6.2.1 Improvements to the code

6.2.1.1 Permeable and solid boundary

Although our simulations produced important results, as discussed above, the main limitation of our new approach for modeling boundary conditions resides in the fact that the boundary is not "impermeable" to particles. In some of our simulations, particles cross the boundary and the code can hardly deal with such a situation. As a matter of fact, we do not think that our boundary should be so particle-tight since we expect some mixing between the infalling material and the (deeper) envelope of the secondaries. Although moving the boundary to a smaller radius would easily fix this issue, it would counter the use and benefits of our new approach. Instead, we suggest that the use of sink particles at the centre of the stars could be implemented. Sink particles are just like point masses except that their mass (and momentum) are allowed to increase as SPH particles get absorbed by it. Such an improvement would

allow the code to handle relatively large mass transfer, which was the main reason of the early ending of some of our simulations, and evolve our binaries for much longer. Although mixing is hardly resolved in our simulations (we probably observe deep penetration rather than actual mixing), it is actually thought to be an important feature in the binary formation scenario of blue stragglers whose cores have somehow been replenished with fresh hydrogen. The use of sink particles could help further clarify this scenario.

Likewise, as discussed in §5.7, our boundary is solid and does not change its shape or provide a time-variable pressure gradient on the SPH particles. As a first approximation, this is a valid treatment (e.g. Deupree & Karakas (2005). However, when the gravitational potential changes significantly along the orbit, like on eccentric orbits, the solid boundary may not be adequate. Such an improvement would involve calculating the actual gravitational force on the ghosts, which is not done as of now, and would therefore require more CPU time. Similarly, we note that the angular velocity of the ghost particles is maintained fixed during our simulations. This is a valid assumption as synchronization occurs over timescales much longer than the whole duration of any of our simulations. However, we think that it would be more physical to drive the angular velocity of the ghosts consistently by ensuring that the angular momentum between the SPH particles and the ghosts is conserved. Although we have not undertaken any work on improving the treatment of "softer" boundaries, we think that both of these "upgrades" would greatly improve the validity of our method.

6.2.1.2 Binary relaxation for unequal-mass binaries

Our relaxation procedure for binary stars has proven to be especially efficient for equal-mass binaries. However, for unequal-mass binaries, we have hardly been able to achieve similar accuracy in the orbital separation. As discussed in §4.3, we suspect the reason for this behaviour to be either in our gravitational force calculation routine or in the use of individual timesteps. We have tried different approaches for the latter but have not yet found any ways to improve it. As for the gravitational force calculation, we found that using an `N-body` approach (i.e. using smaller opening angles; see Chapter 3) improves our results, although doing so also makes running our simulations significantly longer.

6.2.2 Impacts on previous work

Our simulations allowed us to assess the validity of our new boundary condition treatment, which can be applied to the study of many other different types of stars. For example, wind accretion is one common way for stars to accrete from a relatively distant companion and a few different populations of stars are thought to have been formed this way (e.g. barium and carbon stars). We suggest that our technique is versatile enough and that it can be used to model such systems and improve upon previous work (e.g. Theuns et al. 1996).

Likewise, our simulations allowed us to characterize the mass transfer episodes in eccentric orbits which, we suggest, can be used to further refine the work of SWKR07 and SWKR09. Indeed, these authors used a delta function centered at periastron (i.e. mass transfer occurs instantly and at only one point along the orbit) to represent the mass transfer in eccentric binaries. The

fact that these episodes are actually better represented by Gaussian functions with an almost constant FWHM of $\sim 0.12 - 0.15$ P_{orb} would arguably modify the total mass exchanged during each periastron passage and change the secular evolution of binaries. The implementation of the results of SWKR07 and SWKR09, along with the results presented in this thesis, in binary population synthesis codes could also arguably change the overall picture of some binary populations, especially in dense stellar environments where encounters and captures most likely lead to the formation of eccentric binaries. Such refinements to the existing theory of eccentric binaries would represent a step towards a more realistic theory of binary stars. Likewise, a better understanding of the evolution of such binaries would also help shed some light on the formation scenarios (and existence) of some exotic objects.

6.3 Final thoughts

As it turns out, binary star evolution does not only affect the stars themselves, but also their environment. The dynamical evolution of globular clusters, for example, is driven partly by binaries, although the formation of such large groups of stars is still not fully understood. The decryption of the dynamical story of globular clusters hidden in their different exotic stellar populations formed through binaries may be the link to the conditions of when these populous objects formed. Globular clusters are the building blocks of galaxies and remnants from the initial moments of the formation of our own Galaxy, and, possibly, their history may be recovered only through the understanding of the evolution of binary star.

Finally, we note that astronomical observations have ever only relied

on the light received here on Earth to explain celestial phenomena. We only see stars and galaxies through the photons they emit (at least for now; gravitational wave detection has become an intense field of research). Yet, in most instances, the information carried by these little photons tells a story that we still can not fully reconcile with our own theories. Sometimes, then, it is only through our imagination and innovative creations that we can hope to learn more about what is hidden to us. Such a quest for knowledge has lead us to use numerical simulations to recreate the structures of the Universe, to fast-forward the formation and evolution of galaxies and stars, and to "observe" the interactions of stars with each other, with the aim of always pushing further the limits of our theories. It is in the hope of a greater appreciation of the inner workings of the Universe on all of its scales that we pursue this research, one small step at a time.

Bibliography

Abt, H.A & Levy, S.G. 1976, ApJS, 30, 273

Aarseth, S.J., Tout, C.A., & Mardling, R.A. 2008, The Cambridge N-body Lectures: Lecture Notes in Physics, 760, Springer-Verlag (Berlin-Heidelberg)

Balsara, D.S. 1995, J. Comp. Phys., 121, 357

Bate, M.R., Bonnell, I.A., & Price, N.M. 1995, MNRAS, 277, 362

Bate, M.R. 1995, Ph.D. Thesis, University of Cambridge, UK

Benz, W. 1984, A&A, 139, 378

Benz, W., Slattery, W.L., & Cameron, A.G.W. 1986, Icarus, 66, 515

Benz, W. 1990, The Numerical Modeling of Nonlinear Stellar Pulsations: Problems and Prospects, in Buchler J.R. ed., Kluwer (Dordrecht), p.26

Benz, W., Bowers, R.L., Cameron, A.G.W., & Press, W.H. 1990, ApJ, 348, 647

Binney, J., & Tremaine, S. 1987, Galactic Dynamics, in Ostriker J.P. ed., Princeton Univ. Press (Princeton)

Blondin, J.M., Richards, M.T., & Malinowski, M.L. 1995, ApJ, 445, 939

Church, R.P., Dischler, J., Davies, M.B., Tout, C.A., Adams, T., & Beer, M.E. 2009, MNRAS, 395, 1127

Clayton, D.D. 1984, Principles of stellar evolution and nucleosynthesis, The University of Chicago Press (Chicago)

Crawford, J.A. 1955, ApJ, 121, 71

Cummins, S.J, & Rudman, M. 1999, J. Comp. Phys., 152, 584

D'Souza, M.C.R., Motl, P.M., Tohline, J.E., & Frank, J. 2006, ApJ, 643, 381

Dan, M. Rosswog, S., & Brüggen, M. 2009, arXiv:0811.1517

Dermine, T., Jorissen, A., Siess, L., & Frankowski, A. 2010, A&A, 507, 891

Deupree, R.G., & Karakas, A.I. 2005, ApJ, 633, 418

Duquennoy, A. & Mayor, M. 1991, A&A, 248, 485

Edwards, D.A., & Pringle, J.E. 1987, MNRAS, 229, 383

Eggleton, P.P. 1983, ApJ, 268, 368

Eggleton, P.P. & Kisseleva-Eggleton, L. 2006, Astrophys. Space Sci., 304, 75

Eggleton, P.P. 2006, Evolutionary Processes in Binary and Multiple Stars, Cambridge Univ. Press (Cambridge)

Fischer, D.A. & Marcy, G.W. 1992, ApJ, 396, 178

Flannery, B.P. 1975, ApJ, 201, 661

Gaburov, E., Lombardi, J.C. Jr, & Portegies Zwart, S. 2010, MNRAS, 402, 105

Gingold, R.A., & Monaghan, J.J. 1977, MNRAS, 181, 375

Gokhale, V., Peng, X.M., & Frank, J. 2007, ApJ, 655, 1010

Governato, F. et al. 2009, MNRAS, 398, 312

Guenther, D.B., Demarque, P., Kim, Y.-C., & Pinsonneault, M.H. 1992, ApJ, 387, 372

Halbwachs, J.L., Mayor, M., Udry, S., & Arenou, F. 2003, A&A, 397, 159

Han, Z., Tout, C.A., & Eggleton, P.P. 2000, MNRAS, 319, 215

Han, Z., Eggleton, P.P., Podsiadlowski, P., Tout, C.A., & Webbink, R.F. 2001, Evolution of Binary and Multiple Star Systems, in Podsiadlowski P. et al. eds, ASP conf. series 229 (San Fransisco), p.205

Hansen, C.J., & Kawaler, S.D. 1994, Stellar Interiors. Physical Principles, Structure, and Evolution, Springer-Verlag (New York)

Heintz, W.D. 1969, JRASC, 63, 275

Hernquist, L., & Katz, N. 1989, ApJS, 70, 419

Humble, R.J. 1999, Ph.D. Thesis, Monash University, Australia

Hurley, J.R., Tout, C.A., & Pols, O.R. 2002, MNRAS, 329, 897

Hut, P. 1981, A&A, 99, 126

Iben, I. Jr 1991, ApJS, 76, 55

Iben, I. Jr, & Livio, M. 1993, PASP, 105(694), 1373

Ivanova, N., Belczynski, K., Fregeau, J.M., & Rasio, F.A. 2005, MNRAS, 358, 572

Kippenhahn, R. & Weigert, A. 1967, Zeitschrift fur Astrophysik, 65, 251

Kozai, Y. 1962, AJ, 67, 591

Lauterborn, D. 1970, A&A, 7, 150

Layton, J.T., Blondin, J.M., Owen, M.P., & Stevens, I.R. 1998, New Astron., 3, 111

Lombardi, J.C. Jr, Rasio, F.A., & Shapiro, S.L. 1995, ApJ, 445, L117

Lombardi, J.C. Jr, Sills, A., Rasio, F.A., & Shapiro, S.L. 1999, J. Comp. Phys., 152, 687

Lombardi, J.C. Jr, Proulx, Z.F., Dooley, K.L., Theriault, E.M., Ivanova, N., & Rasio, F.A. 2006, ApJ, 640, 441

Lubow, S. H., & Shu, F. H. 1975, ApJ, 198, 383

Lucy, L.B. 1977, AJ, 82, 1013

Mashchenko, S., Couchman, H.M.P., & Wadsley, J. 2006, Nature, 442, 539

Mathieu, R.D. 1994, ARA&A, 32, 465

Mayer, L., Lufkin, G., Quinn, T., & Wadsley, J. 2007, ApJ, 661, L77

Meibom, S., & Mathieu, R.D. 2005, ApJ, 620, 970

Monaghan, J.J. & Lattanzio, J.C. 1985, A&A, 149, 135

Monaghan, J.J. 1989, J. Comp. Phys., 82, 1

Monaghan, J.J. 1992, ARA&A, 30, 543

Monaghan, J.J. 1994, J. Comp. Phys., 110, 399

Monaghan, J.J. 1997, SPH Tech. Note #2, CSIRO Div. of Maths and Stats, Tech. Report DMS C 95/86

Morris, J.P., Fox, P.J., & Zhu, Y. 1997, J. Comp. Phys., 136, 214

Morton, D.C. 1960, ApJ, 132, 146

Motl, P.M., Tohline, J.E., & Frank, J. 2002, ApJS, 138, 121

Navier, M. 1822, Mem. de l'Acad. des Sciences, 6, 389

Paczyński, B. 1965, Acta Astron., 15(2), 89

Paczyński, B. 1971, ARA&A, 9, 183

Paczyński, B., & Sienkiewicz, R. 1972, Acta Astron., 22, 73

Paczyński, B. 1976, Structure and Evolution of Close Binary Systems, in Eggleton, P., Mitton, S., Whelan, J. eds, IAU Symp. 73, Reidel (Dordrecht), p.75

Petrova, A.V., & Orlov, V.V. 1999, AJ, 117, 587

Poisson, S.D. 1829, J. de l'Ecole Polytech., 13, 1

Pooley, D., & Hut, P. 2006, ApJ, 646, L143

Portegies Zwart, S.F., & Verbunt, F. 1996, A&A, 309, 179

Press, W.H., Teukolsky, S.A., Vetterling, W.T., & Flannery, B.P. 1992, Numerical Recipes in Fortran, Cambridge Univ. Press (Cambridge)

Price, D. 2004, PhD thesis, Univ. Cambridge (astro-ph/0507472)

Price, D.J., & Monaghan, J.J. 2007, MNRAS, 374, 1347

Price, D.J. 2007, Publ. Astron. Soc. Aust., 24, 159

Price, D.J., & Bate, M.R. 2009, MNRAS, 398, 33

Raguzova, N.V., & Popov, S.B. 2005, Astron. Astrophys. Trans., 24, 151

Rasio, F.A., & Shapiro, S.L. 1991, ApJ, 377, 559

Rasio, F.A., & Shapiro, S.L. 1994, ApJ, 432, 242

Rasio, F.A., & Shapiro, S.L. 1995, ApJ, 438, 887

Regös E., Bailey, V.C., & Mardling, R. 2005, MNRAS, 358, 544

Renvoizé, V., Baraffe, I., Kolb, U., & Ritter, H. 2002, A&A, 389, 485

Ritter, H. 1988, A&A, 202, 93

Rodono, M. 1992, Evolutionary Processes in Interacting Binary Stars, in Kondo, Sistero, & Polidan eds, IAU Symp. 151, Kluwer (Dordrecht), p.71

Rosswog, S., Speith, R., & Wynn, G.A. 2004, MNRAS, 351, 1121

Saint-Venant, B. de 1843, Comptes Rendus, 17, 1240

Savonije, G.J., & Papaloizou, J.C.B. 1983, MNRAS, 203, 581

Sawada, K., Matsuda, T.,& Hachisu, I. 1986, MNRAS, 219, 75

Scalo, J.M. 1986, Fund. Cosmic Phys., 11, 1

Sepinsky, J.F., Willems, B., & Kalogera, V. 2007a, ApJ, 660, 1624

Sepinsky, J.F., Willems, B., Kalogera, V., & Rasio, F.A. 2007b, ApJ, 667, 1170 (SWKR07)

Sepinsky, J.F., Willems, B., Kalogera, V., & Rasio, F.A. 2009, ApJ, 702, 1387 (SWKR09)

Sills, A., & Lombardi, J.C.Jr 1997, ApJ, 484, L51

Sills, A., Lombardi Jr, J.C., Bailyn, C.D., Demarque, P., Rasio, F.A., & Shapiro, S.L. 1997, ApJ, 487, 290

Sills, A., Faber, J.A., Lombardi Jr, J.C., Rasio, F.A., & Warren, A.R. 2001, ApJ, 548, 323

Soberman, G.E., Phinney, E.S., & van den Heuvel, E.P.J. 1997, A&A, 327, 620

Sod, G.A. 1978, J. Comp. Phys., 27, 1

Springel, V., & Hernquist, L. 2002, MNRAS, 333, 649

Stinson, G.S. et al. 2009, MNRAS, 395, 1455

Stokes, G.G. 1845, Trans. Camb. Phil. Soc., 8, 287

Takeda, H., Miyama, S. M., & Sekiya, M. 1994, Prog. Theo. Phys., 92(5), 939

Theuns, T., Boffin, H.M.J., & Jorissen, A. 1996, MNRAS, 280, 1264

Tohline, J.E. 2002, ARA&A, 40, 349

Tout, C.A. 2008, in The Cambridge N-body Lectures, Lecture Notes in Physics, 760, Springer-Verlag (Berlin-Heidelberg), 297

van der Sluys, M. 2006, Ph.D. Thesis, Utrecth University

Wadsley, J.W., Stadel, J., & Quinn, T. 2004, New Astron., 9, 137

Warner, B., & Peters, W.L. 1972, MNRAS, 160, 15

Zahn, J.-P. 1977, A&A, 57, 383